IntechOpen

Drones
Applications

Edited by George Dekoulis

DRONES - APPLICATIONS

Edited by **George Dekoulis**

Drones - Applications
http://dx.doi.org/10.5772/intechopen.70910
Edited by George Dekoulis

Contributors

Denis Kotarski, Josip Kasać, Fuad Surastyo Pranoto, Ari Sugeng Budiyanta, Gunawan Setyo Prabowo, Lei Ma, Manchun Li, Gaofei Yin, Zhenjing Zhou, Heng Lu, Alfredo Toriz Palacios, José María Enrique Bedolla Cordero, Modesto Raygoza Bello, Edgar Toriz Palacios, Jessica Lisbeth Martínez González, Naiwen Li, Xiao Fu, Chao Liu, Longguo Li, Sergey Cherkasov, Dmitry Kapshtan, Szymon Ptak, Marzena Półka, Łukasz Kuziora, Aneta Kuczyńska, Paul Oppong Kwabena Opk, Han-Ping Mao, Lin Li, George Dekoulis

Notice

First published in London, United Kingdom, 2018 by IntechOpen
eBook (PDF) Published by IntechOpen, 2019
IntechOpen is the global imprint of INTECHOPEN LIMITED, registered in England and Wales, registration number: 11086078, The Shard, 25th floor, 32 London Bridge Street
London, SE19SG – United Kingdom
Printed in Croatia

British Library Cataloguing-in-Publication Data
A catalogue record for this book is available from the British Library

Additional hard and PDF copies can be obtained from orders@intechopen.com

Drones - Applications
Edited by George Dekoulis

p. cm.

Print ISBN 978-1-78923-284-4

Online ISBN 978-1-78923-285-1

eBook (PDF) ISBN 978-1-83881-478-6

Meet the editor

Prof. George Dekoulis received his PhD degree in Space Engineering and Communications from Lancaster University, UK, in 2007. He was awarded a First-Class BEng (Hons) in Communications Engineering from De Montfort University, UK, in 2001. He received several awards from STFC, UK, and EPSRC, UK, and the "IET Hudswell International Research Scholarship." He is currently a professor at Aerospace Engineering Institute (AEI), Cyprus. He has previously worked as a professor in Aerospace Engineering at various departments, such as Space and Planetary Physics, Aeronautical and Space Engineering, Professional Flight, Robotics, Mechatronics, Computer Engineering, Electrical and Electronics, Computer Science, and Mechanical Engineering. His research is focused on the design on reconfigurable state-of-the-art space engineering systems.

Contents

Preface

This edited volume is a collection of reviewed research chapters, concerning the recent developments in the area of drones.

The book includes scholarly contributions by various authors. It was edited by Prof. George Dekoulis, an expert on state-of-the-art implementations of reconfigurable space engineering systems.

The book is divided into four sections: "Introduction," "Drone History," "Drone Design," and "Drone Applications."

After "Introduction," the first section, "Drone History," provides a historical overview of the drones being used by the Indonesian National Institute of Aeronautics and Space. Emphasis is given on the capabilities of these drones in facilitating civilian applications. The following research contribution is contained: "Small to Medium UAVs for Civilian Applications in Indonesia."

The following section on "Drone Design" consists of three research chapters, namely, "Smart Arduino Sensor Integrated Drone for Weather Indices:Prototype," "Generalized Control Allocation Scheme for Multirotor UAVs," and "Uncertainty of Object-Based Image Analysis for Drone Survey Images."

The last section of the book is dedicated to "Drone Applications." It consists of the following four chapters: ""The Use of Unmanned Aerial Vehicles by Urban Search and Rescue Groups," "New Applications of 3D SLAM on Risk Management Using Unmanned Aerial Vehicles in the Construction Industry," "Land use Information Quick Mapping Based on UAV Low-Altitude Remote Sensing Technology and Transfer Learning," and "Unmanned Aerial Systems for Magnetic Survey."

We hope that you will enjoy reading this book and be inspired to scientifically contribute to further success of the global drone community.

Prof. George Dekoulis
Head of Aeronautical and Space Engineering Department
Aerospace Engineering Institute (AEI)
Cyprus

Introduction

Chapter 1

Introductory Chapter: Drones

George Dekoulis

Additional information is available at the end of the chapter

http://dx.doi.org/10.5772/intechopen.76943

Θρώναξ Laconic, Κηφήν Hesychius, Καφάν Doric, Θόρναξ Temple of Apollo Laconic, Minyan hEllenopelasgic Mother of Gods, Θρόναξ Jensius > dröna Swedish > dröhnen German > dreunen Dutch > drān, drǣn Old English > drone, male bee > Unmanned Aircraft.

Αγαίαρχος Διοκλής, Diocles

1. Introduction

Would you explain how this prehistoric word of unknown chronology, initially meaning the Divine male bee, ended up being equivalent to unmanned aircrafts? The mother of drones was symbolised >4000 years ago in many ways, such as the one presented in **Figure 1**.

In nature, drones are male bees with no stingers. They are not responsible for collecting nectar and pollen; the female worker bees do that. Their purpose is to mate with a fertile queen bee. This is how the term drone was introduced to the public, to signify a remotely controlled aircraft for battleship weapon's target practice. The Fairy Queen and the de Havilland Queen Bee target aircrafts were introduced in the 1920s and 1930s, respectively. The DH.82 Queen Bee is presented in **Figure 2**.

Subsequent models were named in a similar manner, such as Airspeed Queen Wasp and Miles Queen Martinet. Drones were first flown during the First World War. They were launched by a catapult and flown using radio-controlled technologies. Their mission objectives have constantly been increasing. Reconnaissance drones were also heavily employed during the Vietnam War. Common missions include decoy actions during missile launching, actual combat and leaflet dropping during psychological war. The United States and Great Britain were the first countries to introduce state-of-the-art technologies into recent drone developments. The

Figure 1. Laconic/Minoan mother of drones >1900 BC (Aegina) (British Museum, London).

Figure 2. Launch of a DH.82 Queen Bee (mother of drones) target drone (1941).

new level of sophistication, endurance, maintenance of higher altitudes, solar-based models and better fuel consumption to achieve longer flights are few of the increased specifications offered by the latest models.

Drones are currently being used in many applications, such as weather monitoring, search and rescue operations, managing natural catastrophes, aerial photography, delivery of goods, atmospheric research and other areas, such as the ones presented in this book.

Drone technology is a constantly developing field of science that today may involve international scientific collaborations. It is also the title of this publication. The aim and structure of the book are presented in the following section.

2. Aim of the book and organisation

The presentation of recent research results and state-of-the-art developments in the broader area of drone technologies is the aim of this book. The collective effort of distinguished international researchers has been incorporated into one textbook suitable for the broader audience interested into this scientific field.

Chapter 2 is dedicated to drone history.

The main historical milestones of drone development and deployment for common civilian applications are presented. Emphasis is given by the authors to drone civilian applications in Indonesia.

Chapters 3–5 present recent research results in drone design.

- Chapter 3 presents a drone project proposal for future measurements of the various weather indices using a smart Arduino sensor-integrated drone.
- Chapter 4 presents a generalized control allocation scheme for multirotor UAVs.
- Chapter 5 presents the development of an object-based algorithm for analysing survey images obtained by drones.

Chapters 6–9 present recent research results obtained by modern drone applications.

- Chapter 6 presents modern techniques employed into urban search and rescue operations using drones.
- Chapter 7 presents how risk management techniques can be utilised by the construction industry through the usage of drones.
- Chapter 8 presents how land-use information quick mapping and transfer learning can be achieved using drones.
- Chapter 9 presents how magnetic surveys can be performed using drones.

3. Conclusion

Drone technologies have constantly been developing for over 100 years. The latest models exhibit a previously unseen set of specifications available to the end users. In this book, recent research results are presented in the areas of drone design and drone applications. We hope

this book will be advantageous to researchers and also inspire the younger generations into pursuing studies and careers within the drone industry.

Author details

George Dekoulis

Address all correspondence to: dekoulis@aeispace.org

Aeronautical and Space Engineering Department, Aerospace Engineering Institute (AEI), Nicosia, Cyprus

Section 2

Drone History

Chapter 2

Small to Medium UAVs for Civilian Applications in Indonesia

Fuad Surastyo Pranoto, Ari Sugeng Budiyanta and Gunawan Setyo Prabowo

Additional information is available at the end of the chapter

http://dx.doi.org/10.5772/intechopen.76426

Abstract

Indonesian government needs a well-built, easy to operate unmanned aircraft systems (UAS) to perform various civilian missions as UAS are a well-known platform for dirty, dull, and dangerous missions. Hence, the Indonesian government has an organization that performs research and development of UAS, named as Aeronautic Technology Center. This organization is placed underneath Indonesian National Institute of Aeronautics and Space. The UAS developments in this institute are primarily driven by civilian uses; therefore, the UAS size, sensor types, and mission payload are optimized for civilian missions. In order to produce the decent to the best quality of the aerial image, which is the essential product for various civilian missions, the UAS regularly flies under the cloud. For this reason, the Aeronautic Technology Center is only developing the LASE (low altitude, short-endurance) and the LALE (low altitude, long endurance) UAS type as of now. The UAS development was begun with LSU-01, followed by LSU-02, LSU-03, and LSU-05. The LSU-01, LSU-02, and LSU-03 are in the operational phase, while the LSU-05 is in the experimental Phase. In this chapter, the specification of the platforms and the sensor capabilities that are relevant with the demands of users in the civilian sector are described.

Keywords: unmanned aerial system, low altitude, long endurance, civilian missions, sensor capabilities

1. Introduction

Indonesia is a beautiful country and has a lot of volcanoes, beaches, and some beautiful landscapes. Furthermore, Indonesia located in the equatorial area where only two seasons

available, summer and rainy. In summer, the beautiful landscapes are enjoyable by many tourists. Contrary to the summer season, rainy season is the unfavorable time for traveling to Indonesia. The reason is, during the rainy season, the rainfall could be increasingly high. The rainfall characteristics over Indonesia are known to have seasonal and inter-annual variability primarily related to the monsoon and El Niño/Southern Oscillation (ENSO) [1]. The East Monsoon, from June to September, brings in dry weather, whereas the West Monsoon, from December to March, brings in the rain. The heaviest rainfall is usually recorded in December and January [2]. The average annual rainfall for Indonesia's Main Islands is ranging between 1200 and 3190 mm/year. The fourth highest rainfall is recorded in Papua (3190 mm/year), Kalimantan (2990 mm/year), Sumatra (2820 mm/year), and Java Island (2680 mm/year) [3]. The high rainfall is committed to flooding disaster. Especially in Java, where the population density is the highest (Java-Bali has estimated for among 58.7 and 59.6% of the national population average between 1993 and 2007 [4]), the flooding disaster could lead to the severe consequence. One of the flood disaster examples is the Jakarta flood on 2 February 2007 that inundated 70,000 houses, displaced 420,440 people and killed 69 people with losses of IDR. 4.1 trillion (US$ 450 million) [5].

Despite the flooding disaster, Indonesia is susceptible to the earthquake and volcanic eruption disasters. The reason why the earthquake frequently happens is the Indonesian location. Placed in one of the most active seismic zones in the world, Indonesia also lies on five active tectonic plates geologically. Hence, the earthquakes occurred daily in the region, with a magnitude of five in Richter scale or larger happened weekly [6]. In order to recognize the greatness of earthquake destruction, look at the following case. On March 2007, a powerful earthquake hit the Indonesian island of Sumatra and resulted in 66 fatalities, 500 injured, and severe damage or destruction of nearly 15,000 buildings. The total loss from the earthquake is estimated at US$180 million [7].

The mountainous terrain of Indonesia is the hideout of some disasters. The mountainous terrain plus Indonesian location in Pacific Rim ring of fire is a good recipe for volcanic eruptions. The mountainous terrain and wet soil could lead to the landslide. Both of the disasters happen frequently in Indonesia.

The natural disaster such as the earthquakes, the floods, the volcanic eruptions and the landslide are one of the problems that confronted by the government. Other problems such as forest fire, illegal fishing, border protection, and terrorism are demand to be fixed too. The government needs an adequate field data to be examined before performing the remedial action.

One of the methods to obtain necessary field data is the aerial photography where the aerial photo is the output of this method. The aerial photo is useful to determine the level of destruction of the disasters and the affected area. Both parameters are necessary for post-disaster management, such as creating the evacuation route for search and rescue team. The aerial photo could be used to validate the hot spot location in the forest fire. That information is useful for firefighting team to control and extinguish the fire. Other

http://dx.doi.org/10.5772/intechopen.76426

interesting functions of the aerial photo are discovering the terrorist hideout in counter-terrorism mission, spotting the illegal fishing operation and protecting the border from smugglers.

The aerial photo, indeed, needs a camera and a platform that capable for carrying the camera into the air. The camera and the platform selection are highly dependent on the mission requirement. A lot of camera is already available in the market for aerial photography. However, the platform shall be built specifically according to the requirement defined by Indonesian government. The Indonesian government needs a well-built, easy to operate unmanned aircraft systems (UAS) platform to perform coastline and borderline surveillance, disaster management and mitigation missions as a UAS are a well-known platform for dirty, dull, and dangerous missions.

For that purposes, the Indonesian government has an organization that performs research and development of UAS platform, named as Aeronautic Technology Center. This organization is placed underneath Indonesian National Institute of Aeronautics and Space. The UAS developments in this institute are primarily driven by civilian uses; therefore, the UAS size, performance, and mission payload are optimized for civilian missions.

However, because Indonesia positioned in the equator area, the sky is cloudy almost every day. In order to produce the decent to the best quality of the aerial photo, the platform (UAS) regularly flies under the cloud. For this reason, the Aeronautic Technology Center only developing The LASE (Low Altitude, Short-Endurance) and the LALE (Low Altitude, Long Endurance) UAS type for now.

The UAS development was begun with LSU-01, followed by LSU-02, LSU-03, LSU-04 and LSU-05. The LSU-01, LSU-02, and LSU-03 are in the operational phase while the LSU-04 and LSU-05 are in the experimental phase. Hence, all three UAS are frequently used for various civilian missions.

In this chapter, the specification of the platforms is described, as well as sensor capabilities, and advantages of each as relevant to the demands of users in the civilian sector. We also briefly discuss the field experience that obtained during the UAS operation.

2. LAPAN surveillance UAS specification

The LAPAN Surveillance UAS, abbreviated as LSU, is the UAS platform developed by Aeronautic Technology Center for the civilian purposes. The design of the UAS and the payload system are utilized mainly for aerial photography missions. The payload system usually uses a small format digital camera. The UAS platform categorized as The LASE (Low Altitude, Short-Endurance) and the LALE (Low Altitude, Long Endurance) class. The LSU family consists of five types such as LSU-01, LSU-02, LSU-03, LSU-04, and LSU-05. **Figure 1** shows the UAS size comparison.

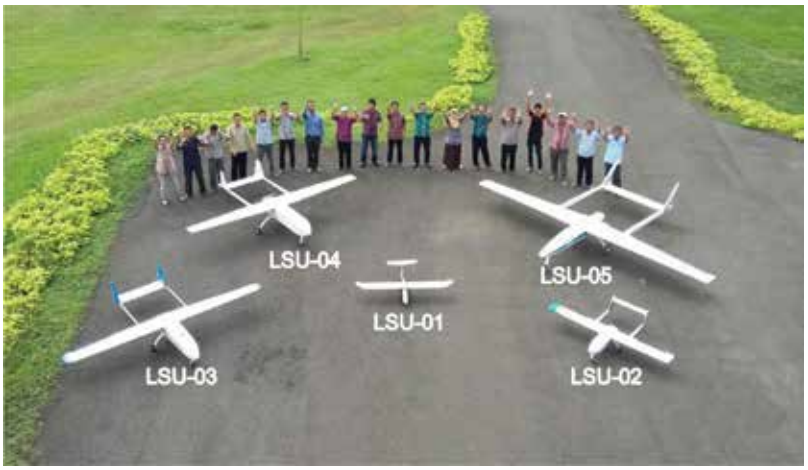

Figure 1. LSU family.

The LSU UAS platform requires an additional system for autonomous flight. The system consists of RC transmitter, RC receiver, autopilot, and servo actuator. During the autonomous flight, the UAS position shall be monitored by ground control segment in real-time. Therefore, a telemetry and ground control station shall be available too. The UAS pilot handles the take-off and landing operation manually. **Figure 2** shows the correlation between the UAS and ground control segment.

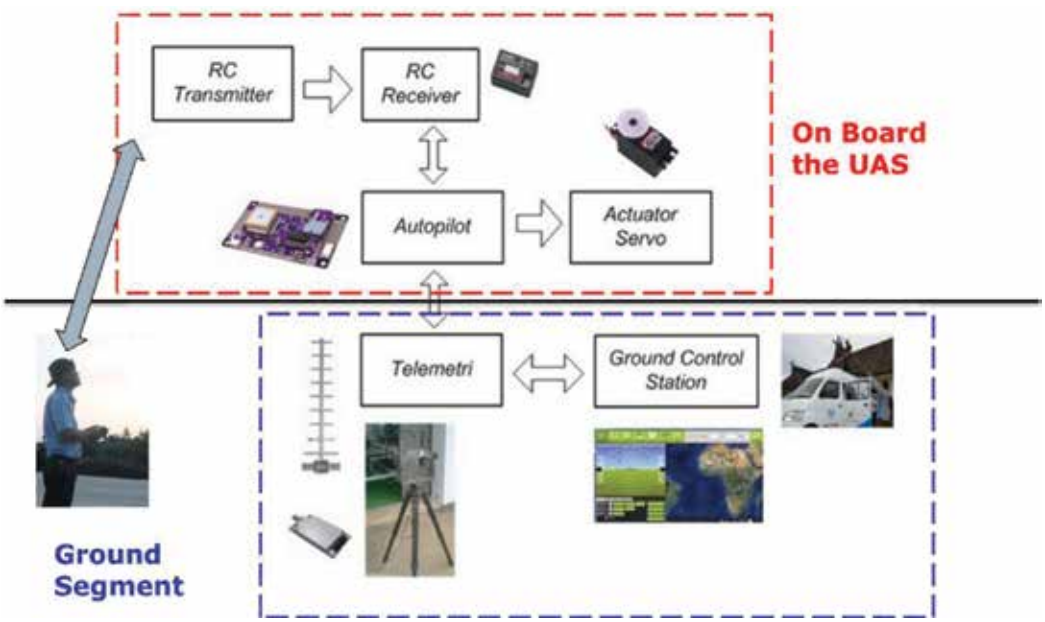

Figure 2. The LSU family avionic system and ground segment.

The autopilot system uses commercially out of the self (COTs) product. There are a lot of alternatives for the UAS autopilot, such as Ardu Pilot Mega (APM), Pixhawk, Feuyu Tech Autopilot Panda, Micro Pilot, and Piccolo Autopilots. However, we use only the Ardu Pilot Mega (APM), Pixhawk, Feuyu Tech Autopilot Panda for our UAS platform.

The ground control segment uses open source software for the flight planning, commanding the UAV, and receiving telemetry data. We use Ardu Pilot Mission Planner if the autopilots are Ardu Pilot Mega (APM) and Pixhawk.

The telemetry system to extend the UAS communication ranges up to 47 km is developed. Without the telemetry system, the UAS communication ranges only 2 km. The telemetry system capable of receiving data (flight data, real-time video, and picture) from the UAS to the ground control segment as well as sending autopilot command to the UAS. The telemetry system located on the ground segment; utilize the Yagi antenna for tracking the UAS while on board the UAS use the omnidirectional antenna. The Yagi antenna is capable of tracking the UAS manually (with the GPS assist) or automatically. **Figure 3** shows the telemetry system of the UAS.

The remote control system is necessary for take-off and landing operation of the LSU family. The LSU family normally take off and climb to the cruise altitude manually, then, change to the automatic mode during the aerial photography mission. After completing the mission, the UAS descending to the commanded altitude automatically and the UAS pilot will take over the control and land the UAS manually. The remote control utilizes the 72 and 2400 MHz frequency for interacted with the UAS operation mode. There are three operation modes: manual, stable, and fully autonomous mode. The maximum operating range of the radio control is 5 km and the typical operating range is 2 km.

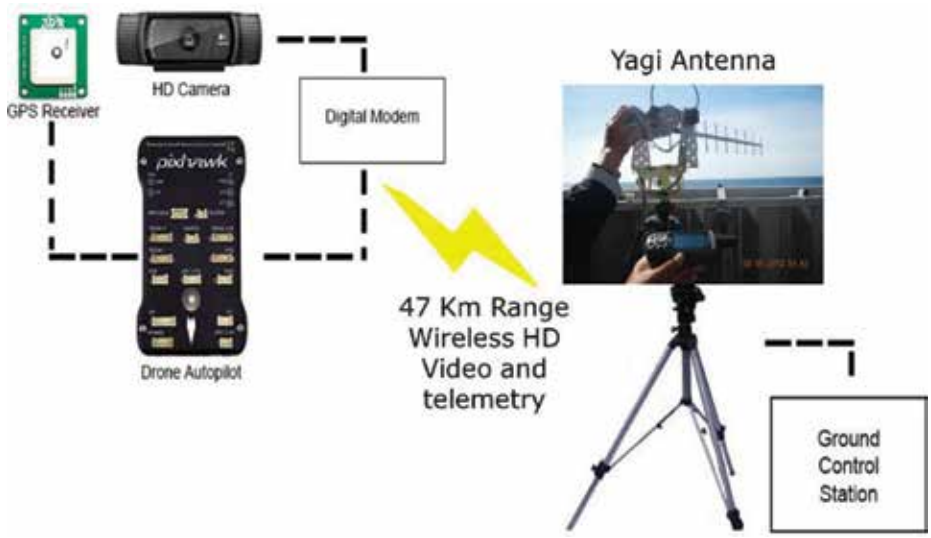

Figure 3. The LSU family telemetry system.

2.1. UAS specification

This chapter describes the LSU family technical specification.

2.1.1. LSU-01

The LSU-01 is the smallest UAS platform in the LSU family. This platform is the only one who uses the electric engine. The platform design is based on the Skywalker UAS family. However, there are some modifications applied to the platform in order to make the platform perform better in the field, such as:

1. Additional fiber lamination to enhance the structural strength of the UAS. The UAS structure is made from the Styrofoam which is known as sturdy and light material. However, in the field, we learned that the material is not sturdy enough when the UAS shall perform the hard landing. The additional fiber lamination helps to protect the UAS structure from destruction when hard landing
2. Special camera bay for housing the small format digital camera. The camera bay is outfitted with structural support and rubber to prevent the camera from shaking. When the shake is minimized, the aerial photo quality is increased (**Figure 4**).

The LSU-01 is used for an aerial photography mission. The mission shall have the following requirement, such as the survey area is within 0–1000 hectares, no proper takeoff and landing place near the mission location, and the survey location has a calm wind condition (the wind speed below 10 m/s). The LSU-01 is capable to finish 250 hectares survey area in one flight with Canon S100 camera. The average speed in flight is 15 m/s, the flight altitude is 300 m above ground level, the flight time is within 30–50 min (highly dependent on the wind condition). **Table 1** shows the detailed specification of LSU-01.

2.1.2. LSU-02

The LSU-02 is the second UAS platform in the LSU family. This platform uses a gasoline engine in push configuration. The platform design is inspired by skyhunter UAS family. The longitudinal section of LSU-02 fuselage is nearly square and has an advantage of the big payload bay.

Figure 4. Left: LSU-01 final configuration; right: LSU-01 during operation with the camera bay shown under the fuselage.

Parameter	Unit	Value
Physical specification		
Wingspan	mm	1830
Wing area	dm^2	41.17
Wing aspect ratio	—	8.133
Wing taper ratio	—	0.885
Fuselage length	mm	1270
Weight specification		
Empty weight	g	1400
Payload weight	g	1600
Maximum takeoff weight	g	3000
Flight performance		
Endurance	min	30–50
Cruise speed	m/s	15
Maximum speed	m/s	25
Service ceiling	m	1500
Payload configuration		
Engine	—	2820KV850–900
Engine type	—	Electric
Electronic speed controller	A	60
Propeller	in.	13
Battery capacity	mAH	2 × 4S 5000
Servo	—	4 × 12 g
Autopilot	—	3DR Pixhawk Mini
Camera	—	Canon S100
Takeoff method	—	Hand cast manual/full auto
Landing method	—	Manual/full auto/parachute

Table 1. LSU-1 technical specification.

The LSU-02 has a landing gear; therefore, the takeoff and landing operation need a runway. However, there are some modifications applied to the platform in order to extend the LSU-02 takeoff and landing capabilities such as implementation of catapult launch for takeoff and parachute or landing net for landing operation. The catapult launch of LSU-02 was successfully tested while the parachute landing still needs some improvements. **Figure 5** shows the LSU-02 during operation.

Figure 5. Top-left: LSU-02 final configuration shortly before takeoff; top-right: LSU-02 during aerial photography mission; bottom-left: landing operation with net; bottom-right: takeoff preparation from Indonesian Hasanudin class corvette warship.

The LSU-02 is used for an aerial photography mission. The LSU-02 has an endurance of 4 h with the average ground speed of 27 m/s. The LSU-02 is capable to finish 2500 hectares survey area in one flight with Sony A6000 camera. In one sortie of flight, the LSU-02 flies at 27 m/s ground speed, 60–80 min flight time and 300 m flight altitude. The LSU-02 has more resistant to the wind disturbance due to powerful gasoline engine installed on this aircraft. The LSU-02 is capable to maintain the 27 m/s groundspeed under 10 m/s headwinds. The LSU-02 is suitable for aerial photography mission that have 10,000–15,000 hectares survey area and has a grass runway for normal takeoff and landing operations. **Table 2** shows the detailed specification of LSU-02.

2.1.3. LSU-03

The LSU-03 is the third UAS platform in the LSU family. This platform is developed from LSU-02; therefore, it uses a gasoline engine in push configuration. The LSU-03 has bigger wing and bigger fuselage compared to the LSU-02 (**Figure 6**). The advantages of LSU-03 over LSU-02 such as longer endurance due to increase fuel capacity and heavier payload capability, it means the LSU-03 is capable to lift up the medium format camera for aerial photography.

The LSU-03 has endurance up to 6 h with the average ground speed of 30 m/s. The LSU-03 is capable to finish 7500 hectares survey area in one flight with Sony A6000 camera. In one sortie of flight, the LSU-03 flies at 30 m/s ground speed, 120–150 min flight time and 300 m flight

Parameter	Unit	Value
Physical specification		
Wingspan	mm	2400
Wing area	dm^2	66.5
Wing dihedral	°	2
Wing swept angle	°	0
Fuselage length	mm	1700
Weight specification		
Empty weight	g	9700
Payload weight (exclude fuel)	g	2000
Fuel weight	g	3300
Maximum takeoff weight	g	15,000
Flight performance		
Endurance	h	3.5–4.0
Cruise speed	m/s	27.3
Maximum speed	m/s	41.6
Service ceiling	m	2000
Payload configuration		
Engine	—	Gasoline
Engine capacity	cc	33
Engine fuel system	—	Carburetor
Propeller	in.	16 × 10
Battery capacity	mAH	3 × 4S 5500
Servo	kg.cm	7.7
Autopilot	—	3DR Pixhawk/Feuyu Tech Autopilot Panda
Flight mode	—	Manually, stable, autonomous
Camera	—	Sony A6000
Gimbal	—	1 axis (roll axis)
Takeoff method	—	Normal, launcher
Landing method	—	Normal, parachute

Table 2. LSU-2 technical specification.

altitude. The LSU-03 is suitable for aerial photography mission that have 20,000–30,000 hectares survey area and has a grass runway for normal takeoff and landing operations. **Table 3** shows the detailed specification of LSU-03.

Figure 6. Left: LSU-03 final configuration shortly before takeoff; right: LSU-03 test flight.

2.2. Payload specification

The payload for the LSU UAS family is mainly a small format digital camera. The aerial photography mission, which uses small format digital camera, is called as small format aerial photography (SFAP). Small-format aerial photography (SFAP) is based on lightweight cameras with 35- or 70-mm film format as well as equivalent digital cameras and other electronic imaging devices. For the most part, these are "popular" cameras designed for hand-held or tripod use by amateur and professional photographers. Such cameras lack the geometric fidelity and exceptional spatial resolution of aerial mapping cameras. Low-cost, availability of cameras and lifting platforms is a combination that renders SFAP desirable for many people and organizations. The SFAP is self-made remote sensing system design, technical implementation, and image analysis may be in the hands of a single person, granting utmost flexibility and specialization [8].

The SFAP may be classified according to the camera attitude (angle of photography) and the type of film used. Depending on the camera angle, the SFAP may be vertical or oblique classification. A vertical SFAP is taken with the axis of the camera at right angles to the horizontal. This yields an image which may be unfamiliar in format but which is relatively easy to manipulate photogrammetrically [9]. Almost all-modern SFAP, including SFAP missions that done by the LSU family is vertical in orientation.

Other interesting parameter in the SFAP is spatial resolution. The spatial resolution for digital camera sensor is known as ground sampling distance (GSD). If the GSD is specified too high (high GSD means small pixel size on the ground), more flight lines will be required and the amount of data per area will increase. It is recommended to specify both a target GSD and a minimum GSD to allow some flexibility because of terrain variation [10]. The very high-resolution satellite like worldview 1, 2, and 3 normally has 50, 46, and 31 cm of GSD, respectively, while manned and unmanned aircraft usually have 3–65 cm of GSD [11]. The smaller GSD value means more detail in the photograph. The GSD is calculated by using Eq. (1) from literature ([8], p. 22), where H_g is flight altitude above ground level and f is camera focal length.

$$GSD = (\textit{camera pixel element size}) \times H_g / f \tag{1}$$

Parameter	Unit	Value
Physical specification		
Wingspan	mm	3500
Wing area	dm^2	127
Wing dihedral	°	2
Wing swept angle	°	0
Fuselage length	mm	2500
Weight specification		
Empty weight	g	18,000
Payload weight (exclude fuel)	g	5000
Fuel weight	g	7000
Maximum takeoff weight	g	30,000
Flight performance		
Endurance	h	4.0–6.0
Cruise speed	m/s	30
Maximum speed	m/s	45
Service ceiling	m	2000
Payload configuration		
Engine	—	Gasoline
Engine capacity	cc	60
Engine fuel system	—	Carburetor
Propeller	in.	14 × 12
Battery capacity	mAH	3 × 4S 5500
Servo	kg.cm	7.7
Autopilot	—	3DR Pixhawk
Flight mode	—	Manually, stable, autonomous
Camera	—	Sony A6000
Gimbal	—	1 axis (roll axis)
Takeoff method	—	Normal, launcher
Landing method	—	Normal, parachute

Table 3. LSU-03 technical specification.

The "camera pixel element size" depends on the digital camera sensor size and the camera resolution. For example, a full frame digital camera Canon EOS 1D X mark II capable to record picture in various resolutions, such as 20.0 megapixels (5472 × 3648), 12.7 megapixels (4368 × 2912),

8.9 megapixels (3648 × 2432) and 5.0 megapixels (2736 × 1824) [12]. The full frame sensor has 36 by 24 mm dimensions and an effective area of 864 mm^2. The value of "camera pixel element size" for each camera picture resolution is shown in **Table 4**. **Table 4** shows higher camera resolution has more information inside 1 mm of sensor length. Assuming $H_g = 1000$ mm and $f = 1$ mm, the GSD at the highest resolution is 0.65 cm while at the lowest resolution is 1.31 cm. It means the picture at the highest resolution contains the detail twice as much as the picture at the lowest resolution.

For the aerial photography mission, the LSU-01 equipped with Canon S100 camera, while the LSU-02 and LSU-03 equipped with Sony A6000 camera. The canon S100 has 7.6 by 5.7 mm sensor size and the maximum resolution of 4000 by 3000 pixels. The focal length is variate between 5.2 and 26.0 mm (35 mm equivalent: 24–120 mm) [13]. On the other hand, the Sony Alpha A6000 has bigger sensor size and higher maximum picture resolution. The Sony Alpha A6000 sensor size measured at 23.5 by 15.6 mm and the maximum resolution of 6000 by 4000 pixels. The focal length of Sony Alpha A6000 camera is depends on the installed lenses. The lens of Sony Alpha A6000 is interchangeable because this camera belongs to the mirrorless camera type. The standard lens kit for Sony Alpha A6000 has variable focal length between 16 and 50 mm (35 mm equivalent, 24–75 mm) [14]. The LSU family usually flies at 300 m altitude during the aerial photography missions. Based on this information, the GSD for the Canon S100 and Sony Alpha A6000 at the longest and shortest focal length can be calculated. **Table 5** shows the GSD value for both camera at $H_g = 300$ m.

Unlike the LSU-01, the Sony Alpha A6000 that mounted in the LSU-02 and LSU-03 is equipped with a-axis gimbal. The gimbal compensates the aircraft roll movement and keeps the camera

Camera resolution (pix)	No. of pixels (Mpix)	Pixel element size (mm/pix)	No. of pixels per mm (pix/mm)
2736 × 1824	5.0	0.013157895	76
3648 × 2432	8.9	0.009868421	101
4368 × 2912	12.7	0.008241758	121
5472 × 3648	20	0.006578947	152

Table 4. Digital "camera pixel element size" for canon EOS 1D X mark II.

Camera resolution (pix)	Pixel element size (mm/pix)	Focal length (mm)	GSD (cm)
Canon S100			
4000 × 3000	0.0019	5.2	11
		26.0	2.2
Sony Alpha A6000 + 16–50 mm kit lens			
6000 × 4000	0.003916667	16.0	7.3
		50.0	2.35

Table 5. The GSD value of canon S100 and Sony Alpha A6000 at $H g = 300$ m.

http://dx.doi.org/10.5772/intechopen.76426

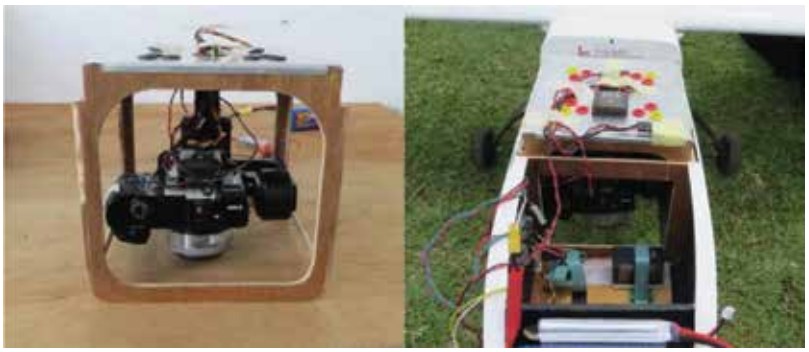

Figure 7. Left: the Sony Alpha A6000 attached in the gimbal. The gimbal is installed in the payload cage; right: the payload cage location at the LSU-02 fuselage.

for pointing downward. With the gimbal, the photograph is guaranteed to have a vertical orientation. The gimbal is attached to the payload cage that also has a rubber for damp the vibration for engine as shown in **Figure 7**. With the gimbal and the damper, the aerial photograph results of LSU-02 and LSU-03 are better compared with the LSU-01.

3. Lapan surveillance UAS mission

3.1. Aerial photography for volcanic mountain mapping

On 17 October 2014, the LSU-01 performed an aerial photography mission for creating 3-D photography of mount Merapi peak. Mount Merapi is the most active volcano mountains in the Java Island. The customer of this mission is Pusat Studi Bencana Alam (PSBA) Gadjah Mada University. The PSBA uses the data for post-disaster management. They analyze the scale of destruction if the mount Merapi erupts again based on the current crater condition. The new crater was created since the last mount Merapi eruption in 2010.

Before performing the mission, some preparations shall be done such as selection of the UAS, flight planning, camera selection, and image processing technique for creating 3-D photography.

The UAS selection shall examine the environment condition before making a decision. The environment is an active volcano and constantly vomiting the volcanic ash. The volcanic ash is one of the threats to the internal combustion engine; therefore, utilizing the LSU families with an internal combustion engine are not reasonable for this mission. The mission uses the LSU-01 because only the LSU-01 utilizes an electrical engine as primary thrust generator.

In order to capture the Mount Merapi, the LSU-01 shall fly 300 m above the mountain, meaning the UAS flies at 3200 m above mean sea level. However, the highest terrain (base camp) that reachable by the team has an altitude of 1050 m above mean sea level as shown in **Figure 8**. Consequently, the LSU-01 shall climb 2150 m to enter the mission altitude. The slant range from the base camp to the mountain peak is 4 km. The LSU-01 takeoff and landing from the base

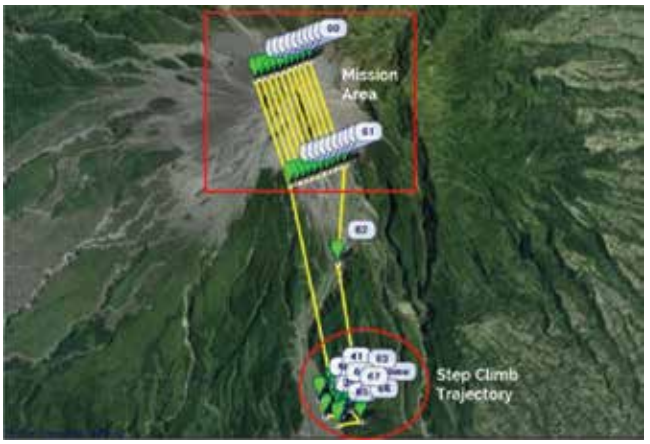

Figure 8. Flight planning for the mount Merapi mission. The red circle shows the waypoint for step climb from 1050 to 3000 m, while the red square shows the mission area at altitude 3200 m.

camp. The LSU-01 take off and climb to the 3000 m altitude using step climb method in circle trajectory. After reaching the 3000 m altitude, the LSU-01 flies 3.5 km and 200 m altitude to enter the mission altitude. At the mission altitude, a strong headwind cause the LSU-01 cannot move forward; hence, the team decides to change the waypoint on demand using telemetry system.

The mission uses Canon S100 camera mounted in the LSU-01 camera bay and equipped with the gimbal and vibration damper. The camera shutter speed is 3 s and the total flight time is 46 min. During this mission, the camera captures 275 raw aerial photos. The Agisoft PhotoScan software was used to process the raw aerial photos. **Figure 9** shows the result of this mission.

Figure 9. Top left and right: isometric view of mount Merapi peak, bottom: top view of mount Merapi peak shows the crater area.

3.2. Aerial photography for landslide disaster

The landslide is happening in Indonesia infrequently. However, once it is happening, the number of victims is quite high. One of the examples is the landslide disaster at Banjarnegara on 18 December 2014. Based on the information from the search and rescue team, there are three known locations of the landslide. The first location classified as the major landslide, the second classified as imminent landslide due to earth crack occurrence, and the third classified as the potential landslide. **Figure 10** shows the relative position between basecamp and the landslide area. The distance between the basecamp and the landslide location is around 2 km, while the altitude of the basecamp is 1023 m MSL. The aerial photography mission shall produce aerial photo that covers the major landslide, imminent landslide, and potential landslide location. The aerial photography is needed by Indonesian National Board for Disaster Management to identify the greatness of the disaster and planning the evacuation scheme for the search and rescue team.

The basecamp does not have any appropriate runway. As shown in **Figure 11** (top-left), the only grass field is available. Therefore, the LSU without landing gear is preferable for this mission. The LSU-01 is the only one who does not have a landing gear hence, the team selects the LSU-01 for this mission. After analyzing the landslide area, the LSU-01 is capable of taking the required aerial photography in one flight. The mission uses Canon S100 camera mounted in the LSU-01 camera bay and equipped with the gimbal and vibration damper. **Figure 11** shows the flight plan for this mission.

In order to capture the landslide area, the LSU-01 shall fly 300 m above ground level (AGL). We assume the altitude at landslide area is equal to the basecamp altitude. It means the LSU-01

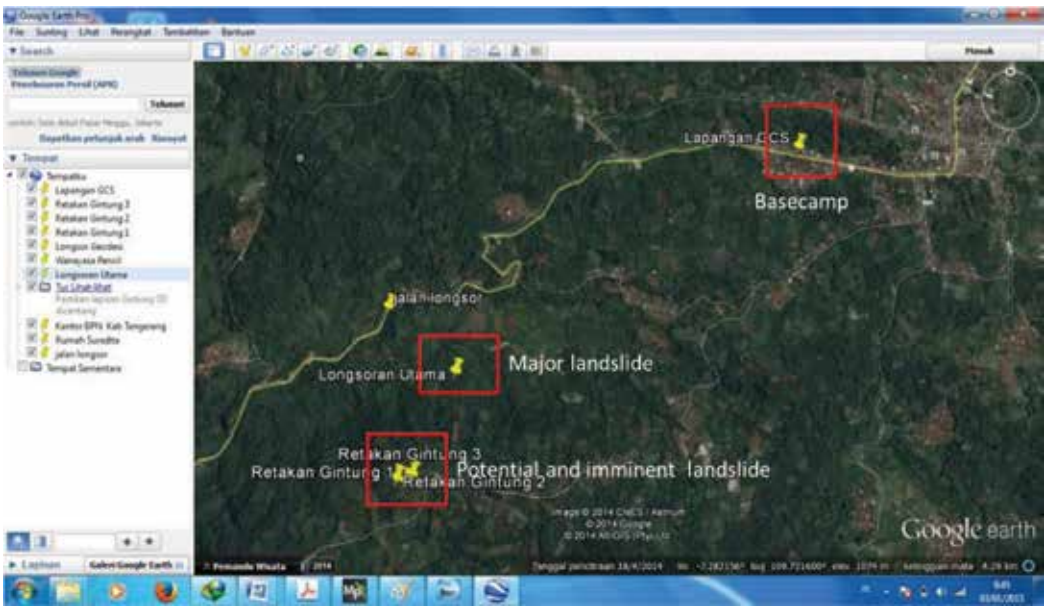

Figure 10. Relative position between the basecamp and the landslide position.

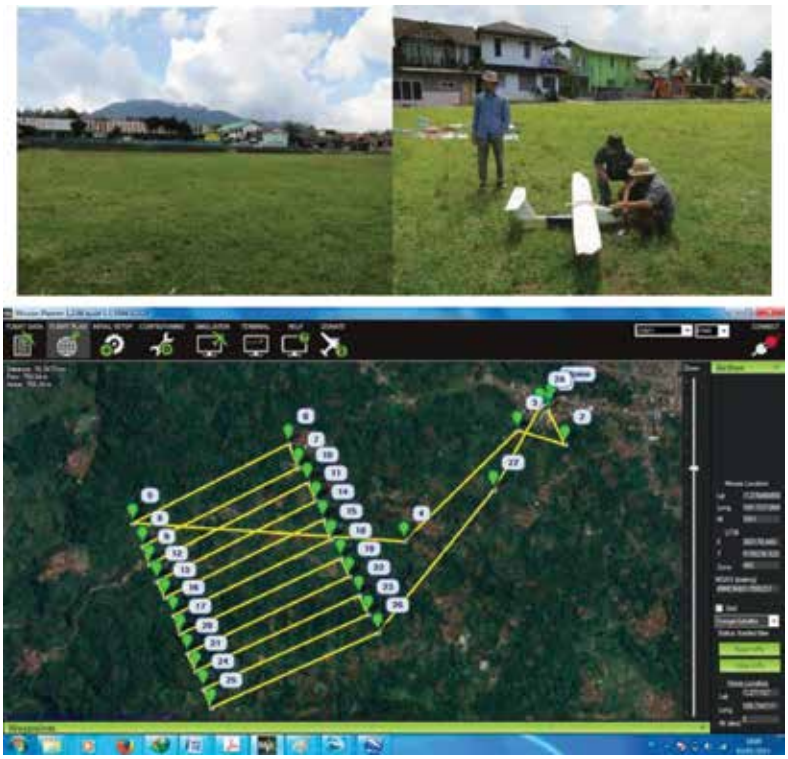

Figure 11. Top left: basecamp condition shows no appropriate runway for takeoff and landing of the LSU, top-right: pre-flight inspection, bottom: flight plan of the landslide mission shows 28 waypoints in total.

shall climb from altitude 1023 m MSL to the 1323 m MSL. The climb phase uses the step climb method from altitude 0 to 80 m AGL (waypoint 2), 80 to 200 m AGL (waypoint 3), 200 to 250 m AGL (waypoint 4) and finally 250 to 300 m AGL (waypoint 5). After reaching the mission altitude, the LSU-01 captures the aerial photography in 11 photographic path (waypoint 5–26). Using this scenario, the LSU-01 able to produce aerial photo that cover the major landslide, imminent landslide, and potential landslide location. **Figure 12** shows the result of this mission. The affected area of the landslide is large. The landslide hit the roads, buried 35 houses and more than 100 peoples [15].

3.3. Aerial photography for mapping the Indonesian army exercise zone

The Indonesian armed force has many exercise zones to train their soldier. One of the exercise zones located in the North Sumatra is called as "daerah latihan tempur Negeri Dolok Kodam I Bukit Barisan." The Indonesian armed force needs the topography map of the exercise zone. The map shall have good quality and good accuracy. Therefore, Indonesian armed force asks the aeronautic technology center for support.

The initial survey indicated that the total mission area is 12,200 hectares. The takeoff and landing place is available too. However, the farthest distance from takeoff and landing place to the mission area is 30 km, while the shortest is 15 km. The UAS shall fly 30 km to the mission area

Figure 12. The landslide in Banjarnegara, 18 December 2014.

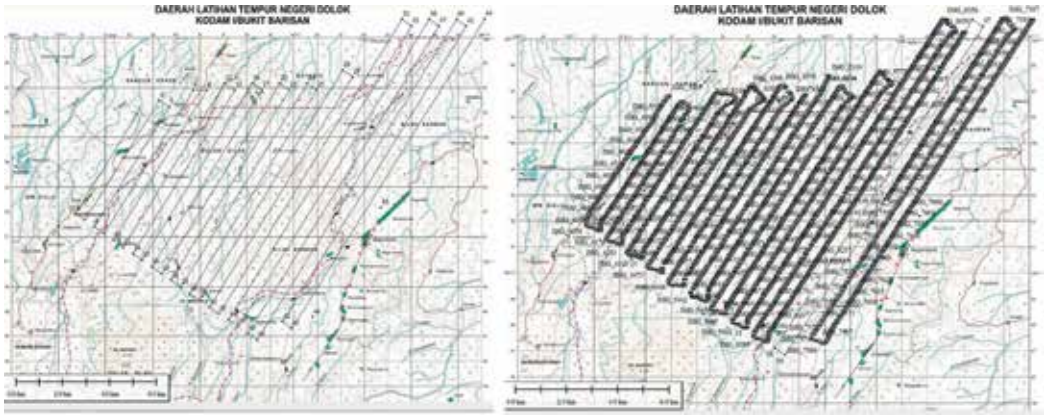

Figure 13. Left: the flight planning of the LSU-02 aerial photography mission show 44 waypoints in total; right: the photography data that captured during this mission.

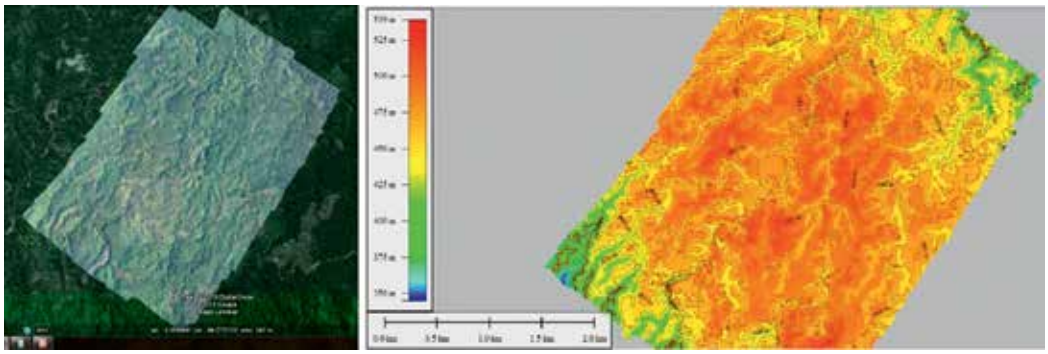

Figure 14. Left: the topography map of the exercise zone; right: the contour map of the exercise zone.

and starting the mission. Based on this situation, The LSU-02 is the best option for handling the mission due to its ability to cover 2500–3000 hectares mission area within one sortie of flight (**Figures 13** and **14**).

Flight sortie	Flight endurance (min)	Fuel available (L)	Total fuel consumption (L)	Flight distance (km)	Fuel consumption / 100 km (L)
First	112	2.5	2.25	126	1.78
Second	84	3.5	1.05	126	0.83
Third	100	3.5	1.80	137	1.31
Fourth	62	2.5	1.30	102	1.27

Table 6. The fuel consumption and flight distance for each flight sortie.

The LSU-02 flies four times to cover the whole mission area at the flight altitude of 300 m. The Sony Alpha A6000 is installed inside the LSU-02 payload bay during this mission. The fuel consumption for each mission sortie is recorded too. **Table 6** shows the fuel consumption as well as flight duration for each mission sortie.

In total, there are 44 waypoints that divided into four flight sortie during this mission. The numbers of photographs are 3348. **Figure 14** shows the result of this mission.

4. Conclusion

With the increase of UAS usage in civilian world, the Aeronautics Technology Center has the important role to keep the contribution in these sectors. The contributions such as the research and development of UAS platform, as well as the dissemination of the research product to the civil world are continuously performed. The capability of LSU family will be improved and upgraded proportioned with the trend and need in civilian world. This chapter only shows a little part of LSU family research, development and dissemination activity that was done by the Aeronautics Technology Center.

Acknowledgements

The authors would like to thank the National Institute of Aeronautics and Space (LAPAN) for the financial support.

Conflict of interest

The authors whose names are listed in this chapter certify that they have NO affiliations with or involvement in any organization or entity with any financial interest (such as honoraria; educational grants; participation in speakers' bureaus; membership, employment, consultancies, stock ownership, or other equity interest; and expert testimony or patent-licensing arrangements), or non-financial interest (such as personal or professional relationships, affiliations, knowledge or beliefs) in the subject matter or materials discussed in this manuscript.

Appendices and nomenclature

AGL	above ground level
APM	Ardu Pilot Mega
COTs	commercially out of the self
ENSO	El Niño/southern oscillation
GPS	global positioning system
GSD	ground sampling distance
LALE	low altitude, long endurance
LASE	low altitude, short endurance
LSU	LAPAN surveillance UAS
MHz	megahertz
MSL	mean sea level
PSBA	Pusat Studi Bencana Alam
RC	radio control
SFAP	small-format aerial photography
UAS	unmanned aircraft systems

Author details

Fuad Surastyo Pranoto*, Ari Sugeng Budiyanta and Gunawan Setyo Prabowo

*Address all correspondence to: fuad.pranoto@lapan.go.id

Indonesian National Institute of Aeronautics and Space (LAPAN), Aeronautic Technology Center, Bogor, Indonesia

References

[1] Lee HS. General rainfall patterns in Indonesia and the potential impacts of local seas on rainfall intensity. Water. 2015;**7**:1751-1768. DOI: 10.3390/w7041751

[2] Asian Development Bank. Indonesia Country Water Assessment. Manila: ADB; 2016. pp. 3-5. E-ISBN: 978-92-9257-361-4

[3] Ministry of Environment. Status Lingkungan Hidup Indonesia 2012. Jakarta: Ministry of Environment; 2013

[4] The World Bank. Indonesia, the Rise of Metropolitan Regions: Towards Inclusive and Sustainable Regional Development. Jakarta: National Development Planning Agency; 2013. pp. 10-12

[5] Case M, Ardiansyah F, Spector E. Indonesia, Climate Change in Indonesia. Jakarta: WWF. pp. 01-13

[6] Pribadi KS, Kusumastuti D, Rildove. Learning from recent Indonesian earthquakes: An overview to improve structural performance. In: Proceedings of the 14th World Conference on Earthquake Engineering; 12-17 October 2008; China, Beijing: WCEE; 2014. pp. 1-8

[7] Miyamoto HK, Gilani AS. Recent earthquakes in Indonesia and Japan: Observed damage and retrofit solutions. In: Proceedings of the 14th World Conference on Earthquake Engineering; 12-17 October 2008; China, Beijing: WCEE; 2014. pp. 1-8

[8] Aber JB, Marzolff I, Ries JB. Small-Format Aerial Photography: Principles, Techniques, and Geoscience Applications. 1st ed. Oxford: Elsevier; 2010. pp. 15-25. ISBN: 978-0-444-53260-2Ch2

[9] Hickin EJ. Maps and Mapping. A Cartographic Manual. Burnaby: R.S. Graphics and Printing; 2014. pp. 74-76. Ch7

[10] Neumann KJ. Digital Aerial Camera [Report]. Aalen: Deutchland Integraph Z/I GmbH; 2006

[11] Pranoto FP, Prabowo GS. Economic analysis of small format aerial photography mission utilizing the LSA-01 UAV. International Journal of Unmanned Systems Engineering. 2015;**3**:31-39. DOI: 10.14323/ijuseng.2015.11

[12] Canon EOS-1D X Mark II [Internet]. Available from: https://downloads.canon.com/nw/camera/products/eos/1d-x-mark-ii/specifications/canon-eos-1dx-mkii-specification-chart.pdf [Accessed: May 03, 2018]

[13] Canon PowerShot S100 [Internet]. Available from: https://en.wikipedia.org/wiki/Canon_PowerShot_S100 [Accessed: May 03, 2018]

[14] ILCE-6000 [Internet]. Available from: https://www.sony.com/electronics/interchangeable-lens-cameras/ilce-6000-body-kit/specifications [Accessed: May 03, 2018]

[15] Satu Dusun Tertimbun Tanah Longsor di Banjarnegara, Jawa Tengah [Internet]. 2014. Available from: https://www.voaindonesia.com/a/satu-dusun-tertimbun-di-banjarnegara-jawa-tengah/2557623.html [Accessed: January 03, 2018]

Section 3

Drone Design

Chapter 3

Smart Arduino Sensor Integrated Drone for Weather Indices: Prototype

Hanping Mao, Oppong K. Paul, Ning Yang and Lin Li

Additional information is available at the end of the chapter

http://dx.doi.org/10.5772/intechopen.76872

Abstract

Mostly, the conditions within an ecosystem as well as weather of a field affect crop productivity greatly. Different weather conditions produce different effects and different impact on the quality of the crop field or the ecosystem. Weather elements form a chain reaction, as the atmosphere is not the only one being affected. Atmospheric air temperature, vapor pressure and relative humidity or moisture content can act together and form diverse effects on crops. These diverse effects turn to reduce radiation which is necessary for plants, or increase rainfall patterns. Consistent high temperatures can increase the heat transfer to local bodies of water in addition to heating the air. Monitoring the climate and the weather conditions are important not only as an environmental baseline, but to maintain quality working conditions, marine studies and recreational safety. The parameters of climate are measurable, for example, atmospheric vapor pressure, temperature, precipitation and solar radiation, can be captured and recorded daily on the Smart Arduino Sensor Integrated Drone. Means and extreme datasets, maximum and minimum weather trends with deviations of lengthy time series would be calculated for each of these climate parameters which were considered in this study. These results are a simple form of climate indices, as they already describe changes in climate. All the readings and datasets are recorded on a cloud platform, as well as, in an installed microchip on the drone. Data synchronization is done with MAT-LAB and Arduino Programming Rule.

Keywords: Arduino, MATLAB, sensor, weather data, rain-cap, wind-cap, environment

1. Background to the proposed work

Climate and weather data monitoring which gives vivid and exact information for farming purposes goes beyond weather stations. Interesting enough, every farmer needs to know and monitor the weather if high productivity is to be met.

Research has it that, agricultural productivity relies directly and indirectly on the weather and climatic conditions. Therefore failure to adhere to the weather before, during and after farming renders crop production susceptible to unsuspected disease attacks that are caused or influenced by certain weather conditions [1]. This research is intended to meet the demand for easy-to-use, easy-to-access, and accurate weather data for farmers using a drone (UAV) with mounted Arduino Sensors to give accurate climate information to farmers in crop production especially rainfall, solar (duration and intensity) and temperature.

This Arduino Drone is been built and developed in Jiangsu University—Zhenjiang, China P.R, with state-of-the-art multi-parameter weather sensors which focus on four main weather parameters—radiation, temperature, rainfall, and humidity all in one compact, lightweight instrument called Smart Arduino Drone. There are readings for other weather parameters but the focus is on the above four data set as they have direct or indirect effect on crops at a higher rate considering rice production in Zhenjiang, China.

This Smart Arduino Drone is built with easy setup and synchronization with the controller and stored memory for computer reading and analysis. It will need minimal technical know-how to install, integrate, and maintain. The main focus is to monitor the weather conditions on a rice field, tea farm, maize or vegetable fields as these crops require different conditions for optimal productivity.

The Arduino Board which controls the sensors runs on the Arduino Software and MATLAB data logins and it will give users an automatic data collection and the option of real-time data posting through the Internet due to the onboard GPS (Beidou) system.

1.1. Aims and objectives

This study mainly focuses on developing a high-resolution weather data indices for farmers using a Smart Drone. Again the Smart Drone is designed to record accurate weather readings which are far less labor-intensive over the traditional, manual counterpart of weather data recording at a weather station.

Specifically, this study seeks to estimate missing values in weather data by regularized expectation maximization also called RegEM, and to homogenize weather dataset by Quantile Matching Adjustment, referred to as QMadj [2].

1.2. Evidence of research or justification

1.2.1. Surface climate and data reconstruction

Climate data provide great depth of information about the atmosphere that impacts almost all ecosystem of human life [3]. Global change research and impact studies are highly dependent on the description of the mean state and variability of recent climate [2]. As such, continuous and quality climate datasets are precursors for excellent climate-impact studies especially for modern farmers. An example is the indication by [4] that high spatial and temporal rainfall resolutions were needed for urban drainage and urban flood modeling applications.

Various mathematical approaches have been applied widely for data reconstruction in many climate datasets. This project will give first-hand information to the farmer directly on the farm and crop performances can be monitored. Herman et al. [5] constructed a comprehensive archive of Australian rainfall and climate data from ground-based observational data using spatial interpolation algorithms, so this project is justified due to the new way and method of monitoring the weather parameters for crop production.

2. Materials and method

2.1. Materials

- Site: Zhenjiang rice fields

The Drone considered for this project is DJI with Model Number Matric 600, Phantom 4 Pro. This drone is built to carry up to 13 pounds and produce all the thrust needed by relying on six rotor systems with each been powered by an actively cooled motor [6]. The Drone controller is an A3 Flight with six separate batteries that switches on automatically should one fail [6].

Arduino Board and Sensors: Temperature, Relative Humidity, Precipitation/Rainfall and Solar radiation (Duration & Intensity), Beidou, Wind Sensor (Speed and Direction), and Digital Camera. Software is Arduino Programmer, and Mat Lab for Data Synchronization.

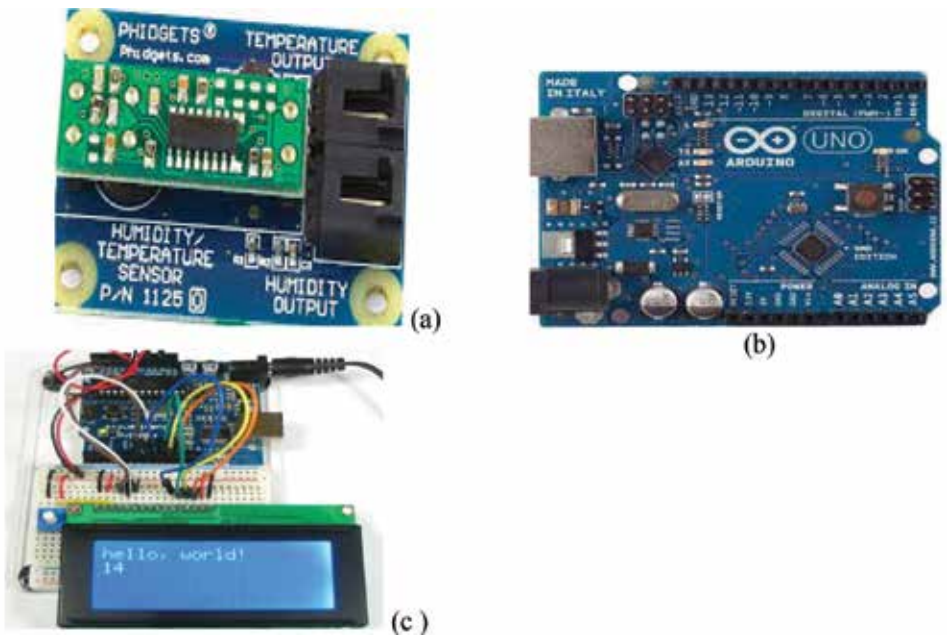

Figure 1. (a) Temperature and humidity sensor, (b) Arduino board mount, (c) Arduino board mount.

2.1.1. Methodology and scope of the project

The Smart Arduino Sensor Drone will fly and record weather data and communicate the information to the farmer (Crop Production Fields) directly on a computer. The Arduino Sensor and the drone has been designed to quickly discover the key weather elements to making a successful farming with requirements to rice, tea, maize and some selected vegetable fields. It is been built as a hands-off, easy to use and as industry specific as possible.

First, The Arduino Board called TuxCase would be mounted on the base plate of the built UAV (Drone) using the flat-head screws. After this, the Arduino sensors would be placed inside the TuxCase as shown in **Figure 1a–c** [7], and fastened into the case using the four shorter (1/4″) screws that came with the Arduino TuxCase kit.

Secondly, the colorimeter shield would be mounted onto the Arduino board which has only one orientation possible together with the weather parameter sensors by following the shield pins which are labeled on the silkscreen (white text) to match the label on the corresponding header on the Arduino board (**Figures 2–4**).

The synchronization process would be done using the Arduino Programming Rule, all the four sensors would be programed to record the weather information which will then be stored on a cloud and an installed microchip. The weather parameters of interest (rainfall, temperature, humidity and solar) would then be captured by the Arduino Sensors and processed by

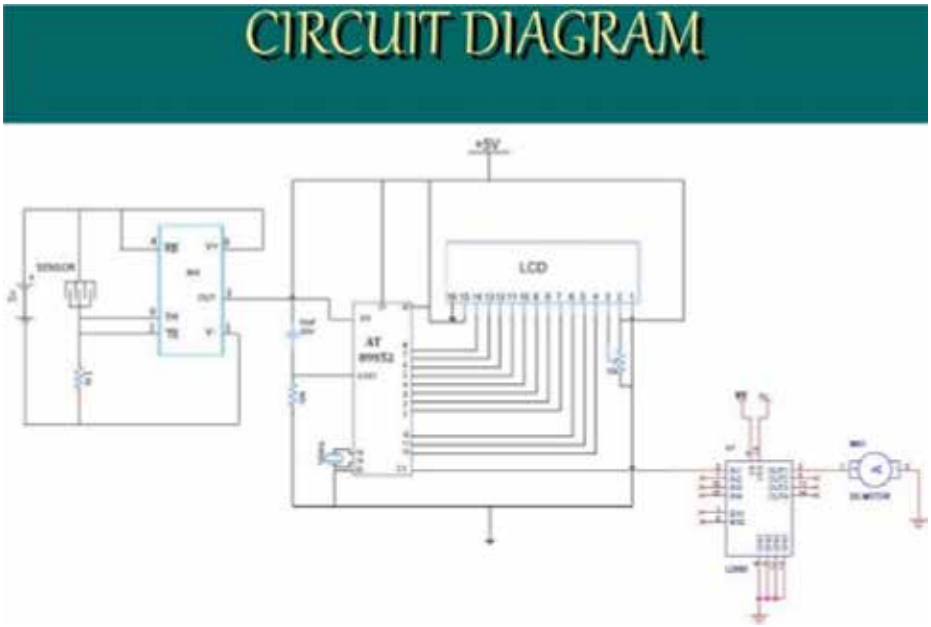

Figure 2. Circuit diagram for Arduino Connection.

http://dx.doi.org/10.5772/intechopen.76872

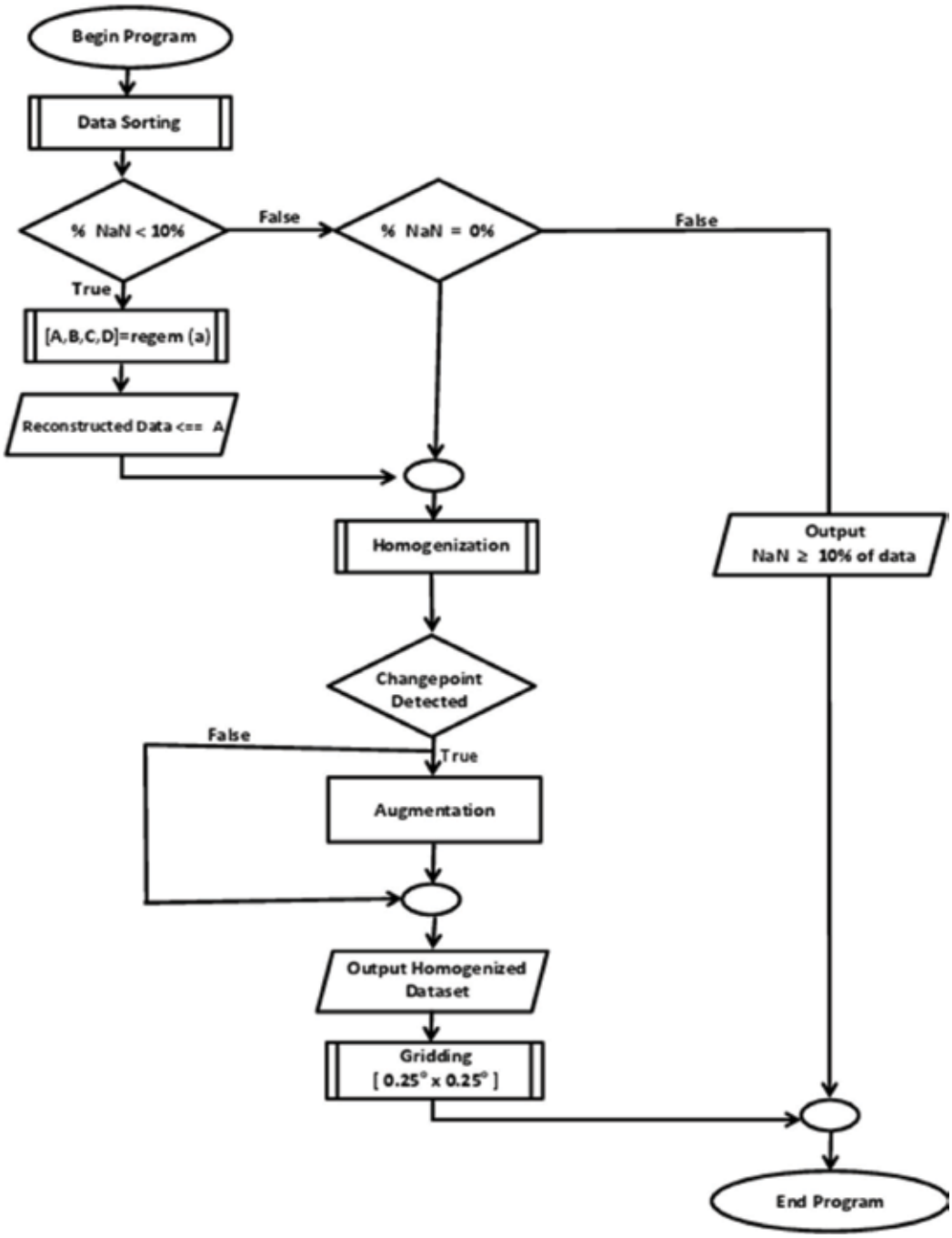

Figure 3. Arduino Programming Rule Interface: Flowchart of data gap estimation, homogenization and gridding steps that will be carried out in this study.

Figure 4. Smart Arduino sensor integrated drone.

MATLAB Software. The frequencies at which weather data can be collected, its quality and its ability to be processed, managed and stored becomes critical to how useful this Smart Arduino Sensor can be.

2.2. The Arduino and MATLAB programing

The structure of the Arduino programming language runs in at least two parts. These two required parts, or functions, enclose blocks of statements [8]. The setup function should follow the declaration of any variables at the very beginning of the program.

2.3. Data captured by the Smart Arduino drone

- **Rainfall (intensity, and duration)** would be measured using the Arduino RAINCAP Sensor, which is the only maintenance-free rainfall sensor. The rainfall sensor measures raindrops. The impacts will give signals which will be proportional to the intensity of the drops. The sensor will then convert the signal from each drop into rainfall, intensity, and duration. This RAINCAP sensor can even distinguish different types of rain such as Relief or Frontal [9].
- **Temperature, relative humidity** these sensors rely on Arduino's proven technology and experience, and provide highly accurate and stable readings based on the geological location of the flying drone. The unit calibration is done using the Arduino Software.

- **Solar (duration and intensity), wind speed and direction** are measured ultrasonically with Arduino's advanced WINDCAP sensor and Solar sensor.

All the sensors within the Smart Arduino Drone would be calibrated using the Arduino Software and data analysis done by MATLAB. After all the sensors are mounted on the Arduino board, the Smart Arduino Drone needs to be aligned, connected to a data logger (computer) and power source (Battery). Flying height of the drone depends on the individual but it is estimated that, flying higher allows you to cover more ground in a shorter amount of time with less battery usage.

3. Expected results: auto piloting sample

From the table above (**Table 1**), the Smart Arduino Drone on trial recorded data in Zhenjiang indicating that, Zhenjiang is a warm temperate ecological zone. The data used (**Table 1**) shows that, there is significant rainfall throughout the year in Zhenjiang.

Even the driest month still has a lot of rainfall. According to [10], this climate is classified as Humid Tropical Climate (Cfa). The average annual temperature is 15.5°C in Zhenjiang.

Monthly rainfall totals of the four districts are presented with each entry representing the probable range of monthly rainfall total for any grid that lies within a particular zone. Dantu district records monthly rainfall peaks of about 300 mm in any of the months between June and September. Jurong District the zone with the overall highest cumulative rainfall amount

Month	**Rainfall (mm)**			
	Dantu	**Danyang**	**Jurong**	**Yangzhong**
January	<100	<100	<100	<100
February	<100	<100	<150	<100
March	<150	<150	<250	<150
April	50–200	50–200	100–250	50–200
May	50–200	50–200	100–350	100–250
June	100–300	100–300	150–450	100–300
July	100–300	100–300	100–250	<200
August	100–300	100–300	50–200	<150
September	50–300	50–300	50–300	<150
October	50–150	50–200	50–300	<200
November	<100	<100	<200	<100
December	<100	<100	<100	<100

Table 1. Autopiloting estimates of monthly rainfall in four districts of Zhenjiang.

Month	Rainfall (mm)			
	Dantu	Danyang	Jurong	Yangzhong
Dec–Jan–Feb	<300	<300	<400	<400
Mar–Apr–May	100–500	100–500	100–900	100–700
Jun–Jul–Aug	200–800	200–800	300–800	200–600
Sep–Oct–Nov	200–600	200–600	200–800	100–500
Annual	600–1800	800–2000	900–2000	600–1400

Table 2. Autopilot estimates of seasonal & annual rainfall in the four districts (agro-ecological zones).

(450 mm) amongst the four districts of Zhenjiang agro-ecological zones, whereas Yangzhong district is the zone with the least cumulative rainfall amount.

Yangzhong district has rainfall pattern similar to that of Jurong district, however, rainfall amounts over the Yangzhong district is lesser.

Table 2 shows autopilot estimates of seasonal rainfall totals for the four agro-ecological zones, with each column representing the range of rainfall total for any grid lying within a particular zone. Jurong district (zone) has an all-year maximum seasonal rainfall, with Yangzhong district recording the least seasonal rainfall. In all districts, the second trimester was found to be the rainfall onset over the country and thus, is the best season for farmers to engage in planting.

The third trimester, is identified as the season of probable extreme events over the entire Zhenjiang, and the very first trimester, however, is the driest period over the entire Zhenjiang.

3.1. Success criteria: autopilot clearness index over Zhenjiang

The transparency of the atmosphere over Zhenjiang is an all-important parameter, for the solar radiation potential of the city. It is indicated by the fraction of extraterrestrial solar radiation which reaches the earth surface as global radiation, and thus is a measure of the degree of the clearness of the sky, or the clearness index [11]. **Figure 5** shows the clearness index over Zhenjiang for both Smart Drone estimated and weather station datasets.

It is shown in **Figure 5b** that clearness index has an estimated value greater than 50% for all the four agro-Meteorological zones or districts. The monthly average maximum and minimum estimated clearness index for the study area is 59 and 47.8%.

This indicates a moderately transparent sky across the Zhenjiang city. Jurong district however, shows the lowest clearness index value of 54%. This is not unexpected as it can be attributed to a bi-modal heavy rainfall and very low temperature regimes over the district [12]. The atmosphere here is thus characteristically moisture gladdened, with relatively high convective atmosphere. This affords the district a greater effect of atmospheric attenuation hence low atmospheric transparency.

The implication of having mean clearness index greater than 50% is that the sky is moderately transparent throughout the study area (Zhenjiang), confirming clear sky conditions and show

http://dx.doi.org/10.5772/intechopen.76872

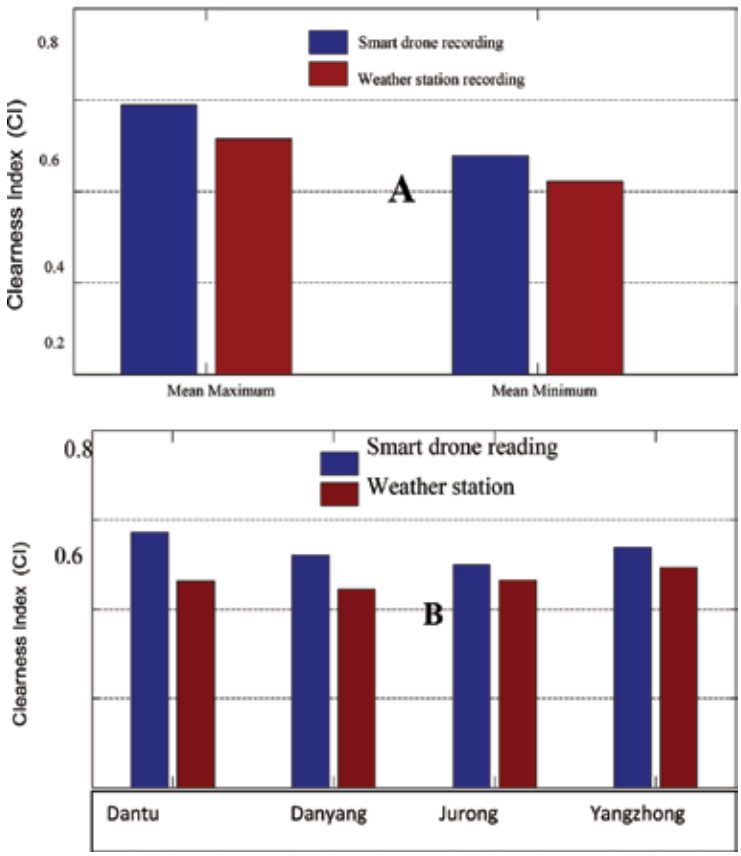

Figure 5. Clearness index (CI) over Zhenjiang: (a) represents the monthly mean maximum and minimum CI over the country and (b) represents clearness index (CI) for all the four districts (agro-ecological zones).

that the amount of solar radiation on a horizontal surface is sufficient for solar energy utilization in Zhenjiang city.

The weather station clearness index is relatively low compared with the estimated clearness index by the Smart Drone. This is expected since the Meteosat-7 satellite observed Global Horizontal Irradiation, (GHI) by the clear-sky model developed by the SWERA-partner SUNY (State University of Albany, New York), which was implemented by [13].

4. Conclusion

It is expected that, based on the autopilot data already generated, the Smart Arduino Sensor Integrated Drone will predict the average means of temperature, rainfall, wind (direction and speed) solar patterns of Zhenjiang community in China. This Smart Drone in agriculture is a big boost to farmers because it carries the potential of completely transforming and revolutionizing the farming and agriculture industry.

Weather parameter reading, soil health scans, monitoring crop health, applying fertilizers and watering the fields, even tracking weather and estimating yields, and then collecting the data and analyzing it for prompt action are some elements considered in this ongoing project.

All in all, this Smart Arduino Integrated Drone can mechanize every step of farming and eliminate the costs of human errors and enable farmers to react quickly to threats (such as drought conditions and flood), helping with maximization of income and returns on investment crop productivity.

This Smart Drone in agriculture is a big boost to farmers because it carries the potential of completely transforming and revolutionizing the farming and agriculture industry.

Author details

Hanping Mao, Oppong K. Paul*, Ning Yang and Lin Li

*Address all correspondence to: lifejnr@yahoo.com

School of Agricultural Equipment Engineering, Jiangsu University, Zhenjiang, Jiangsu, P.R China

References

[1] Acheampong AA, Fosu C, Amekudzi LK, Kaas E. Perceptible water comparisons over Ghana using PPP techniques and reanalysis data. 2017;**6**(3):449

[2] Lowe EF, Battoe LE, Coveney MF, Schelske CL, Havens KE, Marzolf ER, Reddy KR. The restoration of Lake Apopka in relation to alternative stable states: An alternative view to that of Bachmann et al. (1999). Hydrobiologia. 2001;**448**(1-3):11-18

[3] Siqueira MFD, Peterson AT. Consequences of global climate change for geographic distributions of cerrado tree species. Biota Neotropica. 2003;**3**(2):1-14

[4] Segond ML, Tabary P. 10.5 quantitative precipitation estimations from operational polarimetric radars for hydrological applications. 2007

[5] Herrmann JW, Lin E, Al E. Affordable space systems manufacturing: Intelligent synthesis. Paper presented at the CD-ROM ASME Design Engineering Technical Conferences & Computers & Information in Engineering Conference; 2001

[6] Clark DR, Meffert C, Baggili I, Breitinger F. DROP (DRone Open source Parser) your drone: Forensic analysis of the DJI Phantom III. Digital Investigation. 2017;**22**:S3-S14

[7] Havenith MN, Yu S, Biederlack J, Chen NH, Singer W, Nikolić D. Synchrony makes neurons fire in sequence, and stimulus properties determine who is ahead. Journal of Neuroscience, The Official Journal of the Society for Neuroscience. 2011;**31**(23):8570

[8] Arakliotis S, Nikolos DG, Kalligeros E. LAWRIS: A Rule-Based Arduino Programming System for Young Students. Paper presented at the International Conference on Modern Circuits and Systems Technologies; 2016

[9] Cerveny R. Hamilton and the hurricane. Weatherwise. 2016;**69**(5):42-48

[10] Tubiello FN, Amthor JS, Boote KJ, Donatelli M, Easterling W, Fischer G, et al. Crop response to elevated CO and world food supply: A comment on "Food for Thought…" by Long et al., Science 312:1918-1921. European Journal of Agronomy. 2007, 2006;**26**(3):215-223

[11] Curry JM, Ohnson ER, Tarnes JH. Effect of dropped plies on the strength of graphite-epoxy laminates. AIAA Journal. 2015;**30**(2):449-456

[12] Toledo-Aceves T, Swaine MD. Biomass allocation and photosynthetic responses of lianas and pioneer tree seedlings to light. Acta Oecologica. 2008;**34**(1):38-49

[13] Imam S, Yilmaz S, Sohmen U, Gorzalski AS, Reed JL, Noguera DR, Donohue TJ. iRsp1095: A genome-scale reconstruction of the Rhodobacter sphaeroides metabolic network. BMC Systems Biology. 2011;**5**(1):116

Chapter 4

Generalized Control Allocation Scheme for Multirotor Type of UAVs

Denis Kotarski and Josip Kasać

Additional information is available at the end of the chapter

http://dx.doi.org/10.5772/intechopen.73006

Abstract

Unmanned aerial vehicles (UAVs) are autonomous or remotely guided aircraft, which can potentially carry out a wide range of tasks. Multirotor type of UAV has unique ability to perform vertical take-off and landing (VTOL), a stationary and low-speed flight where certain configurations can achieve very complex and precise movements. Therefore, they are suitable for performing tasks such as delivery of first aid kit, firefighting, infrastructure inspection, aerial video, and many others. In this chapter, a generalized control allocation scheme for a multirotor UAV is presented, which describes the mapping of rotor angular velocities to the control vector of the aircraft. It enables control and design of multirotor configurations with diverse geometrical arrangement and characteristics of the propulsion subsystem depending on the task, which multirotor has to carry out. The inverted scheme, which is implemented as a motor mixer, maps the control inputs into a set of aircraft actuator outputs.

Keywords: multirotor UAV, VTOL, control allocation scheme, propulsion subsystem, motor mixer

1. Introduction

Unmanned aerial vehicles (UAVs) can be defined as autonomous or remotely guided aircrafts, which do not require the onboard human crew during operation; so, it is expected that they would be used in a wide range of tasks and operated in harmful conditions. The development of new technologies, especially microelectromechanical systems (MEMS), and an increase of the control units' computer power have enabled rapid progress and a large number of interesting applications. There are several categories of UAVs, which are in various stages of research, development, and application (rotary-wing, fixed wing, flapping-wing, blimp, and hybrid UAV). Rotary-wing UAVs have the ability to carry out vertical take-off and landing

(VTOL), stationary and flight at moderate speed making them suitable for performing tasks without the need for a runway or a launch pad.

Multirotors are the type of rotary-wing UAVs with fixed pitch wings and propellers. Since they are typically small in size with extreme agility and maneuverability, multirotors belong to micro aerial vehicles (MAVs). They are suitable for use in aerial photography, surveillance, infrastructure inspection, precise agricultural, search and rescue missions [1, 2], delivery, and many other tasks. Multirotors have six degrees of freedom (DOF); it is assumed that the aircraft is symmetrical and rigid, and the only moving parts are rotors with the propellers connected to the rotor axis. Rotors angular velocities are the only variables that have a direct impact on the multirotor dynamics [3]. From a control perspective, multirotors are represented as highly nonlinear multivariable systems because coordinate system transformations include trigonometric functions and aerodynamic forces that are proportional to the squared rotor speed. If the functionality of control loops is lost, multirotor will crash, because it is inherently unstable system and cannot return to equilibrium state by itself. Given that the only variables are the rotor (propulsion) subsystem angular velocities, multirotor configurations can be classified according to the propulsion arrangement.

The design and development of multirotors are constrained by the size, weight, and power consumption [4]. The most common and by far the most used multirotor configuration is the one with four rotors, quadrotor [5, 6], which is suitable for the evaluation of control algorithms [7, 8]. Performing certain tasks such as the lifting of heavy equipment requires configurations which have six, eight or more rotors. Configurations may consist of single (hexarotor, octorotor) and coaxial [9] (Y6 and X8 rotor) propulsion arrangements, in which various control units have built-in or with overlapping arrangements [10]. These configurations have the characteristic of a parallel geometric rotor arrangement and can be classified as flat multirotor configurations. As a result of growing interest in development and application of multirotor UAVs where some tasks require longer flight time or complex and precise aircraft movements, an increasing number of new configurations are emerging. By properly selecting propulsion arrangement, it is possible to improve certain properties such as an increase in flight time [11]. Several papers deal with the novel configurations with actively tilted rotors [12, 13] in order to overcome the underactuation limitation of conventional flat multirotor configurations. A novel overactuated quadrotor UAV based on actively tilted rotors is proposed in [14]. Actively tilted configurations require an additional number of actuators, which makes the system more complex and also increases weight and power consumption. Therefore, passively tilted nonflat multirotor configuration, such as presented in paper [15], is more suitable for analysis and realization. The drawback of the mentioned papers is the limitation in the mathematical representation of configurations so that the analysis is also limited to certain properties.

In this chapter, a nonlinear mathematical model of the multirotor UAV is described. The model is decomposed into a rigid body dynamic model, derived by using Newton-Euler method and control allocation scheme, which describes a mapping of rotor angular velocities to a control vector. Control allocation matrix, whose rank determines whether the configuration is underactuated or fully actuated, is defined with rotors geometric arrangement and propulsion physical parameters. Through open loop simulations, the implemented model enables the analysis

of dynamics and energy consumption for different generic multirotor configurations, so it is possible to design diverse multirotor UAVs for various tasks. The fact that the nonflat design can provide six independent control variables, one for each degree of freedom, has a significant influence on the motion planning and control design. Fully actuated configurations provide the more efficient realization of different task objectives, which require complex movements such as tasks involving manipulation with objects in the presence of external forces. The inverted scheme, implemented in a flight controller as a motor mixer, maps the control vector to actuator commands.

2. Preliminary system descriptions

The mathematical model of the multirotor UAV is a function that is mapping input angular velocities of rotors to output position and orientation of the aircraft, which is required for the design and synthesis of control algorithms. The model describes multirotor behavior that is important for dynamics and energy consumption analysis of different configurations.

2.1. Reference coordinate systems

To describe the multirotor dynamic model, it is necessary to define the inertial coordinate system (Earth frame) and the aircraft system (body frame). Earth frame is defined as an inertial right hand Cartesian coordinate system connected to earth's surface with z-axis direction normal to ground level. Earth frame does not rotate, which means that the law of inertia is directly applicable. Multirotor position $\boldsymbol{\xi} = [X \;\; Y \;\; Z]^{\mathrm{T}}$ is determined by the coordinates of the vector, which connects the origin of Earth frame with the origin of body frame. Multirotor orientation $\boldsymbol{\eta} = [\phi \quad \theta \quad \psi]^{\mathrm{T}}$ is determined by three Euler angles describing the orientation of the body frame in relation to the Earth frame. Rotation around the X axis is defined as the roll angle ϕ, rotation around the Y axis as the pitch angle θ, and rotation around the Z axis as the yaw angle ψ.

Body frame is fixed on the multirotor body and it is also right hand Cartesian coordinate system. The assumption is that the origin of body frame coincides with the multirotor center of gravity (COG) and that the principal inertia axes of multirotor body coincide with the body frame coordinate axes. Since the frame is fixed to the rotating multirotor body, the inertia forces are added to Newton's laws of motion. The inertia matrix is time-invariant and also reduced to diagonal matrix due to the symmetry of the multirotor body. Multirotor linear (translational) velocities $\mathbf{v}^B = [u \quad v \quad w]^{\mathrm{T}}$ and angular (rotational) velocities $\boldsymbol{\omega}^B = [p \quad q \quad r]^{\mathrm{T}}$ are defined in the body frame. Since the onboard sensors and propulsion subsystem are defined with respect to the body frame, it is more suitable to formulate the motion equations, force vector $\mathbf{F} = [F_X \quad F_Y \quad F_Z]^{\mathrm{T}}$, and moment vector $\mathbf{T} = \left[T_\phi \quad T_\theta \quad T_\psi\right]^{\mathrm{T}}$ in the body frame.

2.2. UAV kinematic model

Assuming that the multirotor is a rigid body, translational and rotational motion can be described as the motion of the particle located at the body COG. It follows that the description

of the multirotor motion is reduced to the description of the translation and rotation of the body frame. Kinematics of a UAV with six DOF is described by

$$\begin{bmatrix} \dot{\boldsymbol{\xi}} \\ \dot{\boldsymbol{\eta}} \end{bmatrix} = \begin{bmatrix} \mathbf{R} & \mathbf{0}_{3\times3} \\ \mathbf{0}_{3\times3} & \boldsymbol{\Omega}_B \end{bmatrix} \begin{bmatrix} \mathbf{v}^B \\ \boldsymbol{\omega}^B \end{bmatrix} \tag{1}$$

where $\dot{\boldsymbol{\xi}}$ is the linear and $\dot{\boldsymbol{\eta}}$ is the angular velocity vector in Earth frame, $\mathbf{R}$ is an orthogonal rotation matrix, which maps the linear velocity vector from Body to Earth frame, and $\boldsymbol{\Omega}_B$ is transformation matrix, which maps the angular velocity vector from Body to Earth frame.

Using the Euler's rotation theorem, rotation of Earth frame to body frame is described with three consecutive rotations around the known axes. Since the rotation matrix is mapped from Body to Earth frame, inverse rotations need to be calculated,

$$\mathbf{R} = \mathbf{R}^T(\psi, Z)\mathbf{R}^T(\theta, Y)\mathbf{R}^T(\phi, X) \tag{2}$$

where $\mathbf{R}(\psi, Z)$ denote the 3×3 elemental rotational matrix, which describes the rotation around the Z axis for the yaw angle ψ. As shown in **Figure 1**, the rotation result is an auxiliary coordinate system with axes (X_1, Y_1, Z),

$$\mathbf{R}(\psi, Z) = \begin{bmatrix} c_\psi & s_\psi & 0 \\ -s_\psi & c_\psi & 0 \\ 0 & 0 & 1 \end{bmatrix} \tag{3}$$

where $c_i = \cos(i)$ and $s_j = \sin(j)$. The matrix $\mathbf{R}(\theta, Y)$ describes the rotation around the Y_1 axis for the pitch angle θ. The rotation result is an auxiliary coordinate system with axes (X_B, Y_1, Z_1),

$$\mathbf{R}(\theta, Y) = \begin{bmatrix} c_\theta & 0 & -s_\theta \\ 0 & 1 & 0 \\ s_\theta & 0 & c_\theta \end{bmatrix} \tag{4}$$

The matrix $\mathbf{R}(\phi, X)$ describes the rotation around the X_B axis for the roll angle ϕ. The rotation result is the body frame with the axes (X_B, Y_B, Z_B),

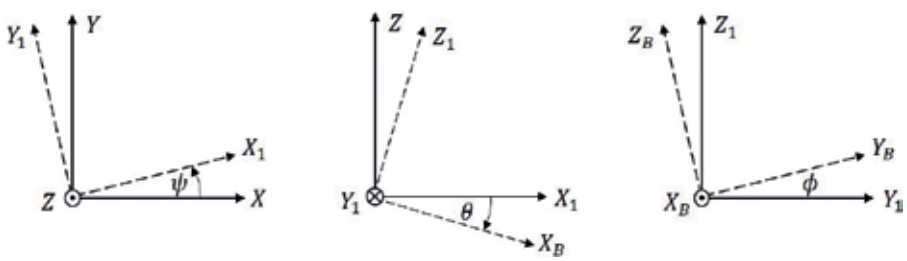

Figure 1. Illustration of Euler rotations.

$$\mathbf{R}(\phi, X) = \begin{bmatrix} 1 & 0 & 0 \\ 0 & c_\phi & s_\phi \\ 0 & -s_\phi & c_\phi \end{bmatrix} \tag{5}$$

Since angular velocities occur around an axis, the angular velocity is not mapped by rotation matrix. The rate of yaw angle occurs around the Z axis, rate of pitch angle around the Y_1 axis, and rate of roll angle occurs around the X_B axis. Using elemental rotation matrices, it is possible to transform the angular velocity vector from the Earth frame into the body frame,

$$\begin{bmatrix} p \\ q \\ r \end{bmatrix} = \begin{bmatrix} \dot{\phi} \\ 0 \\ 0 \end{bmatrix} + \mathbf{R}(\phi, X) \begin{bmatrix} 0 \\ \dot{\theta} \\ 0 \end{bmatrix} + \mathbf{R}(\phi, X)\mathbf{R}(\theta, Y) \begin{bmatrix} 0 \\ 0 \\ \dot{\psi} \end{bmatrix} \tag{6}$$

Eq. (6) can be written as $\boldsymbol{\omega}^B = {\boldsymbol{\Omega}_B}^{-1}\dot{\boldsymbol{\eta}}$ from which we get an inverse transformation matrix ${\boldsymbol{\Omega}_B}^{-1}$ that enables the calculation of $\boldsymbol{\Omega}_B$.

2.3. Multirotor UAV dynamic model

Multirotor dynamics is described by a multivariable nonlinear model, which consists of six second-order differential equations. It is derived by using the Newton-Euler method based on Euler's laws of motion, considering the assumptions that the body frame origin coincides with the aircraft COG and that the axes of the body frame coincide with the principal inertia axes of the multirotor body.

2.3.1. Translational dynamics

The translational (linear) motion of a rigid body based on the first Euler law with respect to the body frame is described by

$$m\dot{\mathbf{v}}^B + \boldsymbol{\omega}^B \times \left(m\mathbf{v}^B\right) = \mathbf{F} \tag{7}$$

where m is aircraft mass. The translational dynamics of the multirotor system is influenced by the force vector given with propulsion and external forces caused by the environment

$$\mathbf{F} = \mathbf{g}_B + \mathbf{d}_f + \mathbf{f} \tag{8}$$

Force vector is divided into gravitational $\mathbf{g}_B$, disturbance force $\mathbf{d}_f = [\, d_{mX} \quad d_{mY} \quad d_{mZ} \,]^{\mathrm{T}}$, and propulsion subsystem force vector $\mathbf{f} = \begin{bmatrix} f_X & f_Y & f_Z \end{bmatrix}^{\mathrm{T}}$. The gravitational force vector has a direction parallel to the Z axis in the Earth frame $\mathbf{g}_E = [\, 0 \quad 0 \quad mg \,]^{\mathrm{T}}$. In the body frame, it is defined by rotation matrix $\mathbf{g}_B = \mathbf{R}^{\mathrm{T}}\mathbf{g}_E$.

The total translational dynamics with respect to the body frame is given by the equation

$$\dot{\mathbf{v}}^B = m^{-1}\left(-\boldsymbol{\omega}^B \times \left(m\mathbf{v}^B\right) + \mathbf{g}_B + \mathbf{d}_f + \mathbf{f}\right) \tag{9}$$

Since the dynamic model in the Earth frame does not contain the members of the imaginary forces and the gravitational force coincides with the Z axis, the translational dynamics is shown in Earth frame,

$$\ddot{\boldsymbol{\xi}} = m^{-1}\left(\mathbf{g}_E + \mathbf{d}_f + \mathbf{R}\mathbf{f}\right) \tag{10}$$

2.3.2. Rotational dynamics

The rotational (angular) motion of a rigid body based on the second Euler law with respect to the body frame is described by

$$\mathbf{I}\dot{\boldsymbol{\omega}}^B + \boldsymbol{\omega}^B \times \left(\mathbf{I}\boldsymbol{\omega}^B\right) = \mathbf{T} \tag{11}$$

where $\mathbf{I}$ is the inertia matrix. By applying the assumption that the multirotor frame has symmetrical structure, inertia matrix becomes diagonal, which enables simplification of the dynamic model,

$$\mathbf{I} = \begin{bmatrix} I_{XX} & 0 & 0 \\ 0 & I_{YY} & 0 \\ 0 & 0 & I_{ZZ} \end{bmatrix} \tag{12}$$

The rotational dynamics of the multirotor system is influenced by the moment vector, given with external moments caused by the environment and propulsion moments

$$\mathbf{T} = \mathbf{o}_B + \mathbf{d}_\tau + \boldsymbol{\tau} \tag{13}$$

Moment vector is divided into gyroscopic torque $\mathbf{o}_B$, disturbance moment $\mathbf{d}_\tau = \begin{bmatrix} d_{m\phi} & d_{m\theta} & d_{m\psi} \end{bmatrix}^{\mathrm{T}}$, and propulsion subsystem moment vector $\boldsymbol{\tau} = \begin{bmatrix} \tau_\phi & \tau_\theta & \tau_\psi \end{bmatrix}^{\mathrm{T}}$. The gyroscopic torque vector introduces the gyroscopic effect to the model. When rotating around the desired axis, multirotor starts to rotate around an axis that is perpendicular to the rotor axis and the desired axis of rotation.

$$\mathbf{o}_B = -\sum_{i=1}^{N} J_{TP}\left(\boldsymbol{\omega}^B \times \mathbf{e}_3\right) P_i \omega_i \tag{14}$$

J_{TP} is the total motor inertia moment (around the rotor axis) that depends on the dimensions and geometry of the rotor, P_i is the sign of the ith rotor rotation where clockwise (CW) rotation have positive sign while counterclockwise (CCW) rotation have negative sign and ω_i is the ith rotor angular velocity.

The total rotational dynamics with respect to the body frame is given by the equation

$$\dot{\boldsymbol{\omega}}^B = \mathbf{I}^{-1}\left(-\boldsymbol{\omega}^B \times \left(\mathbf{I}\boldsymbol{\omega}^B\right) + \mathbf{o}_B + \mathbf{d}_\tau + \boldsymbol{\tau}\right) \tag{15}$$

2.3.3. Control vector

Control vector is the input in the multirotor dynamic model from which it follows that it is the only vector that can influence the system dynamics. It consists of propulsion subsystem force and moment vector $\mathbf{u}_B = [\mathbf{f} \quad \boldsymbol{\tau}]^T$. It depends on the propulsion subsystem configuration and squared angular velocities of the rotor, which are the input to the multirotor mathematical model,

$$\mathbf{u}_B = \boldsymbol{\Gamma}_B \boldsymbol{\Omega} \tag{16}$$

where $\boldsymbol{\Gamma}_B$ is control allocation matrix, which describes how the propulsion subsystem maps the rotors angular velocities to the control vector. $\boldsymbol{\Omega}$ is vector of the rotors squared angular velocities, $\boldsymbol{\Omega} = \left[\omega_1{}^2 \; \omega_2{}^2 \ldots \omega_N{}^2\right]^T$.

3. Propulsion subsystem

Multirotor configuration is determined with the propulsion subsystem, which is defined by the geometric arrangement and characteristics of the propulsion units. The assumption is that the propeller aerodynamic forces consist of the thrust force and the drag torque.

3.1. Propulsion aerodynamic forces

During rotation, the propeller motion through the air causes aerodynamic forces that directly affect the multirotor dynamics. An air is accelerated behind the blade through a pressure difference, which is produced between the forward and rear surfaces of the airfoil-shaped blade (**Figure 2**). As a result, thrust force and drag torque are produced depending on the propeller geometric characteristics and the rotor angular velocity.

The relationship between the aerodynamic forces and the rotor angular velocity is derived by the blade element momentum theory. Thrust force of *i*th propulsion unit is given by

$$\mathrm{f}_{R_i} = k_f \omega_i{}^2 \tag{17}$$

where k_f is a thrust force factor, which is determined by propeller geometric characteristics.

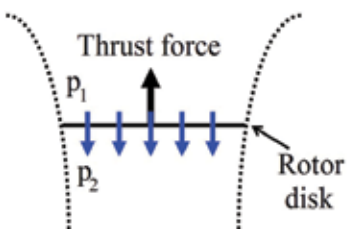

Figure 2. Flow model of a propulsion unit [10].

$$k_f = C_T \rho A r^2 \tag{18}$$

where C_T is thrust force coefficient, ρ is air density, A is the area of propeller (rotor) disk, and r is the propeller radius.

Drag torque of ith propulsion, which must be produced in order to overcome the air resistance and achieve the desired angular velocity is given by

$$\tau_{R_i} = k_\tau {\omega_i}^2 \tag{19}$$

where k_τ is a drag torque factor,

$$k_\tau = C_P \rho A r^3 \tag{20}$$

and C_P is the power coefficient. Thrust force factor k_f and drag torque factor k_τ can be obtained from experimental measurements [16].

3.2. Multirotor configurations

Multirotor configuration consists of an arbitrary number of rotors (N). Configurations mostly consist of even number of propulsion units in order to cancel reactive moment around the vertical axis Z_B. Conventional configurations are characterized by a parallel geometric rotor arrangement and can be divided according to the efficiency of the propulsion arrangement and the size of aircraft.

3.2.1. Conventional propulsion arrangements

The most frequently used configurations have an even number of rotors with a single propulsion arrangement (**Figure 3**). Rotors are placed on the diagonals that are placed in the X or + configuration with respect to the X_B axis marked with the red arrow.

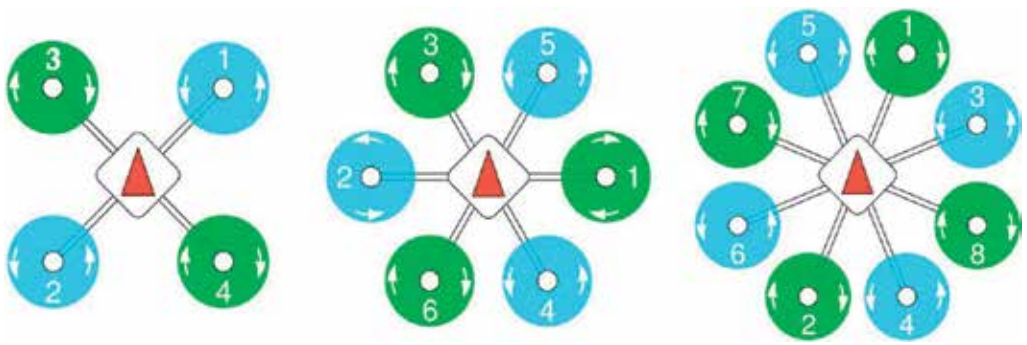

Figure 3. Multirotor configurations with single propulsion arrangement [17].

The selection of the propulsion subsystem depends on the task demands for the payload, flight time duration, or other specific requirements. It is important to note that the increase in the number of rotors increases the price and size of the aircraft.

In addition to a single propulsion arrangement, often configurations have a coaxial arrangement. It is used when greater payload capacity is needed, while at the same time there are limits to the size or geometry of the aircraft. It is characterized by a reduced efficiency of the propulsion unit that manifests itself through shorter flight time or reduced payload capacity compared to configurations with the single arrangement and the same number of rotors [18].

Most commercial control units have a flexible system that allows it to support various multirotor configurations. Architecture ensures that the propulsion geometric arrangement does not require special case handling in the core controllers [19]. Inverted control allocation scheme, often called motor mixer, maps control vector to actuator commands, which control motors or servos. PX4 have built-in airframe references for conventional multirotor configurations as shown in **Figures 3** and **4**.

3.2.2. Nonconventional propulsion arrangements

In addition to the conventional, there are more and more new configurations that are proposed. The configuration with overlapping propulsion geometric arrangement has also parallel rotor arrangement. It is suggested in order to reduce thrust losses respect to the coaxial configurations [20] (**Figure 5**).

The multirotor configurations so far described share features that significantly affect the dynamics and properties of the aircraft. They consist of an even number of symmetrically arranged rotors in one or more parallel planes with $X_B Y_B$ plane. It follows that the rotor thrust vector is parallel with the Z_B axis. We can classify them as flat or parallel multirotor configurations (FMRC).

Due to the specific requirements of some tasks, except flat configurations, the multirotor configurations can have a nonparallel geometric arrangement with respect to the Z_B axis. Rotors can be rotated around two axes, either actively or passively, so it is important to define

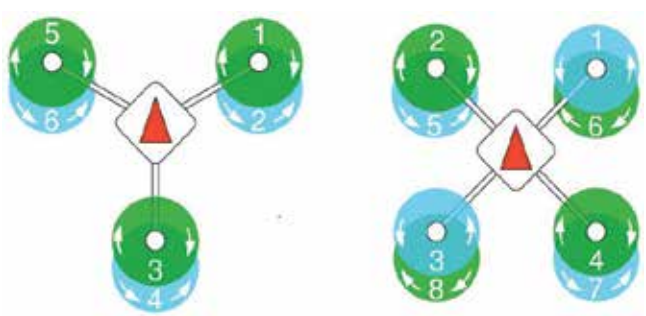

Figure 4. Multirotor configurations with coaxial propulsion arrangement [17].

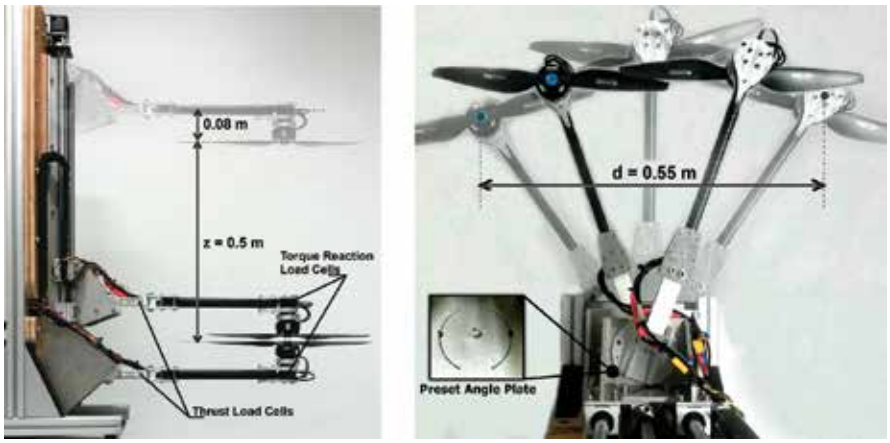

Figure 5. Overlapping propulsion arrangement test rig [20].

a geometric arrangement for different designs. Those configurations can be classified as non-flat multirotor configurations (NFMRC) [21].

3.3. Propulsion geometric arrangement

It is necessary to define the rotor position and orientation relative to the aircraft COG, the origin of body frame. For this purpose, a right-hand coordinate rotor system is defined through which the position and rotor orientation are described. Rotor arm of *i*th rotor connects the origin of body frame and the origin of his frame (**Figure 6**). X_{R_i} is a *i*th rotor arm axis with direction from the aircraft COG. Z_{R_i} has the same orientation and direction as Z_B. We can say that the *i*th rotor frame is actually body frame translated for l_i and rotated for angle χ_i.

3.3.1. Rotor unit position

Rotor position vector ξ_{R_i} is defined with *i*th rotor angle χ_i around the Z_B axis and with the distance l_i from *i*th rotor to origin of body frame. The assumption is that the position of the rotor lies in the $X_B Y_B$ plane, so the third coordinate equals zero,

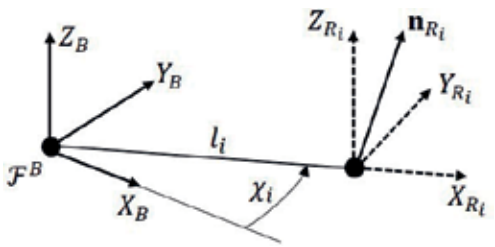

Figure 6. Rotor coordinate systems [21].

$$\xi_{R_i} = \begin{bmatrix} \cos\chi_i \\ \sin\chi_i \\ 0 \end{bmatrix} \cdot l_i \tag{21}$$

3.3.2. Rotor unit orientation

Since the control vector is defined in body frame, the rotor orientation is shown with three consecutive rotations. Orientation vector for *i*th rotor is defined by

$$\mathbf{n}_{R_i} = \mathbf{R}(\chi_i, Z_B)\mathbf{R}\left(\gamma_{y_i}, Y_{R_i}\right)\mathbf{R}\left(\gamma_{x_i}, X_{R_i}\right)\mathbf{e}_3 \tag{22}$$

where $\mathbf{R}(\chi_i, Z_B)$ is rotation matrix around Z_B axis (**Figure 6**), $\mathbf{R}\left(\gamma_{y_i}, Y_{R_i}\right)$ is rotation matrix around Y_{R_i} axis, and $\mathbf{R}\left(\gamma_{x_i}, X_{R_i}\right)$ is rotation matrix around X_{R_i} axis (**Figure 7**).

γ_{x_i} represents rotor tilt angle around *i*th rotor arm axis X_{R_i}, γ_{y_i} represents rotor tilt angle around Y_{R_i} axis, and $\mathbf{e}_3$ is an unit vector. If all tilt angles around rotor frame axes are equal to zero, then we have a parallel or flat multirotor configuration. With proper selection of tilt angles around rotor arm axis, it will be shown that it is possible to achieve desired allocation of force and moment in $\begin{bmatrix} \tau_\phi & \tau_\theta & f_Z \end{bmatrix}^{\mathrm{T}}$ and $\begin{bmatrix} f_X & f_Y & \tau_\psi \end{bmatrix}^{\mathrm{T}}$.

4. Control allocation scheme

The rotors position and orientation determine the allocation of aerodynamic forces to control vector of multirotor UAV, respectively propulsion geometric arrangement maps the thrust forces and drag moments to force and moment vector of propulsion subsystem.

4.1. Thrust force and drag torque mapping

Thrust force mapping of *i*th rotor is determined by the orientation vector of the same rotor. Force vector of *i*th rotor (propulsion) with respect to body frame is given by

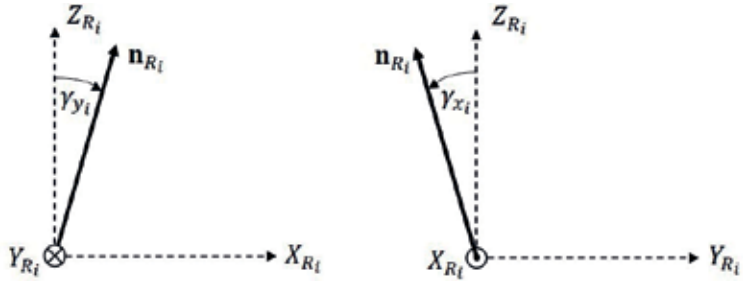

Figure 7. Illustration of tilt angles.

$$\mathbf{f}_i = \left(k_f \mathbf{n}_{R_i}\right)\omega_i{}^2 \tag{23}$$

Thrust force and drag torque mapping of *i*th rotor to a moment vector of *i*th rotor (propulsion) with respect to body frame is given by

$$\boldsymbol{\tau}_i = \left(k_f \boldsymbol{\xi}_{R_i} \times \mathbf{n}_{R_i} + P_i k_\tau \mathbf{n}_{R_i}\right)\omega_i{}^2 \tag{24}$$

P_i is the sign of the *i*th rotor rotation where CW rotation have positive sign while CCW rotation have negative sign.

$$P_i = \text{sign}(\omega_i) \tag{25}$$

The control vector consists of propulsion subsystem force and moment vectors $\mathbf{u}_B = [\,\mathbf{f} \quad \boldsymbol{\tau}\,]^{\mathrm{T}}$. Propulsion subsystem force vector is equal to the sum of the propulsion units' force vectors

$$\mathbf{f} = \sum_{i=1}^{N} \mathbf{f}_i \tag{26}$$

The same applies to propulsion subsystem moment vector, which is equal to the sum of the propulsion units' moment vectors.

$$\boldsymbol{\tau} = \sum_{i=1}^{N} \boldsymbol{\tau}_i \tag{27}$$

4.2. Control allocation matrix

Control allocation scheme is a matrix derived from Eqs. (26) and (27) by using the matrix representation of the vector product $\mathbf{a} \times \mathbf{b} = \mathbf{S}(\mathbf{a})\mathbf{b}$. The matrix rows represent DOF, while the matrix column represents multirotor propulsion units. Control allocation matrix summarizes a mapping of the rotor angular velocities to a control vector

$$\boldsymbol{\Gamma}_{\mathrm{B}} = \begin{bmatrix} k_f \mathbf{n}_{R_1} & \cdots & k_f \mathbf{n}_{R_N} \\ k_f \mathbf{S}\left(\boldsymbol{\xi}_{R_1}\right)\mathbf{n}_{\mathrm{R}_1} + P_1 k_\tau \mathbf{n}_{R_1} & \cdots & k_f \mathbf{S}\left(\boldsymbol{\xi}_{R_N}\right)\mathbf{n}_{R_N} + P_N k_\tau \mathbf{n}_{R_N} \end{bmatrix} \tag{28}$$

Rank of the control allocation matrix determines the controllability of the system, which is an important fact for the control design and motion planning. A control system with full row rank is fully actuated; therefore, it is able to accelerate in an arbitrary direction in space. When the matrix is not full row rank, then the control system is underactuated, and it is not able to accelerate in all directions in space.

5. System controllability

Flat multirotor configurations are characterized by parallel alignment of propulsion units thrust force vectors with Z_B axis. It follows that $\gamma_{x_i} = 0$ and $\gamma_{y_i} = 0$, thus rotors orientation vector is equal to the $\mathbf{e}_3$ unit vector. In that case control allocation matrix has rank equal to four

which means that aircraft provide only four independent control variables. Regardless of the number of actuators, flat configurations shares inherent underactuated condition of control system thus control input cannot accelerate the aircraft in arbitrary directions. In order to achieve the desired position in space, it is necessary to change the orientation of the aircraft, thus flat configurations are strongly coupled systems (**Figure 8**).

Control allocation matrix for flat hexarotor FX6 is given by

$$\mathbf{\Gamma}_{FX6} = \begin{bmatrix} 0 & 0 & 0 & 0 & 0 & 0 \\ 0 & 0 & 0 & 0 & 0 & 0 \\ k_f & k_f & k_f & k_f & k_f & k_f \\ -k_f l & k_f l & \frac{1}{2}k_f l & -\frac{1}{2}k_f l & -\frac{1}{2}k_f l & \frac{1}{2}k_f l \\ 0 & 0 & -\frac{\sqrt{3}}{2}k_f l & \frac{\sqrt{3}}{2}k_f l & -\frac{\sqrt{3}}{2}k_f l & \frac{\sqrt{3}}{2}k_f l \\ k_\tau & -k_\tau & k_\tau & -k_\tau & -k_\tau & k_\tau \end{bmatrix} \tag{29}$$

In order to overcome the underactuation condition, it is required to select propulsion geometric arrangement for which control allocation matrix will have rank equal to six. From Eq. (23),

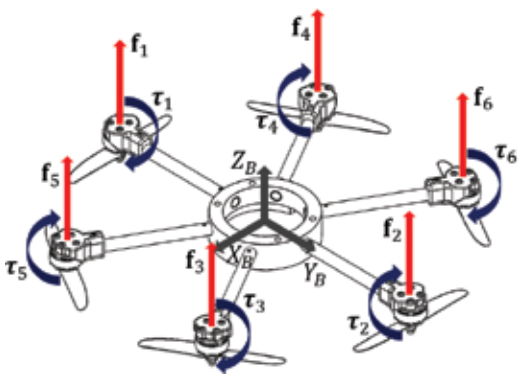

Figure 8. Flat hexarotor configuration—FX6 [22].

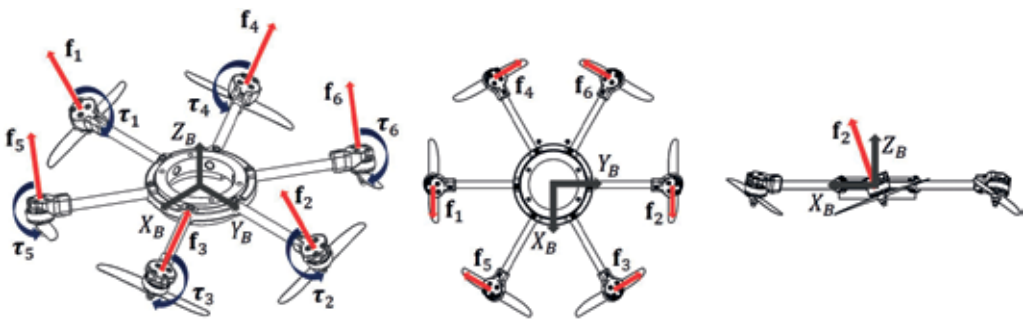

Figure 9. Non-flat hexarotor configuration—NFX6 [22].

it is evident that orientation vector of rotors determines the allocation of thrust force. By tilting rotor around X_{R_i}, it will be shown that it is possible to achieve desired allocation of thrust force so that matrix has rank equal to six. In that case, control system will have six independently controlled DOF, respectively, fully actuated system. A necessary condition is that the multirotor consists of six or more rotors (**Figure 9**).

Control allocation matrix for nonflat hexarotor NFX6 is given by

$$\Gamma_{NFX6} = \begin{bmatrix} k_f s_\gamma & k_f s_\gamma & -\frac{1}{2}k_f s_\gamma & -\frac{1}{2}k_f s_\gamma & -\frac{1}{2}k_f s_\gamma & -\frac{1}{2}k_f s_\gamma \\ 0 & 0 & \frac{\sqrt{3}}{2}k_f s_\gamma & \frac{\sqrt{3}}{2}k_f s_\gamma & -\frac{\sqrt{3}}{2}k_f s_\gamma & -\frac{\sqrt{3}}{2}k_f s_\gamma \\ k_f c_\gamma & k_f c_\gamma & k_f c_\gamma & k_f c_\gamma & k_f c_\gamma & k_f c_\gamma \\ -k_f l c_\gamma + k_\tau s_\gamma & k_f l c_\gamma - k_\tau s_\gamma & \frac{1}{2}k_f l c_\gamma - \frac{1}{2}k_\tau s_\gamma & -\frac{1}{2}k_f l c_\gamma + \frac{1}{2}k_\tau s_\gamma & -\frac{1}{2}k_f l c_\gamma + \frac{1}{2}k_\tau s_\gamma & \frac{1}{2}k_f l c_\gamma - \frac{1}{2}k_\tau s_\gamma \\ 0 & 0 & -\frac{\sqrt{3}}{2}k_f l c_\gamma + \frac{\sqrt{3}}{2}k_\tau s_\gamma & \frac{\sqrt{3}}{2}k_f l c_\gamma - \frac{\sqrt{3}}{2}k_\tau s_\gamma & -\frac{\sqrt{3}}{2}k_f l c_\gamma + \frac{\sqrt{3}}{2}k_\tau s_\gamma & \frac{\sqrt{3}}{2}k_f l c_\gamma - \frac{\sqrt{3}}{2}k_\tau s_\gamma \\ k_f l s_\gamma + k_\tau c_\gamma & -k_f l s_\gamma - k_\tau c_\gamma & k_f l s_\gamma + k_\tau c_\gamma & -k_f l s_\gamma - k_\tau c_\gamma & -k_f l s_\gamma - k_\tau c_\gamma & k_f l s_\gamma + k_\tau c_\gamma \end{bmatrix} \tag{30}$$

6. Conclusions

This chapter describes a nonlinear mathematical model for the multirotor type of UAV. Mathematical model consists of rigid body dynamics and control allocation scheme providing a certain modularity for control design and implementation. Control allocation scheme describes a mapping of the rotor angular velocities to a control vector, which is determined by propulsion geometric arrangement and physical parameters. Matrix row rank is important information about the controllability of a system. Conventional flat multirotor configurations have only four independent control variables, it follows that they have in common the underactuation condition of system. Since the underactuated system cannot be controlled to follow arbitrary trajectories and some tasks require complex movements, it is important to design multirotor configurations which overcome underactuation limitation. The described mathematical model can be used for open loop simulations which are important for dynamics and power consumption analysis. Furthermore, the inverted scheme is suitable for implementation in various flight controllers.

Author details

Denis Kotarski[1]* and Josip Kasać[2]

*Address all correspondence to: denis.kotarski@vuka.hr

1 Karlovac University of Applied Sciences, Karlovac, Croatia

2 Faculty of Mechanical Engineering and Naval Architecture, University of Zagreb, Zagreb, Croatia

References

[1] Konrad R, Serrano D, Strupler P. Unmanned aerial systems. In: Search and Rescue Robotics —From Theory to Practice. Rijeka: InTech; 2017. pp. 37-52. DOI: 10.5772/intechopen.68449

[2] Mizutani S, Okada Y, Salaan CJ, Ishii T, Ohno K, Tadokoro S. Proposal and experimental validation of a design strategy. In: 2015 IEEE/RSJ International Conference on Intelligent Robots and Systems (IROS). Hamburg, Germany: 28 Sept-2 Oct; New York: IEEE; 2015. pp. 1271-1278. DOI: 10.1109/IROS.2015.7353532

[3] Bresciani T. Modelling, identification and control of a quadrotor helicopter [thesis]. Lund: Lund University; 2008. 184 p. Available from: http://www.control.lth.se/publications/

[4] Mulgaonkar Y, Whitzer M, Morgan B, Kroninger CM, Harrington AM, Kumar V. Power and weight considerations in small, agile, quadrotors. In: George T, Islam MS, Dutta AK, editors. Proc. SPIE 9083, Micro- and Nanotechnology Sensors, Systems, and Applications VI. 2014. DOI:10.1117/12.2051112

[5] Raza SA, Gueaieb W. Intelligent flight control of an autonomous Quadrotor. In: Casolo F, editor. Motion Control. Rijeka: InTech; 2010. pp. 245-264

[6] Naidoo Y, Stopforth R, Bright G. Quad-rotor unmanned aerial vehicle helicopter modelling & control. International Journal of Advanced Robotic Systems. 2011;**8**(4):139-149

[7] Nicol C, Macnab CJB, Ramirez-Serrano A. Robust adaptive control of a quadrotor helicopter. Mechatronics. 2011;**21**:927-938. DOI: 10.1016/j.mechatronics.2011.02.007

[8] Kasać J, Stevanović S, Žilić T, Stepanić J. Robust output tracking control of a quadrotor in the presence of external disturbances. Transactions of FAMENA. 2013;**37**(4):29-42

[9] Kim GB, Nguyen TK, Budiyono A, Park JK, Yoon KJ, Shin J. Design and development of a class of rotorcraft-based UAV. International Journal of Advanced Robotic Systems. 2013;**10**(2):1-9. DOI: 10.5772/54885

[10] Otsuka H, Nagatani K. Thrust loss saving design of overlapping rotor arrangement on small multirotor unmanned aerial vehicles In: 2016 IEEE International Conference on Robotics and Automation (ICRA). Stockholm, Sweden: 16-21 May; New York: IEEE. p. 3242-3248. DOI: 10.1109/ICRA.2016.7487494

[11] Driessens S, Pounds P. The triangular Quadrotor: A more efficient quadrotor configuration. IEEE Transactions on Robotics. 2015;**31**(6):1517-1526. DOI: 10.1109/TRO.2015.2479877

[12] Segui-Gasco P, Al-Rihani Y, Shin H, Savvaris A. A Novel Actuation Concept for a Multi Rotor UAV. In: 2013 International Conference on Unmanned Aircraft Systems (ICUAS); 28-31 May; Atlanta, USA. 2013. pp. 373-382. DOI: 10.1109/ICUAS.2013.6564711

[13] Badr S, Mehrez O, Kabeel AE. A novel modification for a quadrotor design. In: 2016 International Conference on Unmanned Aircraft Systems (ICUAS); 7-10 June; Arlington, USA. 2016. pp. 702-710. DOI: 10.1109/ICUAS.2016.7502536

[14] Ryll M, Bulthoff HH, Giordano PRA. Novel overactuated quadrotor unmanned aerial vehicle: Modeling, control, and experimental validation. IEEE Transactions on Control Systems Technology. 2014;**23**(2):540-556. DOI: 10.1109/TCST.2014.2330999

[15] Jiang G, Voyles R. A nonparallel hexrotor UAV with faster response to disturbances for. In: 2014 IEEE International Symposium on Safety, Security, and Rescue; 27-30 Oct; Toyako-cho, Abuta, Japan. 2014. pp. 1-5. DOI: 10.1109/SSRR.2014.7017669

[16] Kotarski D, Krznar M, Piljek P, Šimunić N. Experimental identification and characterization of multirotor UAV propulsion. In: 2nd International Conference on Measurement Instrumentation and Electronics; 9-11 June; Prague, Czech Republic. Journal of Physics: Conference Series; 2017

[17] Dronecode. Airframes Reference [Internet]. Available from: https://dev.px4.io/en/airframes/airframe_reference.html [Accessed: 22.11.2017]

[18] Kotarski D, Piljek M, Tevčić M, Vyroubal V. Mathematical modelling and dynamics analysis of flat multirotor configurations. WSEAS Transactions on Systems. 2017;**16**:47-52

[19] Dronecode. Mixing and Actuators [Internet]. Available from: https://dev.px4.io/en/concept/mixing.html [Accessed: 23.11.2017]

[20] Brazinskas M, Prior SP, Scanlan JP. An empirical study of overlapping rotor interference for a small unmanned aircraft propulsion system. Aerospace. 2016;**3**(4):1-20. DOI: 10.3390/aerospace3040032

[21] Kotarski D, Piljek P, Brezak H, Kasać J. Chattering free tracking control of a fully actuated multirotor with passively tilted rotors. Transactions of FAMENA. 2018;**42**(1)

[22] Kotarski D, Piljek P, Brezak H, Kasać J. Design of a fully actuated passively tilted multirotor UAV with decoupling control system. In: 2017 8th International Conference on Mechanical and Aerospace Engineering (ICMAE); 22–25 July; Prague, Czech Republic. 2017. pp. 385-390. DOI: 10.1109/ICMAE.2017.8038677

Chapter 5

Uncertainty of Object-Based Image Analysis for Drone Survey Images

Lei Ma, Gaofei Yin, Zhenjin Zhou, Heng Lu and Manchun Li

Additional information is available at the end of the chapter

http://dx.doi.org/10.5772/intechopen.72332

Abstract

With the recent developments in the acquisition of images using drone systems, object-based image analysis (OBIA) is widely applied to such high-resolution images. Therefore, it is expected that the application of drone survey images would benefit from studying the uncertainty of OBIA. The most important source of uncertainty is image segmentation, which could significantly affect the accuracy at each stage of OBIA. Therefore, the trans-scale sensitivity of several spatial autocorrelation measures optimizing the segmentation was investigated, including the intrasegment variance of the regions, Moran's I autocorrelation index, and Geary's C autocorrelation index. Subsequently, a top-down decomposition scheme was presented to optimize the segmented objects derived from multiresolution segmentation (MRS), and its potential was examined using a drone survey image. The experimental results demonstrate that the proposed strategy is able to effectively improve the segmentation of drone survey images of urban areas or highly consistent areas.

Keywords: OBIA, high-resolution image, segmentation, uncertainty, Moran's I, Geary's C

1. Introduction

Low-altitude drone imaging is widely used in mapping, land cover/land use monitoring, and resource and environment monitoring, and various low-altitude drone data processing and analysis models have been established [1–4]. As drones are flexible, have customizable temporal resolution, and high spatial resolution, they have attracted much attention from researchers and manufacturers. Drone-based remote sensing has already been applied to the management and monitoring of forest resources [5], vegetation and river monitoring [6], monitoring of archeological sites [7], management of natural disasters and seismic monitoring [8], precision

farming [9], and other aspects. Drone-based remote sensing has been widely applied mainly owing to recent breakthroughs in drone-based remote sensing data acquisition technology, as well as innovative and technological improvements in the remote sensing field [10–13]. The abovementioned descriptions of information extraction from drone-based remote sensing fully utilized the advantages of high spatial resolution in imaging and employed object-based image analysis (OBIA) technology. Therefore, studying the uncertainty of OBIA in drone-based image processing has important significance for the application of drone-based high-resolution imaging.

Segmentation is a prerequisite for OBIA, and the scale of segmentation is an important factor affecting OBIA and affects nearly every stage of OBIA. Multiresolution segmentation (MRS) has been shown to be one of the relatively successful segmentation algorithms in OBIA [14, 15]. This algorithm is very complex and has high requirements on the user; the scale, shape, compactness, and other variables are its main parameters, which are all user-customizable [14]. However, many studies have shown that the scale is the most important parameter, as it controls the dimensions of the subject after segmentation and can directly affect the subsequent classification [16–20]. Therefore, scale problems have become a current prominent problem in OBIA, particularly in OBIA research on MRS. Arbiol et al. [21] also pointed out that semantically significant regions are found at different scales, making the acquisition of appropriate segmentation scales and obtaining optimized segmentation results relatively important. However, many specific terrain extraction studies were dependent on repeated experiments, and scale parameters were determined according to experience [22]. Evidently, this is an irreplaceable method [23], and therefore, many researchers have proposed methods to determine the optimal scale parameter [20, 23–27].

Therefore, this chapter focuses on discussing the uncertainty of multiscale segmentation and testing the sensitivity of the evaluation indicators in different segmentation results. Furthermore, the quality of the segmentation results from different scales will be verified in order to propose a strategy to improve the quality of multiscale segmentation. Firstly, the internal consistency of the segmentation object (area-weighted average variance) and the spatial autocorrelation indicators of the object (Moran's I and Geary's C) under different segmentation results were evaluated and measured. Subsequently, based on the consistency and autocorrelation indicators, a top-down object decomposition protocol was proposed so that the segmentation objects can coincide with objects in different terrains. Lastly, an area-based method was used to calculate the precision and recall indicators to evaluate the quality of the multiscale segmentation results. In addition, the optimized segmentation results in the proposed method were verified. This contributed to the high-efficiency processing of data generated by drone-based remote sensing.

2. Study site and data

In August 2011, we used a fixed-wing drone equipped with a Canon EOS 5D Mark II digital camera, with end and side overlaps of 80 and 60%, respectively, at an average flight altitude of 750 m to collect raw image data from a total of 400 km^2 of built-up areas and suburbs in Deyang city. The size of a single image was 5616 × 3744 pixels, and the spatial resolution was

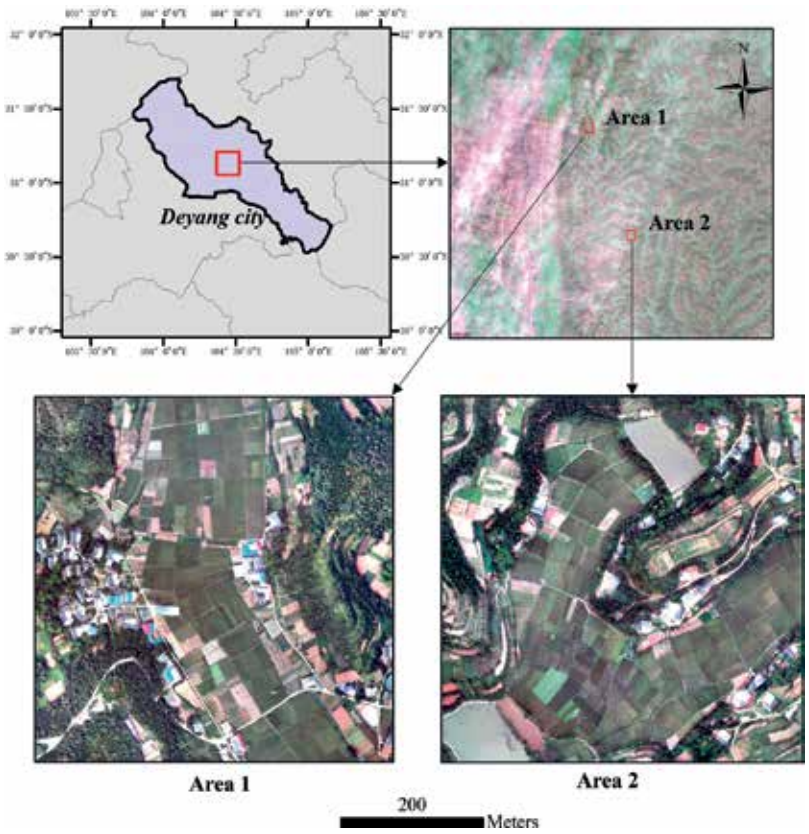

Figure 1. RGB UAV images after orthorectification.

0.2 m. The actual coverage area of each image was 1123 × 748 m. The focal length of the camera was 24.5988 m, and the sensor pixel size was 0.064 mm. After the field images were acquired, the field control points were collected, with each flight belt interval containing one control point. In a flight belt, there were generally 3–5 photographs per control point. Subsequently, digital photogrammetry was used to complete a 0.2-m resolution digital orthophoto map (DOM), which generated 500 × 500 m standard maps.

Two standard drone DOMs (500 × 500 m) were selected for the study, including area 1 and area 2 (**Figure 1**). The terrain ratio of the two experimental images was different: area 1: covered cultivated land (38%), forests (43%), buildings (6%), bare land (5%), and roads (2%), whereas area 2: covered cultivated land (45%), forests (37%), buildings (4%), water bodies (5%), and roads (1%).

3. Multiscale segmentation

Multiscale segmentation is one of the most popular remote sensing segmentation algorithms, and practical applications have been widely used [22, 28, 29]. Multiscale segmentation is a

technique based on region merging, and it is a process of bottom-up region merging from the pixel layer, in which image objects are merged into the large image object layer by layer to produce segmentation results at different segmentation scales. The average spectral heterogeneity of all image objects in the image layer is significantly increased after fusion. In order to achieve this aim, each single merging process must minimize the heterogeneity of two adjacent objects involved in the merging process [30], such that the heterogeneity of the object after merging relative to the increase in the area-weighted heterogeneity of the original two images h_{diff} is minimized. However, the increase in heterogeneity h_{diff} should be smaller than a threshold value (controlled by scale parameters). If and only if h_{diff} is smaller than the threshold value, then the merging is carried out [31]. Using the commercial software eCognition, which was mainly used in this work to implement multiscale segmentation, the heterogeneity was calculated through spectral and shape characteristics. The employed formula is $f = w_{color} \cdot \Delta h_{color} + w_{shape} \cdot \Delta h_{shape}$, where $w_{color} \in [0,1]$ and $w_{shape} \in [0,1]$ are weight parameters that satisfy $w_{color} + w_{shape} = 1$. In detail, Δh_{shape} represents the measurement of the shape modification of the segmentation object, which is measured by smoothness and compactness using the formula $\Delta h_{shape} = w_{compt} \cdot \Delta h_{compt} + w_{smooth} \cdot \Delta h_{smooth}$, where $w_{compt} \in [0,1]$ and $w_{smooth} \in [0,1]$ are weight parameters, and $w_{compt} + w_{smooth} = 1$. For detailed calculations of Δh_{color} and Δh_{shape}, please refer to [31].

In summary, the segmentation parameters mainly include scale parameters and two groups of parameters (w_{color}/w_{shape} and w_{compt}/w_{smooth}). Generally, the segmentation scale parameters represent the largest uncertainty factor causing changes in segmentation results. Therefore, reference data were used to evaluate the quality of the segmentation results under different segmentation scales and test the sensitivity of the evaluation indicator of two segmentation results (including internal consistency and the spatial autocorrelation indicator). In addition, we proposed a top-down object segmentation strategy based on the multiscale segmentation results. In multiscale segmentation, at every segmentation scale, the parameters w_{color}/w_{shape} and w_{compt}/w_{smooth} were fixed as 0.9/0.1 and 0.5/0.5, respectively. Of these parameters, the spectral weight parameter of 0.9 resulted in spectral information playing the most important role in the segmentation process. In order for the segmentation to show no bias between smoothness and compactness, their weight parameters were set to 0.5. In addition, the band weights involved in the segmentation were all set to 1.

4. Evaluation indicators of segmentation results

4.1. Measurement of internal consistency

Multiscale segmentation is essentially a technique based on region merging/growing [30]; this type of method is usually sensitive to the threshold values of the merging conditions, and artificially determined threshold values generally have errors. Therefore, we first measured the sensitivity of different indicators toward the segmentation results and focused on two types of indicators (object internal consistency and object heterogeneity). The best segmentation result should have the maximum consistency and minimum heterogeneity (low spatial autocorrelation) [32]. Currently, in order to evaluate the consistency of objects in the segmentation results,

many studies on scale optimization have focused on an area-weighted average variance or local variance, given by the following formula [32]:

$$v = \frac{\sum_{i=1}^{n} a_i \cdot v_i}{\sum_{i=1}^{n} a_i} \tag{1}$$

Here, vi represents the variance of the ith segmentation object and ai represents the area of the ith segmentation object. The result v represents the internal area-weighted average variance of all the segmentation objects. The larger the value of v, the stronger the consistency of various objects or the smaller the overall difference, and the smaller the value, the larger the overall difference among the segmentation objects [25].

4.2. Object spatial autocorrelation

Generally, the best segmentation results result in the largest difference among objects, such that objects can be better differentiated and heterogeneity indicators reflect this difference. In order to evaluate the heterogeneity between segmentation objects, we tested two heterogeneity indicators, including the Moran's I and reverse Geary's C indices. Moran's I is widely used in current research [23, 32] and tends to indicate global heterogeneity. Geary's C index is less commonly used and tends to represent local heterogeneity.

(1) Moran's I index

$$I = \frac{n\sum_{i=1}^{n}\sum_{j=1}^{n} w_{ij}\left(y_i - \bar{y}\right)\left(y_j - \bar{y}\right)}{\left(\sum_{i=1}^{n}\left(y_i - \bar{y}\right)^2\right)\left(\sum_{i\neq j}\sum w_{ij}\right)} \tag{2}$$

where n represents the number of segmentation objects, yi represents the average grayscale value of all the pixels in the ith segmentation object Ri, and $\bar{y}$ represents the average grayscale value of all the pixels in the entire image. W represents the spatial adjacency matrix between the segmentation objects, and each weight wij represents the adjacency relationship between the segmentation objects Ri and Rj in the segmentation image layer. If Ri and Rj are adjacent, then wij = 1; otherwise, wij = 0. It is worth noting that the indices in this formula are all used for single bands and the value range of I is [−1, 1]. The smaller the value of I, the lower the autocorrelation between the segmentation objects, showing that there are statistical differences between objects. Theoretically, an extremely low value of I exists and represents the best segmentation result [32].

(2) Reverse Geary's C index

The range of Geary's C index values is [0, 2], where a value of 1 indicates no spatial autocorrelation, values less than 1 indicate that there is spatial autocorrelation, and the greater the value, the stronger the correlation. Correspondingly, values greater than 1 indicate negative spatial correlation [33]. Therefore, it is not difficult to see that the Geary's C and Moran's I indices are essentially negatively correlated. In order for Geary's C to be consistent with

Moran's I, Geary's C was expanded here into the reverse Geary's C (C), such that C is equal to one minus Geary's C, given as follows:

$$C = 1 - \frac{(N-1)\sum_i \sum_j w_{ij}(X_i - X_j)^2}{2W\sum_i (X_i - \overline{X})} \quad (3)$$

where N represents the total number of segmentation objects that are in the calculation through i or j indices, X represents the characteristic variable in the calculation, $\overline{X}$ represents the mean value of the characteristic variables of all segmentation objects, and w_{ij} represents a weight matrix with values of 1 or 0 (1 means that the ith object is adjacent to the jth object, and 0 indicates that they are not adjacent). W indicates the total sum of the weight matrix w_{ij}. The range of values for the reverse Geary's C indicator C is [−1, 1], and this is noted to be consistent with the value range of Moran's I.

4.3. Combined analysis of indicators

As consistency and spatial autocorrelation use different angles to evaluate the segmentation results, this section further tests the combined results of both indicators. In order for the consistency and autocorrelation measurements to be comparable, first, $X_{norm} = (X - X_{min})/(X_{max} - X_{min})$ was used to normalize the area-weighted variance (v) in the consistency measurements and the two spatial autocorrelation indicators. Subsequently, the sum of the normalized weighted variance and spatial autocorrelation (using the reverse Geary's C index as an example, $LS = v_{norm} + C_{norm}$) was used to calculate the optimized segmentation scales. Evidently, the individual optimized segmentation results should be scales with lower LS values. This is because at this time, when the combined value of the weighted variance and the spatial autocorrelation value is minimal, both are at an equilibrium and both indicators tend to be optimal [23]. However, the scales obtained this way are individually optimized parameters in the segmentation object when the internal consistency and inter-object heterogeneity have reached the maximal equilibrium. In addition, the three abovementioned indicators were all measurements against a single band or characteristic variable, that is, only one band or characteristic at a time can be calculated. Generally, the segmentation process includes many bands, such as the three RGB bands in the drone data from the previously mentioned experiment. Therefore, in order to consider many bands simultaneously, the mean values of each band were simply obtained when calculating the combined value.

5. Top-down object decomposition

The optimal segmentation scales of differently sized objects are different [34], and the scales obtained through the single acquisition of indicators above are only individually optimized scales; therefore, the segmentation objects have further potential for optimization. Here, the above three parameters were used as a reference to substitute the global indicators, and considering the local spatial autocorrelation indicators, a top-down object decomposition strategy was proposed to optimize the segmentation objects in different terrain types. The

specific steps were as follows: (1) firstly, the segmentation of different scales was achieved, such as 10–300, with a step length of 10. Following that, from a scale of 300, an object set O at the scale 290 in various objects at the scale 300 was searched. If the absolute value of the C indicator of O_i was greater than the specified threshold, then the objects in the combined set O are one object and the updated scale 290 segmentation object image layer is stored until the complete transversal of all objects at the scale 300 layer. (2) Subsequently, step 1 was repeated from the updated scale 290 segmentation image layer, and sequential transversal of all image layers was carried out until the scale 10 image layer. This method is the reverse of the eCognition multiscale segmentation strategy (the eCognition software uses the homogeneity of adjacent objects to measure the bottom-up combined objects and achieve multiscale segmentation) and can play a complementary role.

6. Validation method for segmentation boundaries

Finally, the validation of segmentation boundaries was implemented. On the one hand, the multiscale segmentation results were validated as a reference for subsequent studies; on the other hand, the segmentation results using the method proposed here were validated. An artificial interpreted reference image layer was used and combined with the precision and recall indicators that were calculated from area-based methods. These two indicators have already been widely used in the evaluation of segmentation boundaries [35, 36]. The basic principle is that by assuming a segmentation result S of the raw image and a corresponding actual ground reference image layer R, the precision indicator shows the pixels or area ratio in the ground reference object when the majority of pixels in the object in the segmentation result S overlap. This indicator is relatively sensitive to over-segmentation. The recall indicator shows the ratio of the majority of pixels or area overlapping in the segmentation object in the actual ground object and is sensitive to under-segmentation [36]. In order to clearly describe the calculation process of the precision and recall indicators based on area, the description in [37] was referenced to calculate the precision indicator. The segmentation image layer was matched to the reference image layer, and the object Si in the segmentation image layer was transversed to calculate the overlap area between every R and the largest reference object Rimax in the overlap area of the segmentation image layer. Subsequently, the sum of the overlap areas was divided by the total area of the segmentation image layer, to calculate the precision indicator as follows:

$$Precison = \sum_{i=1}^{n} |S_i \cap R_{i\max}| \Big/ \sum_{i=1}^{n} |S_i| \tag{4}$$

where $|X|$ represents the area of unit X. Similarly, to calculate the recall indicator, the object Ri in the reference image layer was transversed and the overlap area between every Ri and the largest reference object Simax in the overlap area of the segmentation image layer was calculated. Subsequently, the sum of the overlap areas was divided by the total area of the segmentation image layer:

$$Recall = \sum_{i=1}^{n} |R_i \cap S_{i\max}| \Big/ \sum_{i=1}^{m} |R_i| \tag{5}$$

From the principle and calculation process of the two accuracy indicators, it is not difficult to see that similar to the consistency/heterogeneity indicators, both of these indicators are negatively correlated to each other to some degree and it is difficult for both precision indicators to be large at the same time. Generally, only the mean value of the two indicators can be obtained; therefore, both indicators are simply summed together to measure the overall effects of the segmentation:

$$Sum = Precision + Recall \tag{6}$$

7. Experiment discussion

7.1. Changes in each indicator with scale

(1) Area-weighted variance

Generally, optimized scales can be measured by considering the relationship between variance and scale. **Figures 2** and **3** demonstrate the variation of the average variance of the three bands with segmentation scale in experimental areas 1 and 2, respectively, and both regions show consistent trends: as the scale increases, the number of segmentation objects decreases and the average variance of the objects gradually increases. This is easily understood, as when the segmentation scale increases, the segmentation object becomes larger and each segmentation object tends to include a greater area of image brightness values [25]. Therefore, on a rough scale, the average variance of the segmentation objects will tend to increase. Kim et al. [25]

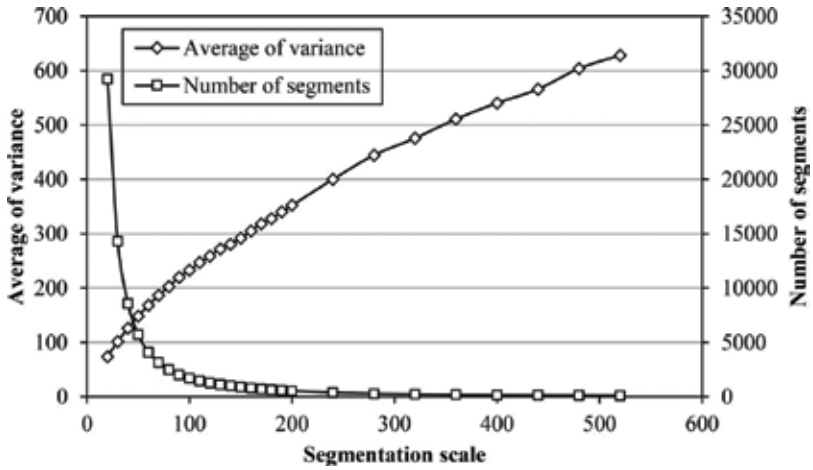

Figure 2. Average of variance for three bands in area 1.

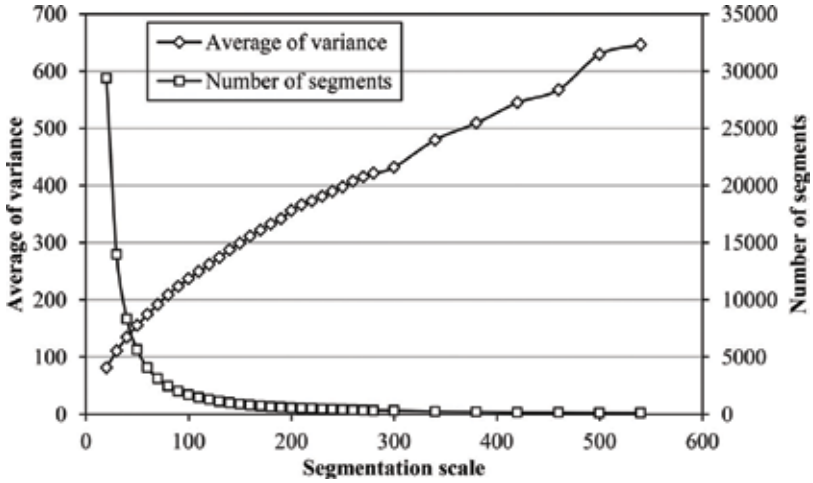

Figure 3. Average of variance for three bands in area 2.

found that with increased scale, and even until under-segmentation, the hybrid object includes more pixels that did not originally belong to the actual image, thereby decreasing the variance of these hybrid images. Therefore, it is generally believed that an optimal segmentation scale exists before the variance tends be gentle. However, the experiment results showed that apart from insignificant inflection points near scale 60, it is difficult to find regions with gentle changes in **Figures 2** and **3**. Conversely, when the variance increases with scale, the magnitude of the increase in consistency is almost maintained. It is worth noting that [38] used a similar principle to develop an estimation of scale parameter (ESP) scale optimization tool, where they integrated the rate of change of the variance curves and the variance curves to identify the optimal segmentation scale. This was carried out under conditions when the magnitude of change in variance with scale was not very significant and was not the best choice.

(2) Moran's I

Figures 4 and **5** shows that Moran's I index continuously decreased when the scale increased from fine to coarse. A fine scale generally tends toward over-segmentation, that is, the segmentation objects that are adjacent to each other are more similar, resulting in a larger Moran's I index (i.e., stronger autocorrelation between objects). Conversely, an increase in scale results in under-segmentation; the segmentation objects become larger, the differences between adjacent segmentation objects become significant, the spectral consistency decreases, and thus Moran's I index decreases. Therefore, considering the variation curve of the autocorrelation indices with the segmentation scale, [25] believed that the minimum autocorrelation should correspond to the optimal segmentation scale. However, the results showed that (**Figures 4** and **5**) the autocorrelation in both experimental areas continuously decreases with increasing scale and Moran's I index alone cannot determine the optimal scale.

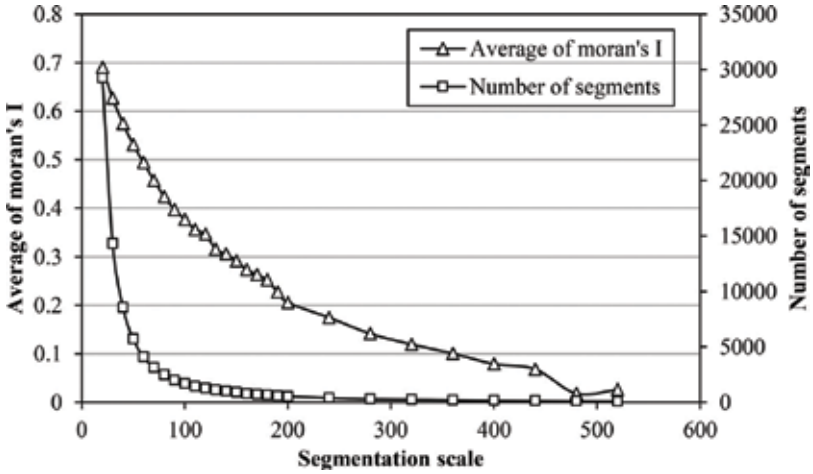

Figure 4. Average of Moran's I for three bands in area 1.

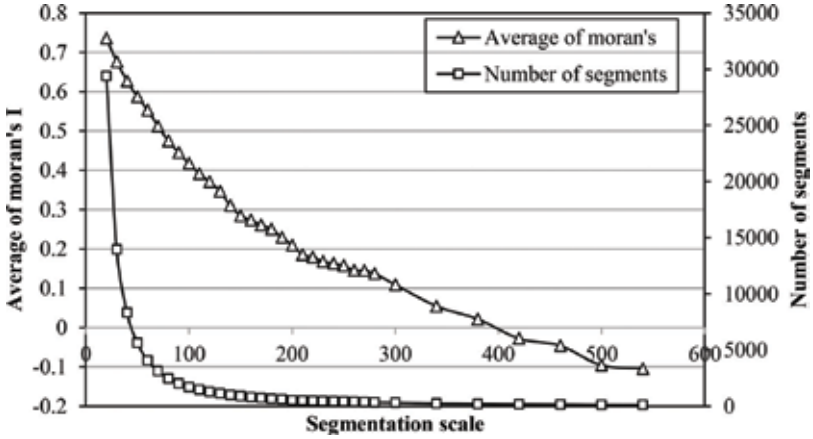

Figure 5. Average of Moran's I for three bands in area 2.

(3) Reverse Geary's C index

Considering that changes in the autocorrelation index Moran's I are not very significant, we tried another autocorrelation index that is more sensitive to local heterogeneity, Geary's C. **Figures 6** and **7** show the changes in Geary's C index with changes in the segmentation scale in the two experimental areas, and it was found that Geary's C decreased with increasing scale. In reality, changes around the optimal segmentation scale are more sensitive: In experimental areas 1 and 2, the regions near scales 120 and 150, respectively, started to become stable, and the magnitude of the scale changes was not as large as that on the fine scale. According to the validation results of the optimized segmentation boundaries (**Figures 12** and **13**), the reverse Geary's C index can better represent the optimized scale compared with variance and Moran's I index.

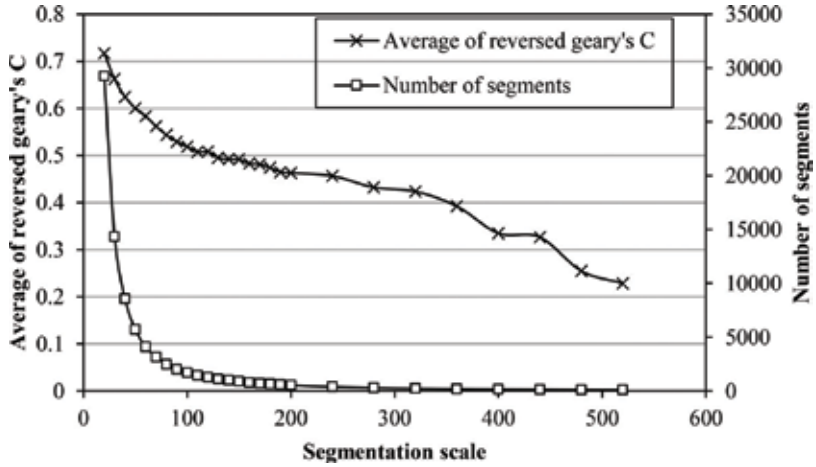

Figure 6. Average of reverse Geary's C for three bands in area 1.

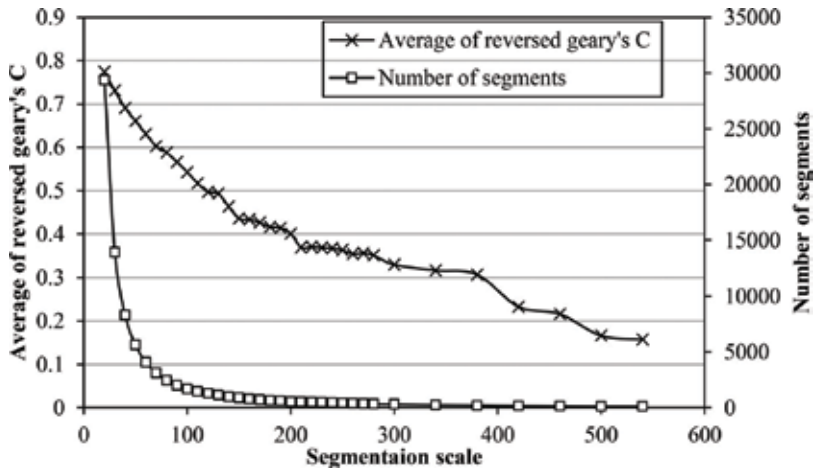

Figure 7. Average of reverse Geary's C for three bands in area 2.

(4) Normalized sums

According to the consistency and autocorrelation tests in the preceding section, it was found that as the scale increases, the variance indicators that represent the consistency of the segmentation object continuously increase, whereas the autocorrelation indicator that represents heterogeneity continuously decreases and it is difficult to discover regions where the changes start to stabilize. Therefore, it is theoretically possible to use the two indicators individually to identify the optimal segmentation scale; Dr guţ et al. [38] and Kim et al. [25] obtained the optimal segmentation scale using one indicator in their studies. The maximum or minimum value can be identified through single indicators, but in fact, the maximum or minimum values do not have a corresponding optimal segmentation scale. This is because when variance still

increases at scale 500 (**Figures 2** and **3**), Moran's I and reverse Geary's C indices still decrease at scale 500 (**Figures 4**–**7**). In our experimental area, scale 500 or even larger scales are evidently not optimal, and this is shown in the subsequent validation results of the optimized segmentation boundaries. Therefore, single indicators are not suitable for the identification of the overall optimal scale. According to the description in the preceding sections, the sum of two indicators for the identification of optimized scales may be appropriate. The test results for experimental areas 1 and 2 are shown in **Figures 8**–**11**. **Figures 8** and **9** represent the sum of normalized variance and normalized Moran's I index, whereas **Figures 10** and **11** represent the sum of normalized variance and normalized reverse Geary's C index. From the validation results of the combined optimized segmentation boundaries (**Figures 12** and **13**), it is easy to see that the curve of the sum of the normalized variance and normalized Moran's I index with

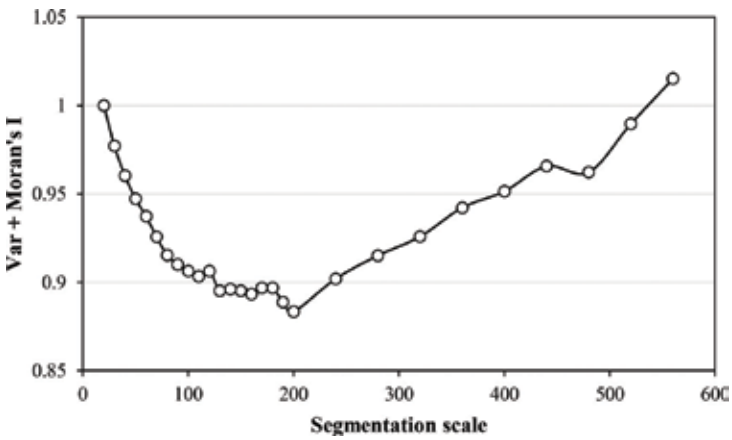

Figure 8. Sum of normalized variance and Moran's I for three bands in area 1.

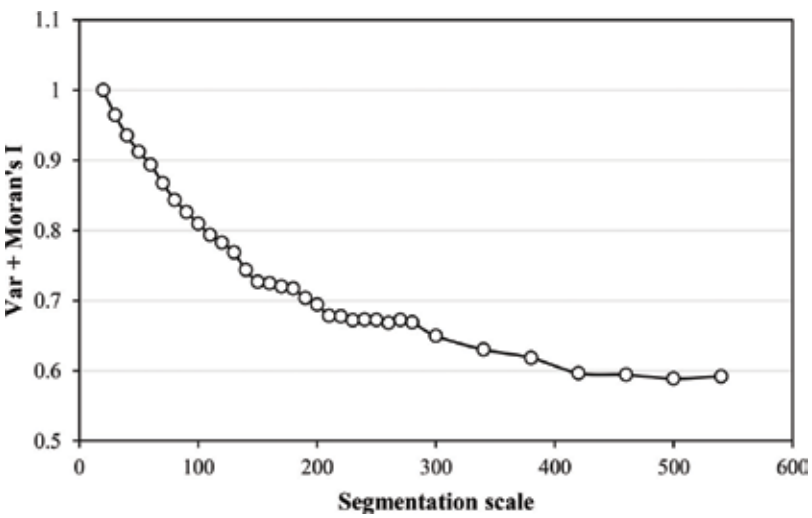

Figure 9. Sum of normalized variance and Moran's I for three bands in area 2.

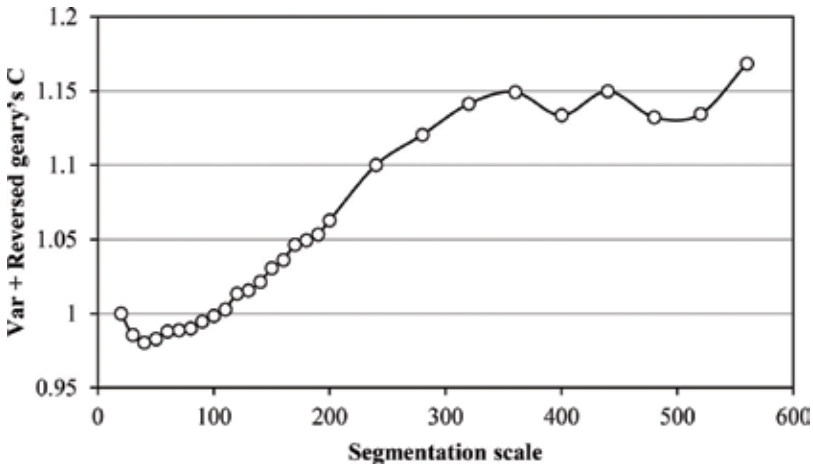

Figure 10. Sum of normalized variance and reverse Geary's C for three bands in area 1.

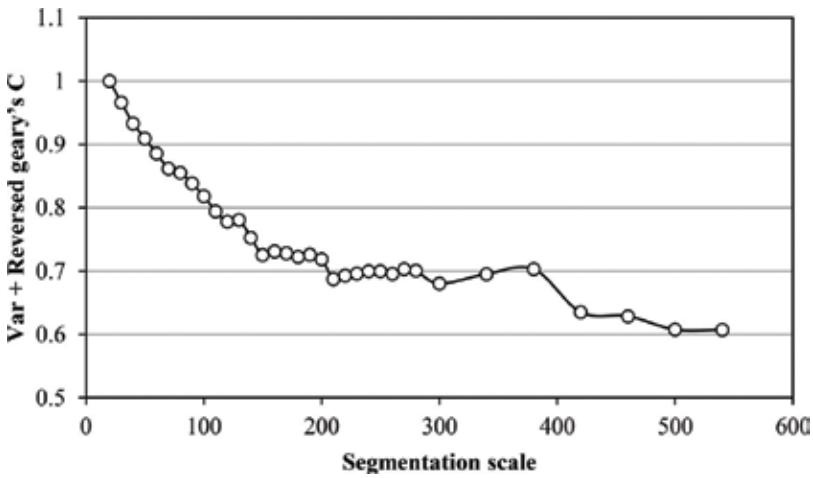

Figure 11. Sum of normalized variance and reverse Geary's C for three bands in area 2.

scale changes can better highlight the optimal segmentation scale, even at the extremely low value obtained at scale 200 in **Figure 8**. This result is consistent with the thinking of [23] who suggested that the lowest corresponding scale of the sum of consistency and heterogeneity indicators is the optimal scale. However, for different experimental areas, the lowest value usually cannot be obtained at the optimal scale, such as in **Figure 9**, which show that the sum of the normalized variance and normalized Moran's I index in experimental area 2 did not achieve extremely low values at suitable scales. It is worth noting that starting from scales 150–200, with increasing scale, the sum of the normalized variance and normalized Moran's I index in experimental area 2 starts to show significant moderation trends and this region corresponds well to the optimal segmentation scale in experimental area 2. Therefore, optimal segmentation scales are assumed to exist between under-segmentation and over-segmentation.

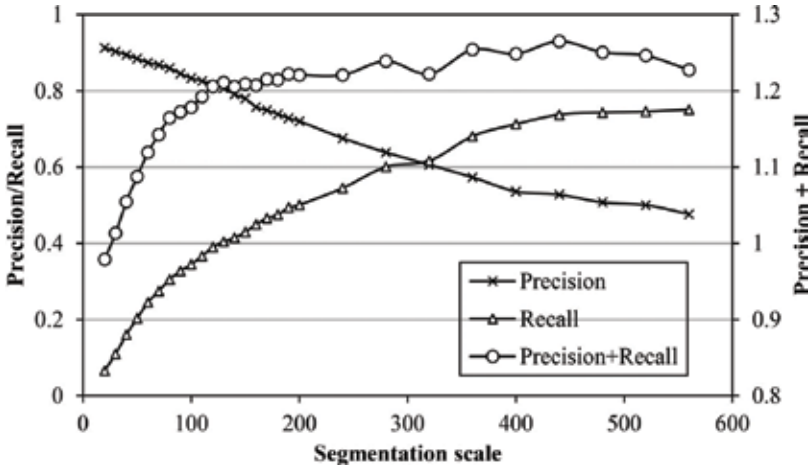

Figure 12. Precision and recall calculated between segments and reference, and their sum for area 1.

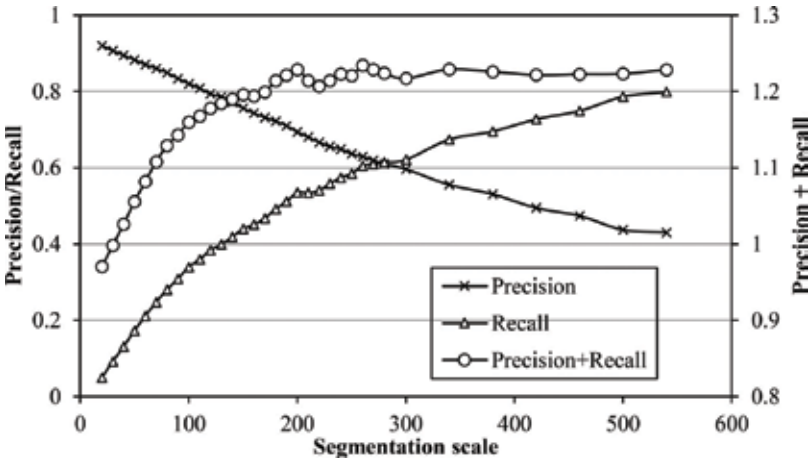

Figure 13. Precision and recall calculated between segments and reference, and their sum for area 2.

Therefore, theoretically, the indicator values start to show significant changes before and after this segmentation scale [25], but owing to differences in segmented terrain in the experimental area, extremely low values do not always appear. Generally, the segmentation scale region before the sum of the normalized variance and normalized Moran's I index starts to show stable changes is used as the optimal segmentation scale. In addition, the results of the sum of the normalized variance and normalized reverse Geary's C index were not good (**Figure 10**), as abnormal changes occurred at smaller scales. This is due to the oversensitivity of the reverse Geary's C index, and the sum of the two is not recommended. For single indicators, the reverse Geary's C index is recommended, although in experimental area 2, the combination of the two (**Figure 11**) was similar to the performance of the sum of the normalized variance and normalized Moran's I index in experimental area 2 (**Figure 9**), or even more significantly, represents the optimal segmentation scale.

7.2. Precision indicator analysis of multiscale segmentation results

This section mainly evaluates the segmentation quality of different segmentation scales by referencing polygon testing of the segmentation results. At the same time, the performance of the abovementioned indicators is validated in order to provide reliable reference information to determine which indicators are more suitable for representing the optimal segmentation scale. **Figures 12** and **13** demonstrate the precision and recall indicators of the two experimental areas and the changes in these two indicators with changes in scale. It can be clearly seen that the precision indicator decreases when the scale increases, whereas the recall indicator increases when the scale increases. The sum of the two increases when scale increases, and starts to become stable within a suitable scale range. Ideally, the larger the sum of the precision and recall values, the better the segmentation result. As these two indicators are sensitive to over-segmentation and under-segmentation, respectively, similar to the consistency and autocorrelation indicators, the optimal segmentation scale is assumed to be the scale at which both indicators start to become stable. Therefore, for experimental area 1, the optimal segmentation scale should be in the region of scale 130, whereas that of experimental area 2 should be in the region of scale 150, and this is similar to the analysis results of Section 3. Therefore, the sum of the region-based precision and recall indicators can effectively show the optimal segmentation scale, which was consistent with the analysis results of [37]. Furthermore, when the sum of the consistency measures and autocorrelation measures is plotted with the sum of precision and recall, it can be clearly see that the combined value of the consistency measures and autocorrelation measures can represent the region when the combined precision and recall indicators start to become stable, that is, the sum of the consistency and autocorrelation measures also starts to show the corresponding scale regions during significant changes. **Figures 14** and **15** show the best combination in the two experimental regions: for experimental area 1, it is the sum of the normalized variance and Moran's I (**Figure 14**), and for experimental area 2, it is the sum of the normalized variance and reverse Geary's C (**Figure 15**). In the figures, the corresponding dotted vertical lines are artificially identified optimal scales.

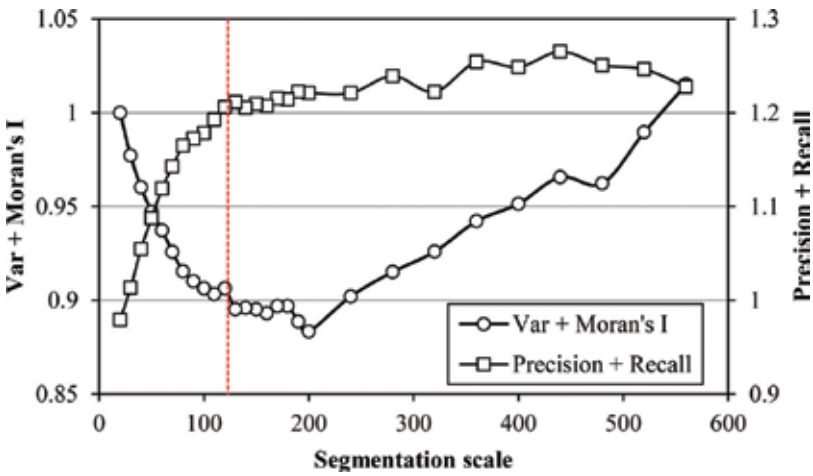

Figure 14. Precision and recall calculated between segments and reference, and the sum of the normalized variance and Moran's I for area 1.

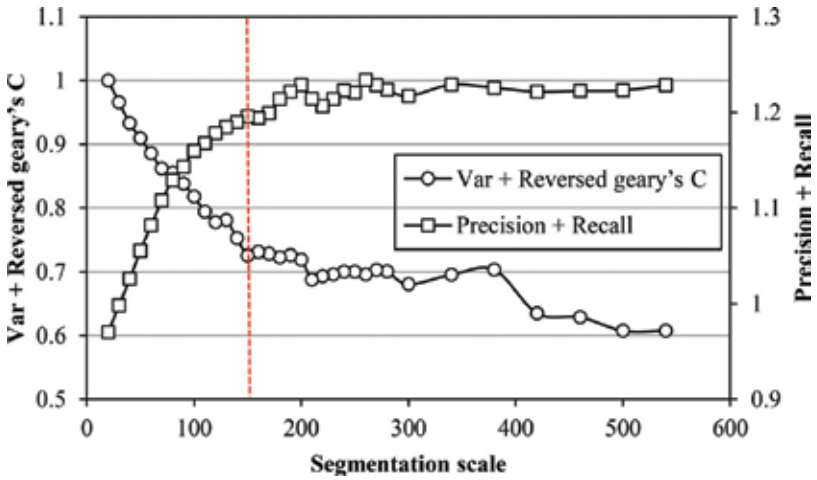

Figure 15. Precision and recall calculated between segments and reference, and the sum of the normalized variance and reverse Geary's C for area 2.

7.3. Top-down decomposition based on autocorrelation measures

Currently, the majority of scale optimization studies all have a goal of obtaining single optimized scales [38, 39]. However, according to the study by [34], the optimized scales of different terrains are different and purely relying on the identification of single optimized scales is essentially not in line with the core thinking of object-oriented remote sensing analysis. Here, we attempted to propose a top-down multiscale segmentation scheme with an aim of obtaining the optimized segmentation results of different terrains. **Table 1** shows the corresponding sum of the precision and recall indicators at different scales for experimental area 1. The maximum or local maximum values in different categories do not always appear on the overall optimal segmentation scale. Here, we used the reverse Geary's C to achieve a top-down decomposition of under-segmented objects. A reverse Geary's C value of 1 indicates that positive autocorrelation exists in the object and the segmentation objects in various layers in the top-down decomposition are obtained using the consistency of adjacent objects to determine the bottom-up merger. Therefore, a high degree of autocorrelation exists in the object set in the lower layer that is included in the upper layer. Through testing, we found that the local reverse Geary's C indices in the object set in the lower layer that is included in the objects in the middle and upper layers in the experiment area are all large and approached 1. Therefore, the threshold values in this test include 0.999, 0.997, and 0.995. If the calculated reverse Geary's C index in the objects in the upper layer, which include objects in the lower layer, is smaller than these values, the objects in the upper layer are disintegrated, that is, the object sets in the layer are retained. **Figure 16** shows the layer-by-layer decomposition result from segmentation scale 320 to scale 50, when the experimental area 1 is below the threshold value of 0.999. It can be seen that this not only retained the overall characteristics of cultivated land and buildings, but the segmentation of forests is also refined. In particular, the proposed method can better represent buildings. **Figure 16(a)** and **(b)** shows the results of top-down decomposition and optimal segmentation scale 130, respectively. **Figure 16(c)** and **(d)** show the optimal segmentation scale 130 result and top-down decomposition result, respectively. The experiments showed that this

Scale	Forests	Roads	Cultivated land	Buildings	Bare land
520	1.434	1.194	1.234	1.242	1.617
480	1.437	1.196	1.236	1.267	1.614
440	**1.443**	1.181	1.259	1.316	1.641
400	1.398	**1.200**	1.265	1.338	1.670
360	1.353	1.145	1.329	1.345	1.686
320	1.251	1.140	1.358	1.367	**1.705**
280	1.261	1.154	1.383	1.401	1.702
240	1.216	1.127	1.395	1.409	1.683
200	1.153	1.119	1.456	1.448	1.667
190	1.151	1.131	1.456	**1.459**	1.664
180	1.129	1.127	1.461	1.447	1.659
170	1.122	1.127	1.471	1.430	1.642
160	1.103	1.128	1.466	1.439	1.646
150	1.093	1.132	1.483	1.440	1.634
140	1.081	1.134	1.482	1.446	1.621
130	*1.078*	*1.136*	*1.501*	*1.452*	*1.592*
120	1.073	1.125	1.493	1.451	1.583
110	1.062	1.152	1.471	1.440	1.583
100	1.054	1.151	1.449	1.431	1.526
90	1.044	1.142	1.444	1.421	1.532
80	1.041	1.142	1.425	1.414	1.513
70	1.036	1.133	1.381	1.392	1.454
60	1.026	1.126	1.341	1.375	1.408
50	1.021	1.112	1.278	1.341	1.350
40	1.017	1.107	1.206	1.320	1.285
30	1.012	1.095	1.123	1.284	1.190
20	1.005	1.054	1.055	1.239	1.121

Table 1. Sum of precision and recall at each scale for area 1. Bold values indicate the optimal segmentation scale in different categories. Italic value indicate the overall optimal segmentation scale for all categories.

method can make up for the deficiencies in merging when the bottom-up multiscale segmentation only considers the consistency of adjacent objects.

7.4. Comparison of results of single-scale and multiscale decomposition

Assume that the optimal segmentation scale of experimental area 1 is 130; then, the corresponding precision and recall indicators of various categories are as shown in **Table 2**. **Table 2** shows the summation of the precision and recall indicators of various categories that were obtained from the accuracy validation of the segmentation results of gradual decomposition from scale 320 to 50

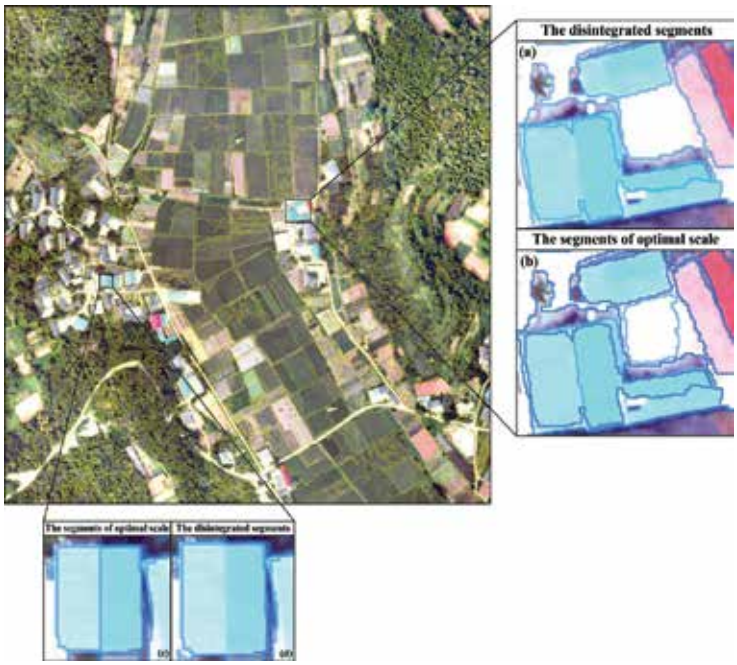

Figure 16. Disintegrated results from scale 320 to 50 using threshold 0.999.

Different methods	Forests	Roads	Cultivated land	Buildings	Bare land
Optimal scale	1.078	1.136	1.501	1.452	1.592
Decomposition result	1.060	1.124	1.436	1.478	1.678

Table 2. Sum of precision and recall at the optimal scale and redefined segments for area 1.

using a threshold value of 0.999, and the comparison of this with the accuracy determined from the optimal segmentation scale of 130. It can be seen that this method can result in the sums of the precision and recall accuracy of forests, roads, and cultivated land being worse than the single optimal scale used for discrimination. However, this method can simultaneously greatly increase the segmentation accuracy of buildings (**Figure 16**) and retain the segmentation characteristics of bare land to a maximum degree. The sum of the precision and recall accuracy was better than at scale 130. It can be seen that the proposed method can effectively improve the segmentation results of urban areas or regions with high consistency (such as buildings and bare land). However, the results of this method may be worse for forests, cultivated land, or other regions with similar spectra. Therefore, this method must be used selectively, such as in study sites that are dominated by urban areas or consistent regions.

8. Chapter summary

This chapter presented the use of drone-based remote sensing images to evaluate the quality of the MRS algorithm for the segmentation of drone images, tested the sensitivity of different

segmentation evaluation indicators, and proposed an optimization protocol for segmentation scales. First, the consistency and heterogeneity measures of the object were used to test the sensitivity of different indicators in multiscale segmentation results. The results showed that it is more difficult to find optimal scales by using single indicators. A combination of area-weighted variance (consistency) and Moran's I spatial autocorrelation index (heterogeneity) can simultaneously account for the internal consistency of the object and the heterogeneity between objects, such that the optimized segmentation object can internally achieve maximum homogeneity and maximum heterogeneity can be achieved between objects, which is more conducive to discovering the optimal segmentation scale. For normalized combined indicators, the combined results of the normalized variance and normalized Moran's I were found to be better than the results of the normalized variance and normalized reverse Geary's C. Through a combination of normalized precision and recall measures, we found the optimal segmentation scale region for experimental areas 1 and 2. These results can provide an empirical reference for the optimization of segmentation in drone-based remote sensing images. Compared with other indicators, the reverse Geary's C is more sensitive to the segmentation scale, as the top-down object decomposition protocol based on its spatial autocorrelation indicator can improve the segmentation results of different terrains. However, this method does not show good results for forests or cultivated land, which have low spectral consistency. Therefore, based on the results of this research, it is recommended that this method be selectively used.

Acknowledgements

This work was supported by the National Natural Science Foundation of China (No. 41701374), the Natural Science Foundation of Jiangsu Province of China (No. BK20170640), the China Postdoctoral Science Foundation (No. 2017 T10034, 2016 M600392), and the National Key Research and Development Program of China (No. 2017YFB0504200). We are also grateful to anonymous reviewers and members of the editorial team for advice.

Author details

Lei Ma[1,2]*, Gaofei Yin[3], Zhenjin Zhou[1,2], Heng Lu[4] and Manchun Li[1,2]

*Address all correspondence to: maleinju@gmail.com

1 Jiangsu Provincial Key Laboratory of Geographic Information Science and Technology, Nanjing University, Nanjing, China

2 School of Geographic and Oceanographic Sciences, Nanjing University, Nanjing, China

3 Institute of Mountain Hazards and Environment, Chinese Academy of Sciences, Chengdu, China

4 State Key Laboratory of Hydraulics and Mountain River Engineering, Sichuan University, Chengdu, China

References

[1] Laliberte AS, Rango A. Image processing and classification procedures for analysis of sub-decimeter imagery acquired with an unmanned aircraft over arid rangelands. GIScience & Remote Sensing. 2011;**48**(1):4-24

[2] Zhang CH, Kovacs JM. The application of small unmanned aerial systems for precision agriculture: A review. Precision Agriculture. 2012;**3**(6):693-712

[3] Ma L, Li MC, Tong LH, et al. Using unmanned aerial vehicle for remote sensing application. In: 21st International Conference on Geoinformatics; 20–22 June 2013, Kaifeng, China; 2013. pp. 1-5

[4] Gomez-Candon D, De Castro AI, Lopez-Granados F. Assessing the accuracy of mosaics from unmanned aerial vehicle (UAV) imagery for precision agriculture purposes in wheat. Precision Agriculture. 2014;**15**(1):44-56

[5] Dunford R, Michel K, Gagnage M, et al. Potential and constraints of unmanned aerial vehicle technology for the characterization of mediterranean riparian forest. International Journal of Remote Sensing. 2009;**30**(19):4915-4935

[6] Sugiura R, Noguchi N, Ishii K. Remote-sensing technology for vegetation monitoring using an unmanned helicopter. Biosystems Engineering. 2005;**90**(4):369-379

[7] Patias P, Saatsoglou-Paliadeli C, Georgoula O, et al. Photogrammetric documentation and digital representation of the macedonian palace in Vergina-Aegeae. CIPA, XXI International CIPA Symposium; 1–6 October 2007, Athens

[8] Dong L, Shan J. A comprehensive review of earthquake-induced building damage detection with remote sensing techniques. ISPRS Journal of Photogrammetry and Remote Sensing. 2013;**84**:85-99

[9] Primicerio J, Di Gennaro SF, Fiorillo E, et al. A flexible unmanned aerial vehicle for precision agriculture. Precision Agriculture. 2012;**13**(4):517-523

[10] Blaschke T, Hay GJ, Kelly M, et al. Geographic object-based image analysis–Towards a new paradigm. ISPRS Journal of Photogrammetry and Remote Sensing. 2014;**87**:180-191

[11] Li M, Ma L, Blaschke T, Cheng L, Tiede D. A systematic comparison of different object-based classification techniques using high spatial resolution imagery in agricultural environments. International Journal of Applied Earth Observation and Geoinformation. 2016;**49**:87-98

[12] Ma L, Li M, Ma X, Cheng L, Du P, Liu Y. A review of supervised object-based land-cover image classification. ISPRS Journal of Photogrammetry and Remote Sensing. 2017a;**130**:277-293

[13] Ma L, Fu T, Blaschke T, Li M, Tiede D, Zhou Z, Ma X, Chen D. Evaluation of feature selection methods for object-based land cover mapping of unmanned aerial vehicle imagery using random forest and support vector machine classifiers. ISPRS International Journal of Geo-Information. 2017b;**6**(51):1-21

[14] Witharana C, Civco DL. Optimizing multi-resolution segmentation scale using empirical methods: Exploring the sensitivity of the supervised discrepancy measure Euclidean distance 2 (ED2). ISPRS Journal of Photogrammetry and Remote Sensing. 2014;**87**:108-121

[15] Witharana C, Civco DL, Meyer TH. Evaluation of data fusion and image segmentation in earth observation based rapid mapping workflows. ISPRS Journal of Photogrammetry and Remote Sensing. 2014;**87**:1-18

[16] Smith A. Image segmentation scale parameter optimization and land cover classification using the random forest algorithm. Journal of Spatial Science. 2010;**55**(1):69-79

[17] Kim M, Warner TA, Madden M, et al. Multi-scale GEOBIA with very high spatial resolution digital aerial imagery: Scale, texture and image objects. International Journal of Remote Sensing. 2011;**32**(10):2825-2850

[18] Myint SW, Gober P, Brazel A, et al. Per-pixel vs. object-based classification of urban land cover extraction using high spatial resolution imagery. Remote Sensing of Environment. 2011;**115**(5):1145-1161

[19] Hussain M, Chen DM, Cheng A, et al. Change detection from remotely sensed images: From pixel-based to object-based approaches. ISPRS Journal of Photogrammetry and Remote Sensing. 2013;**80**:91-106

[20] Dr guț L, Csillik O, Eisank C, et al. Automated parameterisation for multi-scale image segmentation on multiple layers. ISPRS Journal of Photogrammetry and Remote Sensing. 2014;**88**:119-127

[21] Arbiol R, Zhang Y, Palà V. Advanced classification techniques: A review. In: ISPRS Commission VII Mid-Term Symposium Remote Sensing: From Pixels to Processes, Enschede, the Netherlands. 2006. pp. 292-296

[22] Laliberte AS, Rango A. Texture and scale in object-based analysis of subdecimeter resolution unmanned aerial vehicle (UAV) imagery. IEEE Transactions on Geoscience and Remote Sensing. 2009;**47**(3):761-770

[23] Johnson B, Xie Z. Unsupervised image segmentation evaluation and refinement using a multi-scale approach. ISPRS Journal of Photogrammetry and Remote Sensing. 2011;**66**(4): 473-483

[24] Zhang H, Fritts J, Goldman S. Image segmentation evaluation: A survey of unsupervised methods. Computer Vision and Image Understanding. 2008;**110**(2):260-280

[25] Kim M, Madden M, Warner T. Estimation of optimal image object size for the segmentation of forest stands with multispectral IKONOS imagery. In: Blaschke T, Lang S, Hay GJ, editors. Object-Based Image Analysis: Spatial Concepts for Knowledge-Driven Remote Sensing Applications. Berlin, Heidelberg: Springer; 2008. pp. 291-307

[26] Martha TR, Kerle N, van Westen CJ, et al. Segment optimization and data-driven thresholding for knowledge-based landslide detection by object-based image analysis. IEEE Transactions on Geoscience and Remote Sensing. 2011;**49**:4928-4943

[27] Chen J, Li J, Pan D, et al. Edge-guided multiscale segmentation of satellite multispectral imagery. IEEE Transactions on Geoscience and Remote Sensing. 2012;**50**(11):4513-4520

[28] Neubert M, Herold H, Meinel G. Assessing image segmentation quality – Concepts, methods and application. In: Blaschke T, Hay G, Lang S, editors. Object-Based Image Analysis: Spatial Concepts for Knowledge-Driven Remote Sensing Applications. Lecture Notes in Geoinformation & Cartography 18. Berlin: Springer; 2008. pp. 769-784

[29] Dronova I, Gong P, Clinton NE, et al. Landscape analysis of wetland plant functional types: The effects of image segmentation scale, vegetation classes and classification methods. Remote Sensing of Environment. 2012;**127**:357-369

[30] Baatz M, Schäpe M. Multiresolution segmentation-an optimization approach for high quality multi-scale image segmentation. In: Strobl J, Blaschke T, Griesebner G, editors. Angewandte Geographische InformationsVerarbeitung XII. Karlsruhe: Wichmann Verlag; 2000. pp. 12-23

[31] Benz UC, Hofmann P, Willhauck G, et al. Multi-resolution, object-oriented fuzzy analysis of remote sensing data for GIS-ready information. ISPRS Journal of Photogrammetry and Remote Sensing. 2004;**58**:239-258

[32] Espindola GM, Camara G, Reis IA, et al. Parameter selection for region-growing image segmentation algorithms using spatial autocorrelation. International Journal of Remote Sensing. 2006;**27**:3035-3040

[33] Geary RC. The contiguity ratio and statistical mapping. The Incorporated Statistician. 1954;**5**(3):115-145

[34] Ma L, Cheng L, Li M, et al. Training set size, scale, and features in geographic object-based image analysis of very high resolution unmanned aerial vehicle imagery. ISPRS Journal of Photogrammetry and Remote Sensing. 2015;**102**:14-27

[35] Martin D, Fowlkes C, Malik J. Learning to detect natural image boundaries using local brightness, color, and texture cues. IEEE Transactions on Pattern Analysis and Machine Intelligence. 2004;**26**(5):530-549

[36] Reich S, Abramov A, Papon J. A novel real-time edge-preserving smoothing filter. In: Proceedings of the International Conference on Computer Vision Theory and Applications, Barcelona, 2013. pp. 1-11

[37] Zhang XL, Feng XZ, Xiao PF, et al. Segmentation quality evaluation using region-based precision and recall measures for remote sensing images. ISPRS Journal of Photogrammetry and Remote Sensing. 2015;**102**:73-84

[38] Dr guț L, Tiede D, Levick S. ESP: A tool to estimate scale parameters for multiresolution image segmentation of remotely sensed data. International Journal of Geographical Information Science. 2010;**24**(6):859-871

[39] Ming DP, Li J, Wang JY, et al. Scale parameter selection by spatial statistics for GeOBIA: Using mean-shift based multi-scale segmentation as an example. ISPRS Journal of Photogrammetry and Remote Sensing. 2015;**106**:28-41

Section 4

Drone Applications

Chapter 6

The Use of Unmanned Aerial Vehicles by Urban Search and Rescue Groups

Marzena Półka, Szymon Ptak, Łukasz Kuziora and Aneta Kuczyńska

Additional information is available at the end of the chapter

http://dx.doi.org/10.5772/intechopen.73320

Abstract

In the case of natural or man-made disaster, the top priority of urban search and rescue (USAR) groups is to localise the victim as quickly as possible. Even minutes might play a crucial role in the victim's survival. A number of standard operating procedures may be applied to achieve best performance. Rescue dogs are trained to search for alive victims; special inspection cameras are used, before heavy equipment is being implemented. To improve the effectiveness of USAR group operations, innovative technologies might be implemented. The most recent solution is currently designed in MOBNET project, founded by EU under the Horizon 2020 programme. The scope of the project is to combine both cellular technology and early Galileo services to localise the smartphones of potential victims. Integration tests give some promising outcomes. The following chapter looks at typical applications, real needs of public services as well as the performance of the novel system.

Keywords: UAVs, S&R groups, rescue, EGNSS, GPS

1. Introduction

Unmanned aerial vehicles (UAVs), colloquially called drones, are currently the most innovative element used in support of various industrial sectors. The development rate of this industrial sector is catching up with expansion of the cellular or IT sector.

UAVs may be used in various types of activities of the public and private sector, namely:

- Public administration: border guards or services providing assistance after disasters or military services
- Enterprises: monitoring and maintenance of buildings, power companies, construction sites, agricultural facilities, farms, geological discoveries or aerial photographs
- Clients: deliveries of goods, advertising, guided trips and games

To put shortly each UAV is assumed to consist of two main components—the machine as such and the terrestrial control station or a mobile one. On the other hand, the drone comprises a system controlled in real time, control software, interface module to simplify the exchange of data, sensors connected with the software and the avionics. Optionally it may also have an arm control system (if equipped with weapons) or an autopilot. The terrestrial control station comprises control software, interface modules and the controlling person.

Such public services, for example, the fire service, are executing their operations in many fields connected with prevention, rescuing and civil protection. This is a great advancement as compared to the scope of obligations dating a few decades back. The dynamics of those changes has required (and still requires) continuous staff advancement, modernisation of the equipment base and revising adopted solutions with respect to rescue actions.

Given a certain natural division, selected fire service units are specialised in specific domains: technical rescuing, high rescuing, chemical and ecological rescuing, etc. There is also an area connected with elimination of consequences of events of a greater magnitude. Search and rescue groups may go into the state of combat readiness in a few dozen of hours. If means and resources of local communities are insufficient to handle the disaster, the state can formally apply for assistance by launching, for example, a heavy urban search and rescue (HUSAR) group, which has the most extensive scope of competencies and a developed equipment base. The activity of the group may be proven by the most recent dispatches of the Polish HUSAR group:

Earthquake in Nepal (May 2015)

Polish rescuers along with 12 dogs trained to search for survivors and 6 tonnes of equipment were used to search Nepal devastated by the earthquake. The action lasted 11 days. Almost 9000 persons have lost their lives during this incident [1]. For each urban search and rescue group that reached the scene, a particular area to be searched has been assigned. Taking into consideration the size of the disaster, the whole operations required immensely well-coordinated organisation. In fact, the survival of the victims was depending on hours between the incident and the USAR teams to localise the victim. In total, not many alive victims has been found. It is clear that the most valuable resource in case of man-made or natural disaster, where many victims need to be found and rescued, is time.

Earthquake in Haiti (January 2010)

An earthquake of 7° in the Richter scale caused a few hundred thousand victims. A group of Polish rescuers comprising 54 officers and 10 snuffer dogs arrived in Port-Au-Price. High

temperatures were not supportive for work of the rescuers [2]. As there were many USAR teams invited to support the operations, it was a difficult coordination task for local authorities. With extraordinary damages to the infrastructure, it caused significant delays in reaching some areas, especially distant, as the accessibility was limited.

Previously described disasters took place a couple of years ago. In both cases, but also in smaller incidents of regional/national range, the rescuers were fighting with the toughest enemy—the time. It is impossible to improve the deployment time; as the equipment must be prepared, members of USAR team must gather, and some further organisational arrangements must be made. The time necessary to transport these resources on the scene is also unavoidable. After arrival, reaching the scene might also be difficult, due to the infrastructural damages. That is why every minute after arrival might be crucial for the victims' survival. If we cannot shorten the described above deployment/transportation time, it seems that the most important aspect to be considered is the effectiveness of the search and rescue operations.

Search and rescue action groups are generally considered a certain type of "elite units" in the fire service. They remain in constant readiness, go through training courses lasting several hours and also personally train their rescue dogs that are allowed to participate in the actions once they have passed a special exam. Together with such equipment, as inspection cameras or geophones, this is a highly effective way of searching for surviving victims, e.g. in the cited earthquakes. Can modern technologies replace those infallible traditional search methods? Absolutely not. Yet quite clearly they may enhance the effectiveness of conducted search actions. UAVs are a good example. At times of universal access to different types of mobile devices, almost every person carries a mobile phone. This could be used for search needs. A victim lying under the rubble may have a cell phone which would remain switched on until the battery becomes empty, provided it has not become damaged during the event as such. The telephone will try getting a connection with the closest base station. The question is, does having an own base station allow supporting rescue actions?

The response to this question will be presented in subsequent subchapters. It should be emphasised that although this chapter focuses primarily on the use of UAVs in the operation of search and rescue groups, the proposed solutions will easily facilitate implementation in the activity in other public services, such as protecting facilities of particular importance, control of state borders, and assuring security during mass events.

2. Identification of needs

2.1. S&R operations: typical activities

Actions of search and rescue groups are implemented according to strictly defined procedures, which may be basically divided into two categories: local (domestic) and international ones (e.g. under UN-INASARAG). Those procedures regulate among others such aspects as operating readiness and equipping and also regulate among others such aspects as operating

readiness, equipping and the size of groups. In general terms, the operation performed by groups during an action may be divided into four basic phases [1]:

1. Mobilisation
2. Action
3. Demobilisation
4. End of mission

The second phase (action), which takes place on the area afflicted by the disaster, requires coordination of actions of all specialised groups present on the spot. To be able to provide effective help to victims, rescue activities performed on the disaster scene are divided into five consequent stages:

a. Reconnaissance, including identification of hazards and determination of the size of the hazard zone
b. Initial determination of the number of missing persons
c. Securing, including lighting of the scene
d. Finding persons present in inaccessible places
e. Reaching victims with the use of available equipment, granting competent first aid, evacuation of victims and persons at risk from the hazard zone

Each stage should be properly planned and implemented. The first step to be executed on the scene is among others the determination of the size of hazard zone. Given the nature of the activities, in many cases this stage may not be executed quickly or accurately. During large-scale building disasters, caused in particular by earthquakes, the size of hazard zones is considerable, and as an effect, reaching and identifying all areas requiring intervention, for example, owing to cutting off of transport routes, as a rule tend to be hindered.

For this reason one of the implementation methods of this task is a surface search, in other words an accelerated one. It consists in a rapid extensive surface search of the area afflicted by the disaster in order to find areas characterised by high survivability level, like persons immobilised by minor rubble. This solution is strictly connected with restrictions concerning the number of rescuers.

It is assumed that this state would remain unchanged, i.e. the number of rescuers on the scene would not be increased, and so to optimise the search process, it is necessary to have increasingly novel solutions deployed.

2.2. Innovations in fire service

Advanced search methods with the use of modern technologies, such as geographic information system (GIS), rescuers' communication and positioning systems, thermal vision, modern off-road vehicles or unmanned aerial vehicles, clearly improve the possibility of effective execution

of a rescue action. Correct and effective search actions may be performed by thorough planning of activities and maximum usage of the available resources and means.

It should be assumed that at present modern solutions adopted by specialised search and rescue groups should comprise the following.

2.2.1. Making use of precise digital maps (GIS) with the GPS technology (or an optional one)

This type of maps may take into consideration all-terrain obstacles and the location of available resources and means, as well as data bases related to potential trends in the behaviour of missing persons, which in combination with local terrain and weather conditions at disposal of professional rescuers from the given region may significantly accelerate making appropriate decisions. Maps should be available at the command stand, both stationary ones and also of the mobile type, to allow handling data received from communication module-based GPS systems (or different ones) and their transfer to the base and to the database serving as the centre of the GIS. Particular elements may be visualised in the system and enable accurate identification of their type by verifying the equipment ID and its current position. The map displays the position of rescuers determined based on a signal sent from radiotelephones with an installed GPS receiver. The effectiveness of this type of solution is nevertheless limited by the necessity of preparing maps prior to the occurrence of the hazard. However during actions performed on the same area, this solutions gains on effectiveness with the number of events occurring on the area under protection. Consequently digital maps should be dedicated to rescue groups protecting the defined area, for example, mountain rescue service [2].

2.2.2. Ground units used in search and rescue actions

The equipping of search and rescue groups that facilitates the process of searching and locating missing persons, as well as their safe evacuation, comprised all types of mechanical vehicles having diverse type of drive equipped with wheels or tracks. Also, in this respect, novel structures are being developed to support rescuers in their actions. Evacuation may be executed also by air with the use of rescue helicopters; nevertheless difficult weather conditions, relatively high usage costs, lack of available landing place or safe handling of the victims and a considerably low number of such equipment units available make it necessary to seek other solutions that would be much cheaper and more resistant to adverse weather conditions and difficult terrain conditions. Such accessories comprise road vehicles or track and wheel vehicles, such as off-road vehicles, quads, all-terrain vehicles or amphibians (**Figure 1**) [4, 5].

2.2.3. Unmanned aerial vehicles (UAVs)

The use of unmanned aerial vehicles is becoming increasingly popular in actions performed by rescue groups. Most frequently used unmanned aerial vehicles are multicopters, which are capable of vertical take-off and hovering, as well as airplanes or motor gliders, which take off from roads or a special catapult. Selecting the appropriate type of UAVs entails certain advantages and drawbacks. The main drawback of multi-propeller airplanes is their available flight time, which as a rule tends to be within the range of 15–60 minutes depending on the battery size. On the other hand, the main advantage of multi-propeller

airplanes is their manoeuvrability, which in combination with their furnishing with a dedicated camera may considerably reduce the impact of terrain conditions with the use of UAV for search activities, and their furnishing with thermal vision cameras allows finding people even after twilight (**Figure 2**). Unmanned aerial vehicles may also be used for drawing up orthophotos or to provide the view of the scene of actions from a close distance.

2.3. A gap for dedicated UAV applications?

The application of modern technologies in rescuing is highly desirable. Search and rescue groups, the specific nature of actions of which is connected with carrying out actions in difficult terrain conditions, have been found to have particular needs. Given the increasingly frequent access to modern technologies, more and more frequently use is being made of geolocation technologies, and the usage of unmanned aerial vehicles in actions, and consequently the combination of both strategies seems to be a natural step in the implementation of those solutions in rescue actions. The MOBNET system is implementing this trend by using cellular phone signals, the GALILEO system, the European navigation system to localise signals with an accuracy of even 10 cm and unmanned aerial vehicles. The rate and accuracy of localising offered by the system, which is made possible thanks to the fact that according to the Digital in 2017 Global Overview Report ca. 66% people worldwide use their mobile phones every day, are aimed at finding a tool to support considerable search and/or rescue actions.

Figure 1. Example of ground units (a) adapted to driving in a complex terrain trailer pulled by Land Rover Defender 110 [3], (b) all-terrain vehicle Swincar [4] and (c) ARGO 8 × 8 amphibious vehicle in a track and wheel version [5].

Figure 2. View from thermal vision camera provided on UAV—looking for missing persons [6].

http://dx.doi.org/10.5772/intechopen.73320

3. Methods

In response to needs of the market, in the first place of rescue services in the context of enhancing the effectiveness of search actions, an idea was conceived of building an aerial vehicle dedicated to this particular type of activity. As the solution should be best tailored to needs of final users, in the first place, the target groups have been identified. The most important ones of them include the following:

- Superior user: the fire service (search and rescue actions) as a consequence of building disasters, natural calamities, search of missing persons on larger areas and possibly also finding rescuers during diverse types of actions
- Public order services (support during mass events, identification of persons inside a premise)
- Border security services (detection of potential smugglers, persons crossing the border illegally)
- Institutions that control access to specific facilities (protection of critical infrastructure, access control)
- Other services (search for persons in isolated persons with hindered access)

The executed analysis allowed a detailed definition of receiver groups, at which surveys have been addressed. The objective of this kind of survey was to allow compiling opinions concerning current needs related to access to new technologies, such as UAVs. This was a determinant during the MOBNET system designing process. It also enabled the establishment of a data base of stakeholders in this solution thanks to describing project assumptions.

Key issues about which the respondents were asked included the following:

- Personal and contact data (education, professional experience, nationality)
- Potential use of the MOBNET system
- Required accuracy of the location of the victim, number of concurrently located cell phones
- System operating time (on internal power source)
- System operating conditions (threshold, temperature, humidity, wind speed, precipitation, etc.)
- Involvement of rescuers (number of persons who could handle the system in typical conditions, system weight, transport options)
- Requirements concerning the user interface (display of specific data, visualisation, etc.)

Thanks to such structuring of the survey, its results allowed making a detailed delimitation of rules for system functioning. In addition the received responses served also as guidelines for designing the user interface.

4. Survey outcomes

Result of the survey allowed obtaining an image of the optimum solution—a system which would contribute to optimising search actions, in which use is made of a combination of the satellite positioning system (GPS) and cellular technology (DCT).

A total of approximately 300 surveys have been sent out to selected target groups. Sixty-seven responses were received from respondents from four member states of the European Union. Almost a half of them were firemen. Further 15% were border guards. The remaining professions of the respondents included members of search and rescue groups, policemen and soldiers. A median in the set containing the number of years of the respondents' professional experience equalled to 19 years.

Below presented were selected results of the survey.

Figure 3 shows that the respondents did not care too much about the relatively low system inaccuracy. This arose from the nature of typical search and rescue actions. Firemen are, for example, forced to remove heavy structural elements, and so the indication of an area where a person is localised usually appears to sufficient.

It may naturally be expected that the longer the time of using of the system, the better. Taking into account the obtained responses, it may be assumed that an operating time of a few dozen minutes between subsequent charging and replacement of battery would be optimum. Furthermore, taking into account the nature of system operation, all signals would be detected almost in real time, which allows finishing the flight and turning over data to the commander of search actions. Representatives of other services, in particular of border guards, specified much longer times, which are the result of the system used that is most typical for them, namely, flights over the border area.

A question of particular importance for the project concerned information indispensable for UAV operator. Respondents specified in the first place the GPS position, preview of map of the land over the drone is moving, the flight trajectory and the video transmission. As regards categories included in the "other" section, they included among others wind speed, starting position of the UAV, number of detected signals, flight time and ambient temperature.

Figure 3. Selected results of the conducted survey: system inaccuracy (to the left), minimum operating time (centre) and components of user interface (to the right).

As regards the execution of actions, the respondents were asked for feedback concerning issues related to system operation in real time. The obtained responses have shown that the system should be capable of searching ca. 10,000 m^2 during a 30-minute flight. It should be operating within the range of ambient temperature from −20 to +50°C, at a wind speed of even 10 m/s. Furthermore, the distance of the aerial vehicle from the operator should, in the opinion of respondents, be ca. 550 m horizontally and ca. 300 m vertically.

The majority of respondents were of the opinion that it would be possible to use their own operator (81%), while 66% of them saw the possibility of involving at least two rescuers in the operation of the system (during the execution of their typical activities).

A question of particular importance was one concerning the number of concurrently detected signals (mobile phones). In the opinion of almost 50% of respondents, it was sufficient to detect up to 10 signals during one mission. One third of the respondents marked the necessity of detecting up to 100 telephones simultaneously. Three respondents were convinced that the system should be capable of detecting more than 100 signals, yet this applies to the proposed system application during mass events (for needs of registration and potential control of the presence of a given person among participants of the event).

5. Technical approach

5.1. The principles of operations of UAV

Unmanned aerial vehicles (UAVs) may be used to execute a wide spectrum of tasks, which helps reduce the risk that may take place during their implementation by manned aerial vehicles and potentially reduce costs of their usage. Basic structural types of UAVs include unmanned airplane, unmanned airplane with a possibility of rotor rotations, unmanned helicopter and gyroplanes (multicopter). Gyroplanes are capable of changing the flight direction in a brief time and have the capacity of zero-distance start and landing and precise spot hovering over the scene of an incident. They are also adapted to operating in very confined spaces.

The advantage of the drones is that it is no longer necessary for a person to be directly in the helicopter, but he may control it personally from a safe place. This also implies savings of means connected with production, operation and training, even though handling of such equipment also requires outlays connected with obtaining the relevant licences. On the other hand, one of the possible hazards is inexperienced operators unable to use them in a safe way.

In the context of finding victims, drones are not the only available solution. The methodology analysed in this chapter is based on measurements of the propagation force of radio waves that are emitted by cellular phones. An important assumption is that victims being rescued remain in the vicinity of their phones. The strength of signal coming from persons inside buildings is subject to nonlinear disturbances, which may cause significant deformations of the obtained estimated locations of victims. Alternative traditional methods of finding victims comprise search made by man or the usage of snuff dogs.

Drones are the perfect choice for use on contaminated areas, locations of difficult access or ones that pose a hazard for people. This may be illustrated by the example of the problem of cleaning up the contaminated nuclear power plant in Fukushima, even though in this particular case not drones, but unmanned robots were used. This is a scenario in which human abilities cannot be used directly. On the other hand, in such difficult conditions (given temperature and radiation), already 10 robots have been lost during the execution of works on this location (state as on March 11, 2017).

Thanks to their dimensions, drones are also less susceptible to changing weather conditions (this is determined by the type of machine), which makes them easier to use. They may be used during extreme weather conditions, as well as in locations with difficult access, eliminating a hazard for the pilot's health and life. Another advantage is the fact that they may approach facilities or the ground more closely, which allows more accurate and easier diagnosis of potential damage. The deployment of this solution allows increasing the repeatability and accuracy of control and also significantly reduces the operation time.

5.2. Proposed solution: technical aspects

The GPS system informs of the situation of UAV in the air and its flight direction. Thanks to satellite navigation, the installed GPS system finds the accurate position of UAV over the land surface. This system has been provided in the fuselage. In addition, UAV may be equipped with high-quality cameras that record images in real time and allow the location of a potential victim. High-resolution video recorders are not the only advantages offered by the drones. They are also furnished with thermal vision cameras that enable archiving images and recording thermal radiation emitted by almost each physical body. This allows them to operate during the night and in difficult weather conditions.

5.3. The concept of MOBNET

MOBNET has been established to localise victims during natural disasters and extraordinary circumstances, such as earthquakes, hurricanes or snow blizzards. It may also assist rescue services in such activities as the search and finding of missing persons. To ensure precise localisation, the device is compatible with the European satellite navigation system EGNSS, which is characterised by a small margin of error (ca. 1 m). Cellular phones emit a signal in the form of data at regular intervals, so the use of the DCT technology in the device will allow the detection and identification of victims during rescue actions. In the prototype being in the phase of development, the EGNSS and DCT technologies are fully synchronised to assure the most accurate finding possible. During works over the device, an effective and infallible communication link will be developed between unmanned aerial vehicles (UAV) and the terrestrial station. The objective is to obtain a data link which would enable incessant communication of commands between elements. The new system will allow making use of European global satellite navigation systems (EGNSS) including its earlier applications, such as Galileo, and EGNOS, and also digital cellular technologies (DCT), which is to enable the localisation of victims in situations in which access to them is hindered, dangerous or impossible. **Figure 4** presents an operating diagram of the MOBNET system.

http://dx.doi.org/10.5772/intechopen.73320

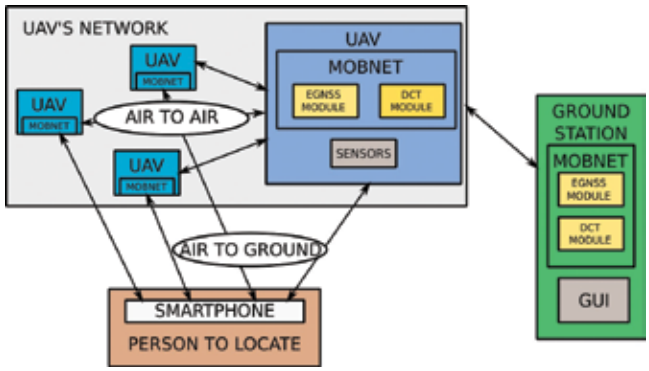

Figure 4. Operating concept of the MOBNET system [7].

6. Conclusions

Actions of search and rescue groups are challenging for many reasons. Above all those actions are carried out as a rule on an unknown area, in many cases abroad, and the terrain conditions tend to be complex. Given restrictions connected with personnel, new methods and technologies are being sought which may significantly affect the effectiveness of those actions. Enhancing the effectiveness of activities of search and rescue groups is strictly connected with performing a quick and precise determination of the size of the hazard zone and localisation of persons at risk. Consequently the MOBNET project, which makes use of a technology based on the system that localises signals of cellular telephone in a way which would eliminate any inconveniences connected with difficult terrain conditions, concurrently allowing obtaining a picture of the incident scene from above, seems to be a very good solution enhancing the effectiveness of actions performed by search and rescue groups.

Typical solutions for search and rescue actions comprise the usage of specially trained dogs, inspection cameras, geophones, etc. At a time of dynamic technological progress, new possibilities keep appearing. Innovative implementation of both the EGNNS technology and DCT opens new possibilities to public services. The identification of signals emitted by cellular phones naturally cannot replace proven traditional methods yet may to a large extent contribute to improving the effectiveness of the search actions. In particular in the case of vast areas, the MOBNET system may indicate the most important zones where resources and means would be sent as priority. This is due to the fact that in such situations, even mere minutes can determine the survival of the victims.

Under the MOBNET programme, a ready solution was offered for public services. The system has been extensively tested with view to integration of particular components. In February 2018, a demo meeting is to take place, during which detailed results of the project are to be presented. Tests in simulated conditions comprise scenarios of incidents typical for search and rescue groups.

By the time this manuscript was being prepared, the integration test took place. The results of in-field testing were satisfactory. The performance of MOBNET system fulfilled all prerequisites took at the beginning of the project. It is able to localise cell phones basing on an innovative approach connecting DCT and EGNSS technologies.

The conducted survey allowed the identification of structural limitations required by final users. The diversity of professions of the respondents also allowed obtaining suggestions concerning further development of the system and potential areas where the ready MOBNET system may be deployed.

It is important to notice that the system might be implemented not only in fire service. As the survey outcomes showed, there are many different potential fields of application. Other public services might use the MOBNET system, e.g. police might log the phones active in particular area, and boarder police might track the violation of boarder integrity. It might be used to control the areas of limited access for unauthorised personnel.

The popularity of smartphone usage is constantly growing. Most of us carry the device with ourselves during the whole day. Therefore it is highly probable that the localization of our cell phone will be equal with the localization of ourselves. And that is particularly identified gap that might be filled with the MOBNET system, in purpose to improve the effectiveness of search and rescue operations.

Acknowledgements

This publication is a part of MOBNET project dissemination activities. The project has received funding from the European Union's Horizon 2020 research and innovation programme under grant agreement No. 687338.

Author details

Marzena Półłka, Szymon Ptak*, Łukasz Kuziora and Aneta Kuczyńska

*Address all correspondence to: sptak@sgsp.edu.pl

The Main School of Fire Service, Warsaw, Poland

References

[1] BBC. Nepal earthquakes: Devastation in maps and images [Internet]. May 15, 2015. Available from: http://www.bbc.com/news/world-asia-32479909 [Accessed: October 10, 2017]

[2] Pallardy R. (Encyclopaedia Britannica). Haiti earthquake of 2010 [Internet]. June 28, 2017. Available from: https://www.britannica.com/event/Haiti-earthquake-of-2010 [Accessed: December 6, 2017]

[3] Team Concept. Product Catalogue [Internet]. 2014. Available from: https://team-concept.pl/oferta/amfibia_argo_8x8 [Accessed: December 2, 2017]

[4] Interwent. Product Catalogue [Internet]. 2015. Available from: http://www.intervent.pl/produkty.html [Accessed: December 2, 2017]

[5] Bartłomiej Puchała. Test: Swincar Spider – Radość z Prostoty [Internet]. 2016. Available from: http://motopodprad.pl/test-swincar-spider-radosc-z-prostoty/ [Accessed: December 2, 2017]

[6] FLIR. Product Catalogue [Internet]. 2016. Available from: http://www.flir.eu/suas/content/?id=74946 [Accessed: December 2, 2017]

[7] MOBNET Consortium. Project Descritpion [Internet]. 2015 [Updated: 2017]. Available from: http://mobnet-h2020.eu/ [Accessed: December 2, 2017]

Chapter 7

New Applications of 3D SLAM on Risk Management Using Unmanned Aerial Vehicles in the Construction Industry

Alfredo Toriz Palacios,
José Maria Enrique Bedolla Cordero,
Modesto Raygoza Bello, Edgar Toriz Palacios and
Jessica L. Martínez González

Additional information is available at the end of the chapter

http://dx.doi.org/10.5772/intechopen.73325

Abstract

Risk Management is an integral part of the Corporate Governance of the Companies, whose objective is to estimate the risks related to each line of business and to make appropriate decisions regarding the adoption of preventive measures. The construction industry, due to its peculiar characteristics about occupational risks, is a sector that must pay particular attention to this issue. Unmanned aerial robots are part of a generation of new technologies, which are emerging in the attempt to develop robust and efficient algorithms capable of obtaining 3D models of structures under construction, to support the assessment of the situation in case of an eventuality, before the direct human intervention. This article proposes to develop a risk management strategy for the construction industry based on obtaining 3D models of work environments using drones, which will allow safe evaluation of risks present in construction zones.

Keywords: unmanned aerial robots, risk management, construction industry, 3D models, SLAM

1. Introduction

In most industrialized countries, the construction industry is one of the most important in terms of contribution to gross domestic product (GDP). In the United States alone, this sector generated $818.6 USD billion in the second quarter of 2017 [1], according to the Bureau of

Economic Analysis. In March 2017, the Bureau of Labor Statistics reported that 6,882,000 people were employed in the construction industry, accounting for 4% of total employment in the United States.

One of the main concerns in such a financially important industry is related to the safety issues of the employees who work in it. According to the National Census of Fatal Occupational Injuries in 2015, there were 4379 deaths of workers in private industry in 2015; of these, 937 (21.4%) belonged to the construction industry, that is, one in five [2]. In addition, according to information reported in Safety + Health, a construction worker has a 75% chance of a disabling injury and a 1-in-200 chance of a fatal injury during a 45-year career.

The U. S. Department of Labor reported that 64% of the deaths of private sector workers in the construction industry in 2015 had four causes, called Fatal four: falls, which represented 364 deaths (38.8%), blows per object with 90 deaths (9.5%), electrocution with 81 deaths (8.6%) and trapping with 67 deaths (7.2%) [1]. It is estimated that the prevention of Fatal Fours would save approximately 600 workers' lives in the United States each year. Almost all construction workers will have at least one work-related injury in their lifetime.

Technological advances in areas such as personal protective equipment, safety-conscious design, focused safety training, among others, have improved worker safety. However, even with such improvements, construction continues to be one of the most dangerous industries in the U. S. economy in terms of serious injury, lost work time, hospitalization, disability, and mortality [3].

According to [4], risk management in the construction industry consists of assessing and responding to the risk that will inevitably be associated with a project. In parallel, risk management seeks to establish mechanisms to reduce the disturbances that can occur during project action [5]. However, one of the problems is that, in many cases, the risk is analyzed once the accident has occurred, i.e., the analysis looks backwards and only helps with recommendations, probabilities and data on accidents that have occurred [6].

The above activity is very helpful in reducing accidents, but it is essential to use more robust tools when performing high-risk work as dynamic as they do in the construction sector, so it is necessary to use flexible technological tools that can interact in complex environments. One of the most important needs of companies in risk management is to reduce accidents from prevention, so it is important to promote the development of a technological-inclusive model that helps to make the process of industrial risk analysis more robust, to contribute to the prevention and reduction of hazards and accidents. Nowadays, with support of multiple options offered by technology, new forms of work can be incorporated, in which human beings can interact with novel tools, at low cost, generating spaces where it is possible to carry out their tasks minimizing risks. Thus, worker protection against occupational hazards requires organizations to evaluate models that combine technology in the design of their jobs, productivity, and employee satisfaction [7].

In recent years, there has been a growing demand for the use of robots in civil contexts [8–11] because companies and individuals have identified the advantages of using such technologies. These include the significant growth of Unmanned Aerial Vehicles (UAV), given the significant advantages of mobility and the ability to gain access to places of very difficult access. Although

http://dx.doi.org/10.5772/intechopen.73325

construction has been known as a highly complex field of application for these types of robotic systems, recent advances in this field offer great hope, as they represent a low-cost alternative for aerial surveillance in risk identification over other equipment where very robust structures are required [12].

The purpose of this research is to develop and test a UAV Technological Inclusion Model for the prevention of high-risk work in the construction industry, based on the Research, Assessment, Analysis and Selection methodology for risk management (RAAS). It also aims to incorporate into the industrial risk analysis management processes the benefits of integrating an incremental innovation that relies on 3D reconstruction to contribute to the knowledge of applications of the tools that are used in robotics.

2. Related works

Continuous monitoring of unsafe conditions and actions is essential to eliminate potential hazards and ensure safe working conditions in the construction industry. Many works have included risk management and its impact, which for Jannadi and Almishari [13] is a measure of the probability, severity, and exposure to hazards of a specific activity. Given the diversity of risks, there is no methodology to cover all the existing casuistry, nor to investigate the causes of accidents, but to anticipate them with the support of tools developed for this purpose.

Several papers show the interest of researchers in this subject. In 2007, Hallowell [14] validated a method that matches the elements of the safety program in construction processes. Rozenfeld et al. [15] developed the "Construction Work Safety Analysis" method, which can predict fluctuations in risk levels. Benjaoran and Bhokha [16] integrated the construction process through risk analysis throughout the design, planning and control phases. Rajendran [17] assessed the relative capacity of elements of a program to improve site security. Markowski et al. [18] proposed the ORA method, which estimates risk levels to colleagues (workers) through three steps: identification, assessment, and hierarchy of potential risks. Salla and Sanna [19] agreed that risk assessments and instruction in safe work practices should ensure that workers have relevant safety knowledge.

In 2004, Azcuénaga proposed a method based on four stages: Identification, Assessment, Action, and Monitoring (IAAM) [20]: 1. Identification of existing risks through activities aimed at such identification (inspections and observations). 2. Assessment or evaluation of risks, using a method that classifies them according to their criticality. 3. Action, taking corrective measures following the priority set by the evaluation, trying to eliminate the risks and, if not, reduce and control them. And 4. Follow-up of corrective measures, indicating the person responsible for their execution, their deadline, and verification of their effectiveness.

Although the tools mentioned above have managed to improve the working conditions of the construction industry, most inspection processes are carried out manually by qualified inspectors, which means that they are subjective. Robotics and computer vision can solve some of these situations, improving inspection quality by collecting different types of data, through which 3D models of working environments are generated [21].

3D reconstruction, based on images of civil infrastructure, is an emerging topic that is gaining interest in the scientific and commercial sectors of the construction industry. In the last decade, reliable computer vision-based algorithms have been made available and can now be applied to solve real-life problems in uncontrolled environments. For example, Fathia et al. [22] analyzed the state-of-the-art image-based 3D reconstruction and categorized existing algorithms according to different metrics, identifying gaps and highlighting future research topics that could contribute to the widespread adoption of this technology in the construction industry.

Seo et al. [23] categorized computer vision techniques for construction safety into three groups, according to the types of information needed to evaluate unsafe conditions and acts: object detection, object tracking, and action recognition. The results demonstrated significant research challenges include a complete understanding of the scene, variation in camera positioning tracking accuracy, and identification of action by multiple teams and workers.

The application of UAVs to project sites has also grown exponentially in recent years [24]. Today, many Architecture / Engineering / Construction and Facility Management (AEC / FM) firms and relevant service companies use these platforms to visually monitor construction and operation in buildings, bridges and other types of civil infrastructure systems. This application captures very large collections of images and videos, along with methods that process visual data in 3D models.

The implementation of UAVs on project sites has been made possible by rapid advances in detection, battery and aeronautical technologies, along with self-contained navigation methods and low-cost digital cameras equipped, which has helped make UAVs more affordable, reliable and easy to operate [25]. Although the direct application of these methods for construction monitoring and risk condition analysis has the potential to obtain efficient evaluation mechanisms, their industrial use has lagged to merely monitoring by collecting videos of the work areas.

3. UAV-based 3D environment reconstruction

The focus of the proposal carried out in this research is to obtain a model of the structure that can be studied; for this task, a tool was developed to reconstruct three-dimensional environments based on the concept of 3D SLAM. In this activity, the UAV made flights to capture different images and videos to identify risks. During the field tests, the Parrot AR Drone 2.0, was used. This UAV belongs to the micro and mini UAV category, which weighs between 100 g and 30 k, and flies at a low altitude (below 300 m) [26]. The Parrot AR 2.0 is powered by four electric motors in quadcopter configuration, has a microprocessor, a series of sensors, two 1280 $\times$ 720-pixel cameras, and an integrated Wi-Fi connector that allows it to link to personal mobile devices while receiving images and telemetry data in real time.

To make the 3D reconstruction of the environment, the site resident provided a collision-free route with objects, considering critical points that should be present in the reconstruction. The control of the UAV to follow this path was carried out following the rapidly-exploring random

http://dx.doi.org/10.5772/intechopen.73325

Figure 1. Evolution of the RRT method.

tree (RRT) methodology, presented in [27], which builds an incremental position tree in a way that rapidly reduces the expected distance to a chosen point (**Figure 1**).

To perform the RRT control, it was first necessary to establish the quadcopter motion model to identify how the vehicle's movement evolves from instant i to $i + 1$, which consists of seven state variables:

$$X_i = \left(x_i, \mathrm{y}_i, \mathrm{z}_i, \dot{x}_i, \dot{\mathrm{y}}_i, \dot{\mathrm{z}}_i, \Psi_i, \theta_i, \varphi_i, \dot{\varphi}_i\right)^{\mathrm{T}} \tag{1}$$

where $\left(x_t, \mathrm{y}_t, \mathrm{z}_t\right)$ represent the position of the quadcopter's center of mass, $\left(\dot{x}_t, \dot{\mathrm{y}}_t, \dot{\mathrm{z}}_t\right)$ the velocity in m/s, both related to the system's fixed coordinate system; in addition, the 10 variables contain the orientation (Ψ, θ, φ) of the UAV, referring to the angles of Roll, Pitch and Yaw, respectively.

To obtain the $i + 1$ status of the UAV, horizontal acceleration $\ddot{x}, \ddot{y}$ and vertical acceleration $\ddot{z}$, as well as angular accelerations $(\ddot{\Psi}, \ddot{\theta}, \ddot{\varphi})$ are derived from the current status X_i and active control inputs U_i, which give the possible end positions of the RRT method.

According to [28], horizontal acceleration is proportional to the horizontal force acting on the quadcopter. Thus, we get the following equation:

$$\begin{pmatrix} \ddot{x} \\ \ddot{y} \end{pmatrix} \equiv \mathrm{f}_{\mathrm{accelation}} - \mathrm{f}_{\mathrm{drag}} \tag{2}$$

where $\mathrm{f}_{\mathrm{accelation}}$ denotes the acceleration force on the UAV, and $\mathrm{f}_{\mathrm{drag}}$ denotes the pulling force. The acceleration force depends on the inclination angle of the UAV, while the pulling force is proportional to its horizontal velocity, which leads to the following equations:

$$\ddot{x}(X_i) = \mathrm{c}_1\left(\cos\varphi_{\mathrm{i}}\,\mathrm{sen}\,\Psi_{\mathrm{i}}\cos\theta_{\mathrm{i}} - \mathrm{sen}\,\varphi_{\mathrm{i}}\,\mathrm{sen}\,\theta_{\mathrm{i}}\right) - \mathrm{c}_2\dot{x}_{\mathrm{i}} \tag{3}$$

$$\ddot{\mathrm{y}}(X_i) = \mathrm{c}_1\left(-\mathrm{sen}\,\varphi_{\mathrm{i}}\,\mathrm{sen}\,\Psi_{\mathrm{i}}\cos\theta_{\mathrm{i}} - \cos\varphi_{\mathrm{i}}\,\mathrm{sen}\,\theta_{\mathrm{i}}\right) - \mathrm{c}_2\dot{y}_{\mathrm{i}} \tag{4}$$

Proportionality coefficients c_1 and c_2 were empirically determined from 30 flight tests. The control command $U = \left(\widehat{\Psi}, \widehat{\theta}, \widehat{\varphi}, \widehat{z}\right) \in [-1, 1]$ defines the desired roll and Pitch angles, as well

as the desired Yaw angular velocity and vertical velocity as a fraction of the maximum allowed value. These parameters serve as input values for drone control. A similar model to the one used for horizontal accelerations, but this time to obtain angular speeds Roll and Pitch, as well as angular acceleration Roll and vertical acceleration, was used as follows:

$$\dot{\Psi}(X_i, U_i) = \left(c_3\widehat{\Psi}_i - c_4\Psi_i\right) \tag{5}$$

$$\dot{\theta}(X_i, U_i) = \left(c_3\widehat{\theta}_i - c_4\theta_i\right) \tag{6}$$

$$\ddot{\varphi}(X_i, U_i) = \left(c_5\widehat{\dot{\varphi}}_i - c_6\dot{\varphi}_i\right) \tag{7}$$

$$\ddot{z}(X_i, U_i) = \left(c_7\widehat{\dot{z}}_i - c_8\dot{z}_i\right) \tag{8}$$

Similarly, elements c_1, c_2, c_3 to c_8 were empirically determined from 30 flight tests. Finally, the transition from drone state i to the $i + 1$ is given by the following expression:

$$X_{i+1}^{-} = X_i + \delta_i \begin{pmatrix} x_i \\ y_i \\ z_i \\ \ddot{x}(X_i) \\ \ddot{y}(X_i) \\ \ddot{z}(X_i, U_i) \\ \dot{\Psi}(X_i, U_i) \\ \dot{\theta}(X_i, U_i) \\ \dot{\varphi}_i \\ \ddot{\varphi}_i(X_i, U_i) \end{pmatrix} \tag{9}$$

where δ_i represents the period of the control cycle.

Once the UAV's advance to the designated position is checked, the next step is to know the approximate actual location of the vehicle, as internal and external disturbances may cause the position to be only partially reached. From the preceding, it is necessary to know relevant internal information about the vehicle to carry out the 3D reconstruction task, such as height, speed, turns, stability and inertia of the UAV, which have been extensively studied and analyzed in Bristeau et al. [29]. The extraction of external information through the onboard cameras is equally important because the acquisition and processing of this information is needed to construct the 3D environment. Thus, the 3D reconstruction algorithm is initially based on predicting the position of the UAV using its odometric information. This first assumption is of vital importance since one of the leading elements for obtaining the 3D model of the environment is the camera's spatial location.

The images captured by the on-board cameras are then used through the monocular SLAM method presented by Civera [30] for more precise location of the vehicle. This algorithm is

based on the extraction of invariant points of interest within the image, located in the R^3 space, which are used by the Kalman Extended filter (a tool widely used to solve the SLAM problem), for the location of the UAV and the simultaneous construction of the map.

Thus, once the image of the environment is obtained, the Speeded-up robust features (SURF) method proposed by Bay et al. [31] is used to collect characteristic points, which is achieved by relying on integral images for convolution. In this sense, the SURF method makes use of a detector based on the Hessian matrix to determine points of interest within the image and their scale. Then, given a point $P = (x, y)$ in the image, the Hessian matrix $\eta = (P, \sigma)$ in P with scale σ is defined as:

$$\eta(P,\sigma) = \begin{bmatrix} \tau xx(P,\sigma) & \tau xy(P,\sigma) \\ \tau xy(P,\sigma) & \tau yy(P,\sigma) \end{bmatrix} \tag{10}$$

where $\tau xx(P, \sigma)$ is the convolution of the second-order derivative of the Gaussian $\frac{\partial^2}{\partial^2 x^2} g(\sigma)$ with the image I in the point P, and similarly to $\tau xy(P, \sigma)$ and $\tau yy(P, \sigma)$. The Hessian determinant indicates the scale of the point of interest, and is calculated through approximations to the second-order derivatives of Gaussian ($\Psi xx, \Psi xy, \Psi yy$) with the following formula:

$$Det(\eta aprox) = \Psi xx\Psi yy - (0.9\Psi xy)^2 \tag{11}$$

with the intention of obtaining points of interest that could be identified in consecutive images under different viewing conditions.

Once the scale is obtained, the next step of the SURF method is to apply a descriptor, to obtain points of interest identifiable in consecutive images under different viewing conditions, so the descriptor must be distinctive and, at the same time, robust to noise, detection errors, and geometric and photometric deformations. For this purpose, it was necessary to calculate the orientation of the point of interest, which is based on the sum of the "Haar wavelet" for directions (x, y) in a circular region of radius 6 s, where s is the scale of the point of interest. Once the directions have been calculated for all neighbors, the dominant orientation is estimated by calculating the sum of all the results within a window that covers a $\pi/3$ angle. The purpose of this step is to construct a square region centered around the point of interest to describe the distribution of the intensity of the content. The result of applying the SURF method is in **Figure 2**.

Although the SURF method provides an efficient method for identifying characteristic points in an image, the result of its application is limited to the R^2 space. Thus, the images obtained with the identification of such points were treated using the reverse depth representation method for the monocular SLAM problem, proposed by Civera [30]. This representation implies that, from a series of fixed sequence images of an environment obtained from a moving camera, it is possible to get a three-dimensional description of the characteristic points contained in the images and use them to achieve a three-dimensional model of the scene.

Thus, for each key point contained in the images, the inverse depth method will eliminate the uncertainty of the depth of each of them, taking their information from the R^2 space to the R^3

Figure 2. Result of the application of the SURF method in the image captured by the UAV.

space. Then, each point i in the three-dimensional space is defined by a 6-dimensional state vector.

$$\mathrm{y}_i = \begin{pmatrix} x_i & y_i & z_i & \theta_i & \varphi_i & p_i \end{pmatrix}^{\mathrm{T}} \tag{12}$$

which encodes the beam from the position of the camera from which the characteristic was first observed, being $(x_i, y_i, z_i)$the optical center of the camera, and $(\theta_i, \varphi_i)$the azimuth and elevation coded in the global reference system of the scene. The depth of the feature along the beam d_i is obtained through its inverse $p_i = 1/d_i$ (**Figure 3**).

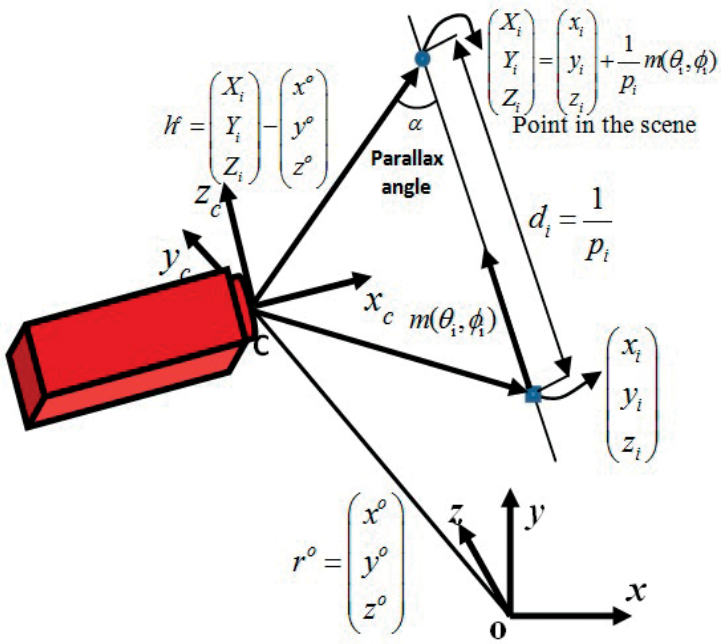

Figure 3. Characteristics parametrization. Source: Own elaboration.

http://dx.doi.org/10.5772/intechopen.73325

The vector obtained is then used to model a 3D point in terms of XYZ Euclidean coordinates as follows:

$$\mathrm{x_i} = \begin{pmatrix} X_i \\ Y_i \\ Z_i \end{pmatrix} = \begin{pmatrix} x_i \\ y_i \\ z_i \end{pmatrix} + \frac{1}{p_i}\mathrm{m}(\theta_\mathrm{i}, \varphi_\mathrm{i}) \tag{13}$$

where $m = \left(\cos\varphi_i sen\theta_i - sen\varphi_i \cos\varphi_i \cos\theta_i\right)$ represents a unitary directional vector.

Once the characteristic points of the scene have been obtained in the R^3 space, the environment is 3D–reconstructed using them in combination with Kalman's extended filter.

The first step for the EKF to be executed is the creation of the covariance matrix $P_{,}$ which is formed by the covariance matrices between the camera and the characteristics of the environment, and the state vector λ, which will contain the position of the camera and the estimation of the scene's characteristic points.

The matrix P has the following form:

$$P = \begin{bmatrix} Pxx & Pxy_1 & Pxy_2 & \cdots \\ Py_1x & Py_1y_1 & Py_1y_2 & \cdots \\ Py_2x & Py_2y_1 & Py_2y_2 & \cdots \\ \vdots & \vdots & \vdots & \ddots \end{bmatrix} \tag{14}$$

And the state vector λ has the following form:

$$\lambda = \begin{pmatrix} x_v^T & y_1^T & y_2^T & y_3^T & \ldots & y_n^T \end{pmatrix}^\mathrm{T} \tag{15}$$

where y_i is the three-dimensional state vector of characteristic i:

$$\mathrm{y}_i = \begin{pmatrix} X_i & Y_i & Z_i \end{pmatrix}^\mathrm{T} \tag{16}$$

and where x_v is the camera's state vector, consisting of a position vector r^o, an orientation quaternion q^{CO} representing the C orientation of the robot's camera with respect to the global reference system O, a linear velocity vector v^o relative to the global reference system, and an angular velocity vector ω^C relative to the UAV's camera reference system, the latter obtained from the odometric system itself.

Next, the EKF algorithm [32] shown in **Figure 4** is executed for each image captured by the UAV as follows:

The EKF Algorithm steps are:

1. Stage of prediction: The filter updates the position and speed of the UAV from the odometric data reported by it.

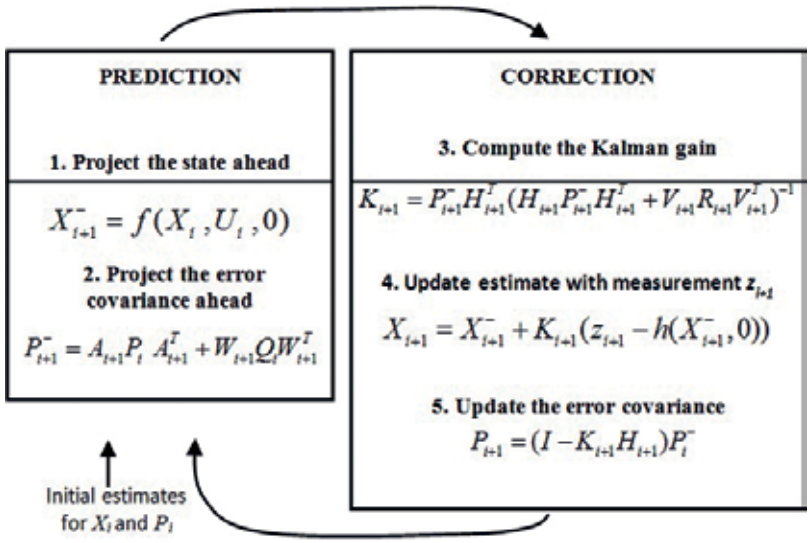

Figure 4. EKF Algorithm. Source: Adapted from [32].

2. Data association: It consists of aligning the characteristics that are being observed in step *k* with those that have been stored on the map. It is necessary to emphasize the importance of the right association between the characteristics for a consistent construction of the map, as any false association could invalidate the entire process. Thus, the joint compatibility data association method (JCBB), proposed by Neira and Tardos [33], was used to perform this stage. This algorithm performs a test to determine the individual compatibility between an observation (zi) and a characteristic obtained from the map, and a selection criterion to decide which are the best associations among the set of compatible associations.

3. Correction stage, in which the gap between the measurement and its estimation is known and the positions of the observed characteristics and the UAV are corrected, reducing the uncertainty between them (**Figure 5**).

Finally, with the completion of the EKF, the update of the environment map must be done by adding the observed localized characteristics that were not part of it and that will serve in each step of the process for the localization process.

Considering that the creation of the 3D map aims to present a complete vision that can be analyzed by an external agent, an extra functionality is added to the reconstruction, in which the localized positions of the UAV will be used to obtain a cloud of points that represents the 3D environment. To this purpose, each image obtained is treated to obtain the edges of the objects present in them and, using two consecutive pictures, these aligned edges are positioned on the map using the concept of stereo vision. In the stereo vision the position of the cameras in different time moments is well known, and from a triangulation of points, these points can be situated in the space R^3 to obtain the detailed map (**Figure 6**).

http://dx.doi.org/10.5772/intechopen.73325

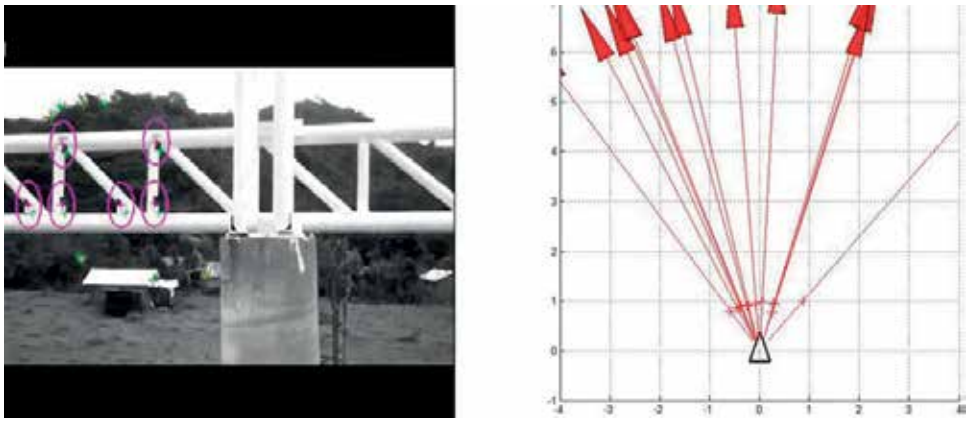

Figure 5. Evolution of the EKF algorithm with SURF points. Source: Own elaboration.

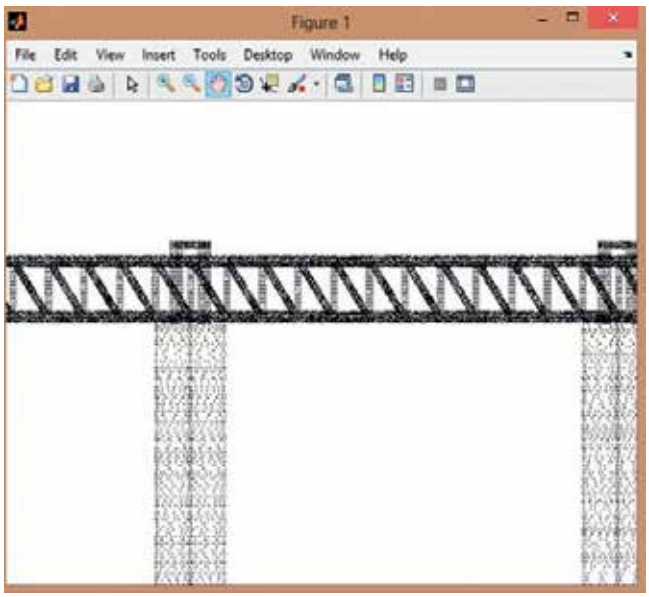

Figure 6. Point cloud of the scene. Source: Own elaboration.

After having carried out all the 3D reconstruction design, the work of collecting samples by UAV reconnaissance flight started in the second week of January 2015, and carried out for 3 weeks, excluding Sundays. Days not suitable for the test (rain, strong winds-over 15 km/h, and extreme fogs) were also excluded. Three schedules were established (7:00, 11:00 and 15:00 h) for collecting images and videos.

4. Industrial risk identification model based on unmanned aerial vehicles

Once obtained the 3D environment reconstruction tool shown in section 3, the next step was to develop an analysis methodology that could have the 3D environment and data collected by the UAV at its center. Thus, the Industrial Risk Identification Model based on Unmanned Air Vehicles (IRIMUAV) [34] presented in this section, aims to help identify and recognize risks using a UAV during industrial accident prevention work, in addition to generating technological advantages in industrial safety.

IRIMUAV was designed to be developed through nine steps grouped into four stages (planning, technological innovation UAV, use of ICT and results) based on the PHVA improvement cycle (also known as Deming cycle). The nine steps are: work program, definition of the area to be inspected, design of the inspection route, establishing critical points, reconnaissance flight, image and video capture, 3D reconstruction of the scene, risk zone analysis, risk log and final risk report (**Figure 7**).

4.1. Planning stage (P)

Step 1. Work schedule. In this level, the personnel in charge of the construction site (the technical safety supervisor or labor resident), must have very clear the working plan or program to be executed, together with the specific activities, either on paper or in a digital format.

Step 2. Definition of the area to be inspected. The site manager, together with his work team, based on the experience and technical capacity of all, and historical information on risks or accidents, will be responsible for defining the area to be observed to identify industrial risks.

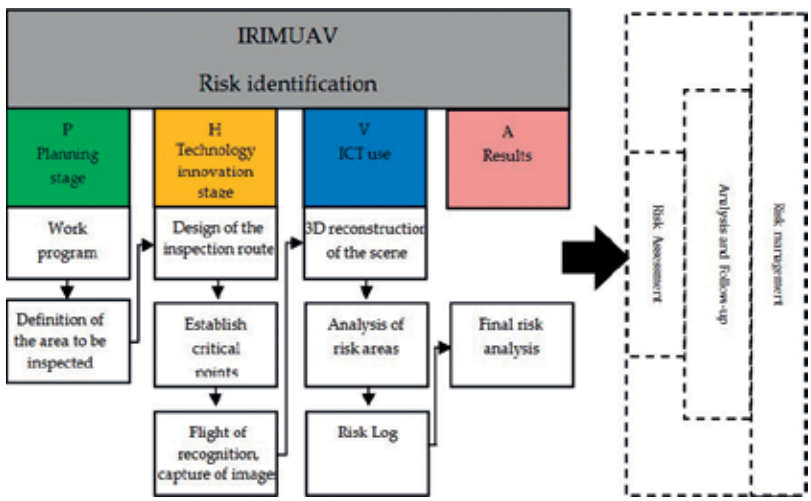

Figure 7. Industrial risk identification model based on unmanned aerial vehicles (IRIMUAV). Source: Adapted from [34].

http://dx.doi.org/10.5772/intechopen.73325

4.2. Technology innovation stage UAV (H)

Step 3. Inspection path design. Once defined the work area to be inspected, called an experimental observation unit, the project manager establishes the list of work that is pending and determines the path or paths of inspection and monitoring to be carried out by the UAV, that is, the places where the UAV must transit. The path design can be done by just creating a flight map.

Step 4. Establishment of critical points. To perform this step, the construction manager must inform the personnel trained to operate the UAV, through the flight map, which are the marked points or places where the UAV should be positioned and take images and video, to identify possible dangers. It is highly probable and recommended that the person in charge of the work be the person trained to operate the UAV.

Step 5. Reconnaissance flight, image and video capture. In this step, the UAV operator will proceed to turn on and pilot the UAV through the designated area and guide it along the inspection pathway, allowing the UAV to obtain images and video at the critical points established in step 4. It is important to keep in mind that during take-off and flight control of the UAV, the following parameters must be specified: wind speed, altitude limit, speed, the height to be inspected and the maximum vertical, as well as the maximum rotation speed with maximum angle of inclination. At his point it is considered that incremental innovation has been achieved.

4.3. ICT use (V)

Step 6. Image reproduction and 3D reconstruction of the scene. Once the UAV obtained videos with front, right side, left side, back, and top views for 360° images, a 3D reconstruction of the scene is obtained.

Step 7. Analysis of risk zones. For this step, the critical points of risk must be analyzed in the images, videos and 3D scene obtained to identify the existing risks.

Step 8. Risk log. It will be necessary to record all the risks identified in step 7 in a risk log, which can be designed in a spreadsheet such as Excel or in physical form.

4.4. Results (A)

Step 9. Final risk report. Once the risk or risks have been recorded, it will be imperative to fill out a risk identification report sheet or format, which will be an essential input of information as the steps of the risk management procedure are performed, especially when there is a need to assess, analyze and monitor risks. Also, the risk identification information obtained will serve to strengthen the planning stage in a new cycle of application of the IRIMUAV model, specifically step 2. The final risk report ensures the management focus of the model.

Once the final risk report is obtained, the magnitude of the risks and the analysis and monitoring of hazards must be performed, to develop risk management and decision making. The last step of the IRIMUAV, the final risk report, provides valuable information for risk

assessment. It also makes it possible to achieve a better analysis and monitoring of risks, since it will help to guarantee a better estimation of risks and their probability of occurrence (whether low, medium or high), as well as supporting a more reliable decision making regarding the consequences of determining the level of exposure to the hazard (light, medium or extreme). It is also important to proceed with the steps of risk analysis, for which it is advisable to use some technological tool available in the market, such as SE Risk (riesgo)—Gestión de riesgos y controles, ORCA Risk Management (gestión de riesgos), o GCI Risk (riesgo) [35].

5. Results

To validate this proposal, it was applied to a Mexican construction company located in the central area of Veracruz, Mexico. An action plan was drawn up to implement the IRIMUAV model (**Table 1**), performed from November 2016 to May 2017.

For the development of the implementation of the IRIMUAV, at each point of the procedure, the observation and recording were performed and included in a list that considered the tasks involved in each activity. The list included the following information: the personnel that executes the activity, people involved, frequency and time of exposure to risks, and the

Application area	Plan elements	Needed documents	Responsible	Programming	Place
Administration	Sensitization	Sensitization program	Staff	October	Training room
	Inducción	Induction program	Staff	October	Training room
	Training	Training program	Staff	October	Training room
	Policy and normativity	Official Mexican NORM NOM-031-STPS-2011	Safety coordinator	November	Company
	Work teams organization	Responsibility matrix	Staff	November	Safety department
	Evaluation of the UAV acquisition	Comparing table	Staff	November	
	Manual writing and training to use the acquired UAV	UAV acquisition			
Process	Manuals	Staff		Company	
Control	Model implementation	IRIMUAV (model)	Staff, safety coordinator	November–March	Safety department
	Allocation area for beam installation				

Source: Own elaboration.

Table 1. Action plan to implement the MIRIUAV model.

http://dx.doi.org/10.5772/intechopen.73325

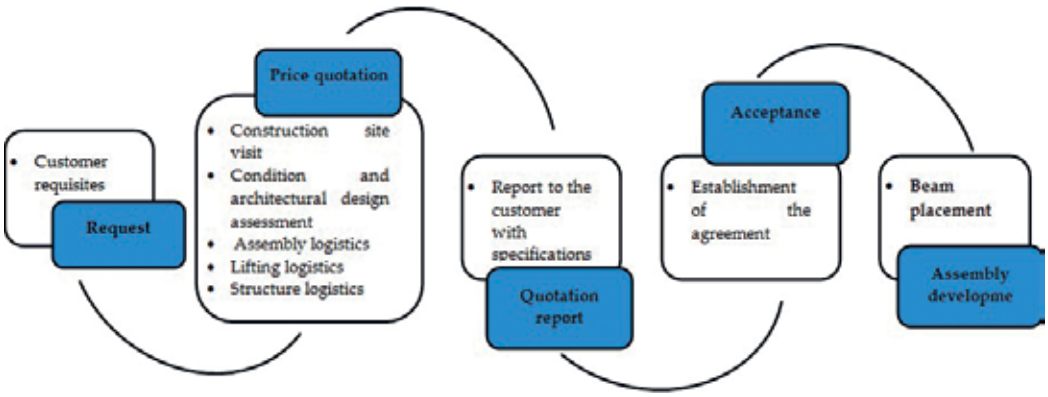

Figure 8. Beam placement process. Source: Own elaboration.

equipment, tools, and machinery to be used. The design of the inspection path was based on the company's specialization, i.e., the most frequent maneuvers, with emphasis on the assembly of steel and concrete bridge straps. The procedure for carrying out this maneuver is shown in **Figure 8**.

Subsequently, to operate the UAV through the flight map, the marked points or places where the UAV should be positioned and take images and video were defined to identify possible dangers. Starting from the bridge construction project, the activity of bridge beam assembly was selected as the inspection and follow-up route for the UAV. The first step was to carry out reconnaissance flights. **Figure 9** shows the flight made by the UAV, to take images to detect critical points for the placement of beams, taking into account the hydro meteorological and topographical conditions, architectural design and materials used for the assembly of beams on each bridge.

The UAV collected images and video footage of the beam-mounting activity. Based on this information, a 3D reconstruction of the scene was generated (**Figure 6**) and from it the present risks were analyzed, obtaining the logbook shown in **Table 2**.

Figure 9. Reconnaissance flight on the right side of Tower 3. Source: Own elaboration.

Day	Number of risks identified by the resident	Number of risks identified through the UAV
1	15	20
2	10	17
3	13	20
4	13	16
5	11	17
6	11	18
7	14	17
8	11	16
9	13	21
10	12	16
11	15	18
12	15	20
	153	216

Source: Own elaboration.

Table 2. Number of risks identified by resident/number of risks identified by UAV.

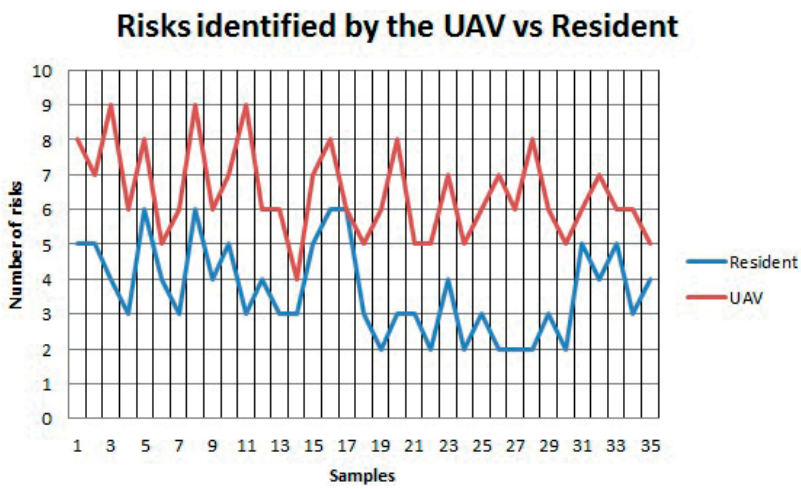

Figure 10. Comparison of risks identified by resident vs. UAV. Source: Own elaboration.

Statistical analysis was then carried out, which consisted of observing, with the aid of simple random sampling, the behavior of variable Y (25 possible accident risks). The risks were assessed using two different methods: 1) through direct observation and experience of the construction site resident and 2) through the images and videos captured by the UAV (see **Figure 10**). With the help of the UAV, 216 risks were identified. Compared to the 153 risks detected by the site resident's experience, with the help of the UAV, 41.17% more risks were identified during the observation period (**Figure 10**).

Hypothesis testing	
H_0	≤3.648649 (Approximately 4 risks)
H_1	>3.648649 (Greater than 4 risks)
Criterion	$Z = \left\lvert \frac{\bar{y}-\mu}{s/\sqrt{n}} \right\rvert$ $Z = 7.94139$
Calculation result	

Source: Own elaboration.

Table 3. Statistical results of hypothesis testing.

A hypothesis test was then carried out to establish that it is possible to identify a higher number of risks with the help of the UAV compared to the traditional method used by the site resident, using the SPSS version 9 software for Windows. The data were first observed to follow a normal distribution, and a common test was performed on large samples [36]. The mean and standard deviation parameters were calculated using the data in **Table 1**. As a known population, data taken from the construction site resident were included, and the mean (μ = 3.648649) and standard deviation (σ = 1.441725) were calculated and the sample mean was estimated based on data obtained by the UAV ($\bar{y}$ = 5.573166) and as standard deviation (s = 1.454058). The significance level was set to 0.05 with a value of Z = 1.96 (see **Table 3**).

As can be seen from the data in **Table 2**, the value calculated for Z is greater than the value of Z in tables, so the null hypothesis established for the test performed is rejected, and it is concluded that the risks identified by UAV are higher than those determined by the traditional method. Besides, for the specific study, it is concluded that on average approximately six risks were identified with the help of UAV compared to the four average risks using the traditional method.

With the application of hypothesis testing and during the development of the Delphi technique, the experts observed favorable results during the identification and risk recognition phase. The procedure increases the value of the model since it includes a more robust and structured logical-deductive process by covering more observation points and information (images, videos and 3D reconstruction). The expert opinion also strengthens the proposal to include the UAV use for high-risk prevention.

6. Conclusions

UAVs as an incremental innovation for the IRIMUAV model proved to be a combination that produced a tool that contributes to strengthening the safety risk management process in the construction industry. The model also showed characteristics that may support a more effective identification and recognition of technical risks, to help prevent and reduce accidents at work, as well as reducing the costs of accidents.

Because of its technological capability, the information that can be collected by UAVs reveals many details imperceptible at plain sight. The evolution of the potential that allows the development of artifacts, procedures, and norms that facilitate the interaction between man and the environment, assuring the adaptation and satisfaction of needs through the application of systematic methods with scientific foundations, results in the rise of technology [37].

In addition to innovation, integrating technology is fundamental, as it has become a factor of organizational growth and increased competitive advantage, somehow minimizing the risk of failure [38]. The risk assessment procedures cited in this document have an added value for risk and cost reduction, through the design of a technological inclusion model using UAVs. The use of UAVs provides greater versatility and extensive use during the stages of the process life cycle since it reduces the limitations of traditional methods. With the capture of images, videos and 3D recognition with the UAVs, it is possible to make more exhaustive studies. The use of UAVs also reduces the subjectivity of traditional studies, actively supporting the analyst, broadening human experience, and improving the level of confidence by providing more non-subjective information on the identified risks [24].

Today we live in a society of global risk, which coexists with global risk scenarios such as ecological risks, financial risks, and terrorist risks, to name a few, where it is necessary to generate brave actions or predictability models [39]. In other words, our society should not work so much for the calculation or prevention of risks, but instead, devote to acting to anticipate future dangers.

The great diversity of technology within the analysis of labor risks allows the industry to face challenges to carry out preventive practices without focusing on economic issues, but on the reduction of the frequency of accidents, and on the seriousness of the damage as a function of the workers' well-being [40]. The present study showed that technology intervention, specifically the use of UAVs employing surveillance robotics to help this great need, is beneficial. The broad scope and visibility of UAVs facilitate work on irregular and uneven terrain, not to mention the low-cost alternative for aerial surveillance in risk identification aspects over other equipment, where very robust structures are required.

The experience gained shows that, with adequate risk management based on correct identification, the number of accidents tends to decrease in line with the magnitude of their consequences. In that sense, this work helps to identify the decisive factors in risk development, locate the central actors and fields of action or points of convergence where the future is built day by day. This research could, therefore, have a positive impact on the development of the emerging technology called security robotics using UAV. Also, the study initially identifies aspects related to UAVs, their environment and mode of use as part of service robotics. It also provides a framework for possible development within the analysis of labor risks and the opportunity to implement as a technological strategy the adoption of new technologies, providing incremental technological innovation, specifically for the process of risk analysis within industrial safety, particularly in construction.

Author details

Alfredo Toriz Palacios[1]*, José Maria Enrique Bedolla Cordero[1], Modesto Raygoza Bello[2], Edgar Toriz Palacios[1] and Jessica L. Martínez González[2]

*Address all correspondence to: alfredo.toriz@upaep.mx

1 Popular Autonomous University of the State of Puebla, Puebla, México

2 Technological Institute of Orizaba, Veracruz, México

References

[1] Gross Domestic Product (GDP) by Industry Data [Internet]. 1999. Available from: https://www.bea.gov/industry/gdpbyind_data.htm [Accessed: 2017-10-12]

[2] Census of Fatal Occupational Injuries Summary [Internet]. 2015. Available from: https://www.osha.gov/oshstats/commonstats.html [Accessed: 2017-10-17]

[3] Frenkel M, Hommel U, Rudolf M, editors. Risk Management: Challenge and Opportunity. 1st ed. Springer; 2005. p. 838. DOI: 10.1007/b138437

[4] Simu K. Risk management in small construction projects [thesis]. Luleå Sweden: Department of Civil and Environmental Engineering, Lulea. LTU; 2006

[5] Skorupka D. Identification and initial risk assessment of construction projects in Poland. Journal of Management in Engineering. 2008;**24**(3):120-127. DOI: 10.1061/(ASCE)0742-597X(2008)24:3(120)

[6] Hopkin P. The Institute of Risk Management. Fundamentals of Risk Management: Understanding, Evaluating and Implementing Effective Risk Management. 4th ed. London, United Kingdom: Kogan Page; 2017. p. 488. ISBN: 978 0 7494 7961 9

[7] Schatsky D, Schwartz J. Redesigning work in an era of cognitive technologies. Deloitte Review. 2015;**17**

[8] Senthil M, Rajamani V, Kanagachidambaresan GR. An intelligent surface ROBOT for civil construction application. In: Proceedings of International Conference on Control, Communication and Power Engineering (CCPE'13); 26–27 April 2013; Bangalore, India; Elsevier; 2013

[9] Dautenhahn K. Socially intelligent robots: Dimensions of human–robot interaction. Philosophical Transactions of the Royal Society, B: Biological Sciences. 2007;**362**(1480):679-704. DOI: 10.1098/rstb.2006.2004

[10] Truong X, Yoong VN, Ngo T. Socially aware robot navigation system in human interactive environments. Intelligent Service Robotics. 2017;**10**(4):287-295. DOI: 10.1007/s11370-017-0232-y

[11] Krishnan RH, Pugazhenthi S. Mobility assistive devices and self-transfer robotic systems for elderly, a review. Intelligent Service Robotics. 2014;**7**(1):37-49. DOI: 10.1007/s11370-013-0142-6

[12] Cavalcanti A, Shirinzadeh B, Freitas J, Hogg T. Nanorobot architecture for medical target identification. Nanotechnology. 2008;**19**:1-15. DOI: 10.1088/0957-4484/19/01/015103

[13] Jannadi OA, Almishari S. Evaluación de Riesgos en la construcción. Diario de Ingeniería y Gestión. 2003;**129**(5):500.129

[14] Hallowell M R, Gambatese J. A formal model for construction safety risk management. In: The Construction and Building Research Conference of the Royal Institution of Chartered Surveyors (COBRA'07); 6–7 September 2007; Atlanta. pp. 1-15

[15] Rozenfeld O, Sacks R, Rosenfeld Y, Baum H. Construction job safety analysis. Safety Science. 2010;**48**:491-498. DOI: 10.1016/j.ssci.2009.12.017

[16] Benjaoran V, Bhokha S. Un integrados de gestión de seguridad con gestión de la construcción mediante el modelo 4D CAD. Ciencia de seguridad. 2010;**48**:395-403

[17] Rajendran S. Sustainable construction safety and health rating system [thesis]. Oregon: Oregon State University; 2006

[18] Markowski A, Mannan BA, Bigoszewska A. Fuzzy logic for process safety analysis. Journal of Loss Prevention in the Process Industries. 2009;**22**:695-702. DOI: 10.1016/j.jlp.2008.11.011

[19] Salla L, Sanna N. Occupational risks in industrial maintenance. Journal of Quality in Maintenance Engineering. 2008;**14**:194-204. DOI: 10.1108/13552510810877683

[20] Azcuénaga LM. Guía para la implementación de un sistema de prevención de riesgos laborales. 3rd ed. Fundación CONFEMETAL; 2004. p. 158. ISBN: 8496169472

[21] Pătrăucean V, Armeni I, Nahangi M, Yeung J, Brilakis I, Haas C. State of research in automatic as-built modeling. Advanced Engineering Informatics. 2015;**29**(2):162-171. DOI: 10.1016/j.aei.2015.01.001

[22] Fathia H, Dai F, Lourakis M. Automated as-built 3D reconstruction of civil infrastructure using computer vision: Achievements, opportunities, and challenges. Advanced Engineering Informatics. 2015;**29**(2):149-161. DOI: 10.1016/j.aei.2015.01.001

[23] Seo J, Han S, Lee H, Kim H. Computer vision techniques for construction safety and health monitoring. Advanced Engineering Informatics. 2015;**29**(2):239-251. DOI: 10.1016/j.aei.2015.01.001

[24] Appelbaum D, Nehmer A. Using drones in internal and external audits: An exploratory framework. Journal of Emerging Technologies in Accounting. 2017;**14**:99-113. DOI: 10.2308/jeta-51704

[25] Ham Y, Han K, Lin J, Golparvar-Fard M. Visual monitoring of civil infrastructure systems via camera-equipped unmanned aerial vehicles (UAVs): A review of related works. Visualization in Engineering. 2016;**4**(1):1-8. DOI: 10.1186/s40327-015-0029-z

[26] Félez EA. Drones: una nueva era de la vigilancia y de la privacidad. Ciberseguridad e infraestructuras críticas. 2013:48-57

[27] Cheng P, LaValle SM. Resolution complete rapidly-exploring random tres. In: Proceedings of the IEEE International Conference on Robotics and Automation (ICRA '02); 11–15 May 2002; Washington DC. New York: IEEE; 2002. pp. 267-272

[28] Qiao ZJ, Zhang C. Dynamic modeling and review of control methods for the quadrotor. Applied Mechanics and Materials. 2013;**373-375**:1406-1412. DOI: 10.4028/www.scientific.net/AMM.373-375.1406

[29] Bristeau PJ, Callou F, Vissiere D. The navigation and control technology inside the AR. Drone micro UAV. IFAC. 2011;**44**(1):1477-1484. DOI: 10.3182/20110828-6-IT-1002.02327

[30] Civera J, Davison A, Montiel J. Inverse depth parameterization for monocular SLAM. IEEE Transactions on Robotics. 2008;**24**:932-945. DOI: 10.1109/TRO.2008.2003276

[31] Bay H, Ess A, Tuytelaars T, Van Gool L. Speeded-up robust features (SURF). Computer Vision and Image Understanding. 2008;**110**(3):346-359. DOI: 10.1016/j.cviu.2007.09.014

[32] Mao G, Drake S, Anderson BD. Design of an extended Kalman Filter for UAV localization. In: Information, Decision and Control, (IDC '07); 12-14 February; Adelaide. New York: IEEE; 2007. pp. 224-229

[33] Neira J, Tardos J. Data association in stochastic mapping using the joint compatibility test. IEEE Transactions on Robotics and Automation. 2001;**17**(6):890-897. DOI: 10.1109/70.976019

[34] Martínez JL, Raygoza M, Toriz A, Sánchez MC, Aguirre F. Análisis de la actualización de los procesos de gestión de riesgos en el sector constructor. Journal CIM. 2017;**5**(2):38-45

[35] Dey PK, Ogunlana SO. Selection and application of risk management tools and techniques for build-operate-transfer projects. Industrial Management & Data Systems. 2004; **104**(3):334-346

[36] Mendenhall W, Scheaffer RL, Wackerly DD. Estadística Matemática con Aplicaciones. 7th ed. Madrid, España: Iberoaméricana; 2010. p. 911

[37] Ortíz N. Gestión de Tecnología e Innovación. Teoría, proceso y práctica. 1st ed. Bogotá, Colombia: Ediciones EAN; 2013. p. 404

[38] Stratopoulos TC. Emerging technology adoption and expected duration of competitive advantage. SSRN. 2016;**1**:1-20. DOI: 10.2139/ssrn.2695858

[39] Billy H, Cameron A, Roy D. La exploración de la integración de la salud y la seguridad con la construcción de la planificación previa. Ingeniería, Construcción y Gestión de Arquitectura. 2006;**13**:438-450

[40] Solís RG, Sosa AR. Gestión de riesgos de seguridad y salud en trabajos de construcción. Revista Educación en Ingeniería. 2013;**8**(16):161-170. DOI: 10.26507/rei.v8n16.304

Chapter 8

Land Use Information Quick Mapping Based on UAV Low-Altitude Remote Sensing Technology and Transfer Learning

Lu Heng, Fu Xiao, Liu Chao, Li Longguo,
Li Naiwen and Ma Lei

Additional information is available at the end of the chapter

http://dx.doi.org/10.5772/intechopen.74475

Abstract

Obtaining surface spatio-temporal data rapidly, automatically and accurately is an important issue in agriculture informationization and intellectualization. Samples obtained by conventional manual visual interpretation are difficult to adapt the demands of land resources information extraction. Low altitude remote sensing technology as a kind of emerging technology for earth observation in recent years. Based on this, spatio-temporal data mining technology was introduced, and knowledge transfer learning mechanism was used, a novel landuse information classification method based on knowledge transfer learning (KTLC) was proposed. Firstly, new image was segmented by improved mean shift algorithm to obtain image objects. Secondly, the vector boundary of the objects and former historical landuse thematic map were matched and nested, invariant objects were obtained through overlay analysis, and purification of invariant object was finished by spectral and spatial information threshold filtering. The historical features category knowledge of thematic map was transferred to the new image objects. Finally, current images classification mapping was completed based on decision tree, and landuse classification mapping results were completed by the KTLC and eCognition for landuse information mapping classification (EC). The experimental results showed that KTLC could obtain accuracies equivalent to EC, and also outperforms EC in terms of efficiency.

Keywords: low-altitude remote sensing technology, land use information, classification mapping, invariant objects acquisition, knowledge transfer learning, prior knowledge

1. Introduction

It is an issue in agricultural informatization and intellectualization to collect surface spatio-temporal data rapidly and accurately. In general, the data sources selected during agricultural information background investigations (such as basic farmland area monitoring and crop planting structure investigation) are satellite images [1–5]. However, it is hard to collect the required image data continuously in cloudy and foggy regions (such as Sichuan Basin, China) as satellite sensors are affected by weather conditions. Satellite images generally have low spatial resolution, so it is hard to identify the scattered and discontinuous small pieces of cultivated land for precise agricultural land monitoring [6, 7]. Meanwhile, land use information is still obtained and updated by means of manual interpretation currently, resulting in large workload and low efficiency. Although some scholars have proposed the automatic interpretation method, and large workload is also required for manual sampling. Therefore, it is far behind real automation. In consequence, higher requirements are placed on data source resolution and information extraction technologies. Under such circumstance, low-altitude remote sensing technology is represented by UAVs emerges. Compared with the conventional aerial photography crafts, UAVs have the following advantages: rapid take-off and landing, repetitive operations, low cost for image collection, and high spatial resolution of collected images [8–10]. As the UAV equipped with the low-altitude remote sensing technology can provide images with centimeter-level resolution at low cost, it has great application potential for basic farmland protection areas with high requirements on accuracy of land use information.

With rapid development of remote sensing technologies, the spatial resolution of collected remote sensing images is increasingly high. On the high-resolution images collected by applying low-altitude remote sensing technology, more spectral information of surface features can be obtained, and spectra difference of similar surface features become large while that of different land types is reduced. Besides, the phenomenon of same feature with different spectra and different features with same spectrum becomes more common. Due to the number of details identified on images and the complication of spectral characteristics of surface features, the accuracy of classification methods (such as maximum likelihood method, minimum distance method, and k-means clustering algorithm) based on conventional spectrum statistics characteristics is lowered [11]. Baatz and Schape [12] put forward the object-oriented remote sensing image classification method based on the characteristics of high-resolution images. With the growing popularity of images with high spatial resolution, the object-oriented analysis method is gradually replacing the conventional pixel-based analysis method [13]. With the objectification technology, spectra, shape, and texture information can be collected effectively and further integration of hierarchical relationships or semantic information can be realized. Therefore, it is more aligned with the visual image interpretation principles and process [14, 15]. A number of studies [16–18] prove that the object-oriented classification method has great potential in the improvement of automatic extraction of high-resolution remote sensing images, and that it is an ideal choice for automatic classification of high-resolution images.

Current knowledge transfer methods can be classified into four categories, that is, instance transfer, characteristics transfer, parameter transfer, and associated-knowledge transfer [19, 20]. In this chapter, by combining associated-knowledge transfer, a transfer method for surface feature

category labels (associated knowledge) based on the detection of invariant objects is designed for classified mapping of high-resolution images collected by applying the low-altitude remote sensing technology. The "category interpretation knowledge of invariant surface features" is migrated from the source domain to the target domain by obtaining invariant surface features on new images through matching and nesting of the new land use images and the previous time-phase thematic vector maps and by transferring the surface feature category label knowledge integrated in the previous time phase to the new images. It is used to set up a new characteristic—surface feature mapping relationship. In this way, this chapter proposes a method for classified mapping of land use information on high-resolution remote sensing images.

2. General information on study area and data

The study area is located in the basic farmland protection area in Lianshan Town, Guanghan City, Sichuan Province, China. The parent materials of soils in Guanghan City are either weathered bedrock matters or loose deposits. The area with soil thickness greater than 100 cm and less than 30 cm, respectively, takes up 7.43 and 1.5% of the total cultivated area. Most soils feature good arability, long arable period, and good fertilizer preservation and supply performance, providing a large arable area. However, Guanghan City has a large population with relatively less land. It covers 548 km^2 in total with a total population of 600,000. Its agricultural area is

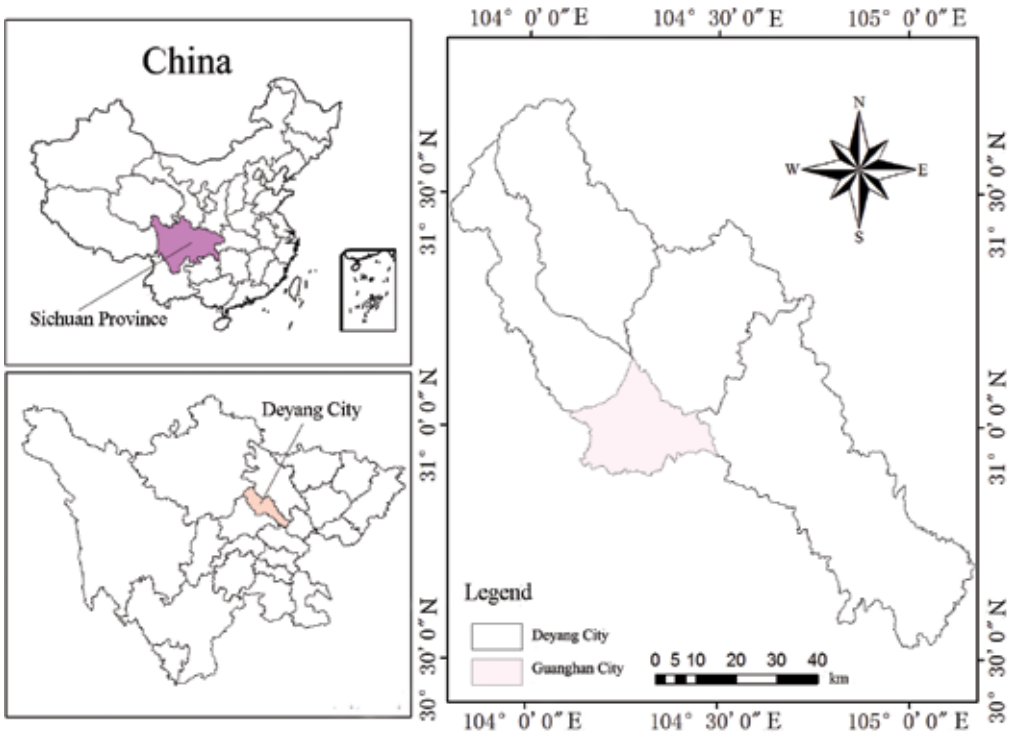

Figure 1. Location of the Guanghan City selected for the experimental purpose.

only 34,000 hm^2, with cultivated land area of 3.1 hm^2 and basic farmland protection area of 28,000 hm^2. Based on the state standards for land use classification and in combination with local conditions, the study area mainly includes six categories of land, that is, cultivated land, forest land, residential land, road, water, and other land. **Figure 1** shows the location of the study area.

Considering that the study area is gentle in terrain and therefore convenient for take-off and landing, the ejection-type fixed-wing UAV is selected for the experimental purpose. Canon EOS 5D Mark II is carried on the flying platform and the preset forward overlap and side overlap are 75 and 45%, respectively. The flight altitude is 600 m, and the camera focal length is 24.49 mm. The collected UAV images have a spatial resolution up to 0.2 m. The thematic land use maps in previous time phase were drawn in June 2014, as shown in **Figure 2a** and **b**. They were taken by UAV in July 2015. To better verify the efficiency and applicability of the method, two typical hybrid UAV images of different land types (i.e., "complex building—cultivated land" hybrid image as shown in **Figure 2c** and "forest land—cultivated land" hybrid image as shown in **Figure 2d**) are selected in this chapter.

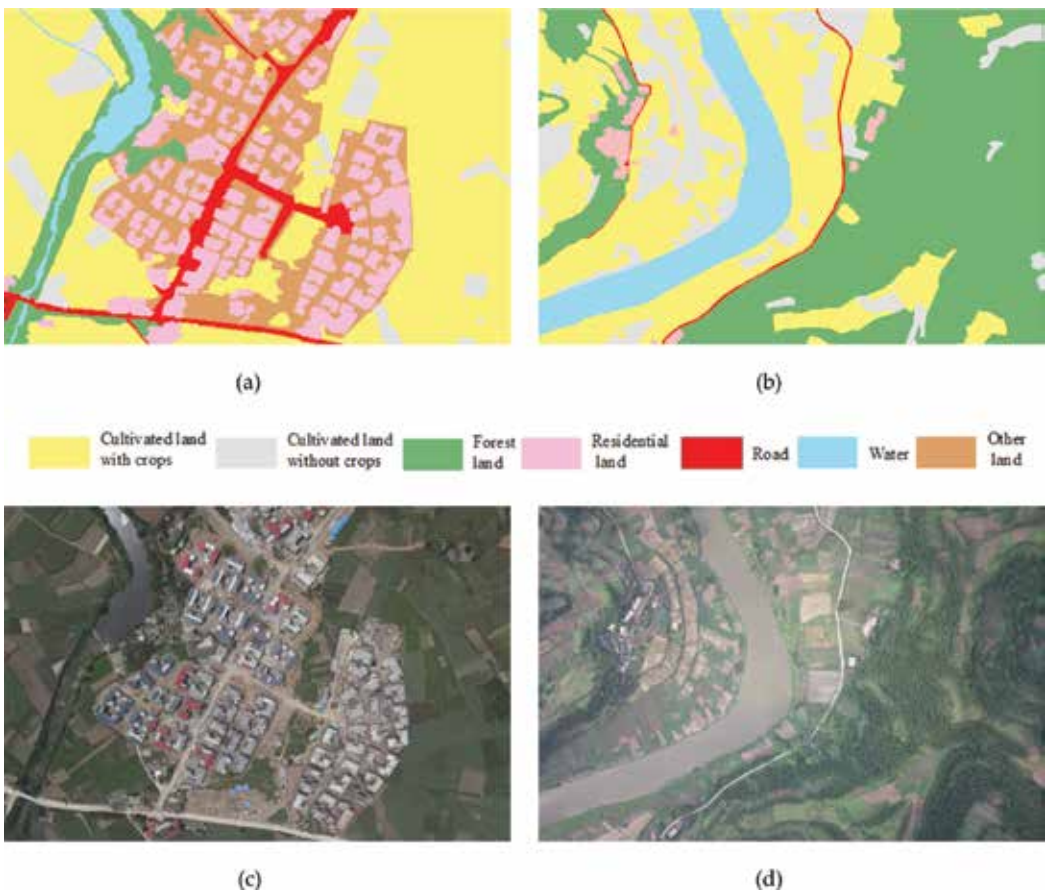

Figure 2. Preliminary thematic land use map and experimental UAV images. (a) Preliminary thematic land use map of experimental image 1. (b) Preliminary thematic land use map of experimental image 2. (c) Experimental image 1. (d) Experimental image 2.

http://dx.doi.org/10.5772/intechopen.74475

3. Working process and study method

3.1. Working process

The collected original UAV images are preprocessed, including color uniformizing, light uniformizing, and generation of orthoimages. After preprocessing, image objects are identified after multi-resolution segmentation of the to-be-classified images by applying the improved mean shift algorithm. Next, the vector boundaries of segmented objects are matched and nested with the thematic land use maps in previous time phase. Invariant objects on current images are identified through overlay analysis so as to weed out wrong invariant objects based on the spectral and spatial information thresholds. At last, the categories of invariant surface features are transferred to the current target images through transfer learning. Classification rules are established with the decision tree so as to carry out classified mapping with current images rapidly. In addition, a comparison is made with the classified mapping directly using object-oriented classification software (eCognition).

3.2. Preprocessing of image data

The digital camera on UAV is of non-metric type, so the images are subject to serious lens distortion. Therefore, distortion correction shall be carried out based on the distortion parameters of the camera [21, 22]. Meanwhile, exposure time intervals and different weather conditions in the flight course will result in chromatic aberration, so color and light uniformizing shall be carried out with the mask method. Based on the aircraft attitude parameters recorded by the flight control system, preliminary image sorting and positioning can be carried out for matching homologous points of adjacent image pairs. After matching homologous points, block adjustment can be made based on the conditions of collinearity equation. After that, the coordinates of ground control points may be incorporated to realize absolute orientation so as to obtain the corrected orthoimages. It provides high-accuracy orthoimage data for subsequent rapid updating and mapping of land use information.

3.3. Mapping method (KTLC) of land use information based on transfer learning

3.3.1. Calculation of improved mean shift segmentation and image/spectral features of objects

First of all, the preprocessed UAV images are divided into texture domain and homochromatic domain. The latter is obtained by applying the mean shift algorithm directly while the former is segmented by applying the mean shift algorithm after appropriate bandwidth is obtained based on the normalized distribution density. Next, based on the established cost function, a decision on merging of adjacent domains is made to eliminate over-segmentation domain. Refer to reference [23] for the improved mean shift segmentation algorithm selected in this chapter. Afterwards, the vector boundaries of segmented objects are matched and nested with the thematic land use maps in previous time phase, allowing them to be under the consistent spatial reference conditions. Invariant objects are further identified on the current images through overlay analysis. After image segmentation, object features have to be calculated so as to ensure the smooth progress of the subsequent classification work. In this chapter, 18 features listed in **Table 1** are calculated based on the spectral, shape, and textural features.

Spectral features			Shape features			Textural features		
Description	**Spectrum or space**	**Interpretation**	**Description**	**Spectrum or space**	**Interpretation**	**Description**	**Spectrum or space**	**Interpretation**
R_Mean	Spectrum	Mean value of red spectral band	L/W	Space	Length-width ratio	GLCM_H	Space	Homogeneity
G_Mean	Spectrum	Mean value of green spectral band	Geo_L	Space	Object length	GLCM_E	Space	Entropy
B_Mean	Spectrum	Mean value of blue spectral band	Geo_W	Space	Object width	GLCM_C	Space	Contrast ratio
R_Dev	Spectrum	Standard deviation of red spectral band	Border_L	Space	Side length of object	GLCM_V	Space	Variance
G_Dev	Spectrum	Standard deviation of green spectral band	Compact	Space	Compactness	GLCM_D	Space	Heterogeneity
B_Dev	Spectrum	Standard deviation of blue spectral band	Num_P	Space	Number of pixels	GLCM_A	Space	Angular second moment (ASM)

Table 1. Spatial and spectral features of objects.

3.3.2. Purification of invariant object samples

It shall be noted that a mistake may be made when invariant objects on the current images are identified through overlay analysis. To this point, relevant rules shall be designed to weed out wrong invariant objects. In this chapter, invariant objects are purified based on the spectral and spatial information. Specifically, object purification is judged by calculating the distance (difference value) between the mean brightness of image elements and the center of object brightness value (mean value), that is:

$$\begin{cases} \left\| R_{x_i} - M_{\mu_i} \right\| \le 4\delta_i \\ \left\| G_{x_i} - M_{\mu_i} \right\| \le 4\delta_i \\ \left\| B_{x_i} - M_{\mu_i} \right\| \le 4\delta_i \end{cases} \tag{1}$$

where R_{x_i}, G_{x_i} and, B_{x_i}—object brightness in red, green, and blue spectral bands, respectively; M_{μ_i}—mean value of object sample brightness; δ_i—spectral standard deviation of image elements in each object.

Considering the spatial information, a wrong object can be judged by checking whether the spectral standard deviation of image elements in each object exceeds the limits.

$$\begin{cases} \delta_i \le 0.2 R_{b_{\max}} \\ \delta_i \le 0.2 G_{b_{\max}} \\ \delta_i \le 0.2 B_{b_{\max}} \end{cases} \tag{2}$$

where $R_{b_{\max}}$, $G_{b_{\max}}$ and, $B_{b_{\max}}$—the maximum image brightness in red, green, and blue spectral bands, respectively. If the selected invariant object meets both Eqs. (1) and (2), it is a reliable invariant object; otherwise, it is an unreliable invariant object and shall be weeded out.

3.3.3. Associated-knowledge transfer learning and rapid classified mapping

After collection and purification of object samples regarding current target images, the best feature combination and classification model are selected for supervised classification based on the calculated image and spectral features. There are many methods regarding feature optimization selection and classification models. To ensure simplification while considering efficiency, in this chapter, the practice regarding feature optimization selection and classification model are conducted by adopting the decision tree algorithm. Then, judgment rules are established for classification purpose so as to complete classified mapping of current images.

3.4. EC method

To verify reliability of the proposed method, classified mapping of land use information is carried out with the widely applied eCognition 8, and a comparison is made with the results obtained from the KTLC method. Image segmentation shall be conducted, and then classified mapping of the segmented image objects may be carried out. Given that the standard nearest

neighbor classification method is simple, efficient, and extensively applied, and it is adopted for classified mapping with the EC method in this chapter. Specific mapping method is as follows: first, select a sample object and carry out statistical analysis to obtain textural/spectral/shape features, information on adjacent domains, etc. for establishment of multi-dimensional feature space; second, calculate the distance between the to-be-classified object and the sample; and finally, judge which one of the to-be-classified objects are closest to a sample based on the feature distance relationship and membership function, and then incorporate such object into the corresponding category.

4. Results and analysis

4.1. Rapid classified mapping

Based on the principles in Section 2.1, spectral and spatial scale parameters are taken as 7 and 10, respectively, for the improved mean shift segmentation. The segmentation results obtained by applying the improved mean shift algorithm are shown in **Figure 3**.

The vector boundaries of segmented objects are matched and nested with the thematic land use maps obtained in June 2014. Invariant objects are identified through overlay analysis and purified based on the spectral and spatial information to weed out the wrong ones. In addition, the categories of invariant surface feature objects are transferred to the current target images through knowledge transfer learning. Finally, the image/spectral features of invariant objects are subject to optimization selection by using a decision tree. Classification rules are established for classified mapping of the land use information. **Figure 4a** and **b** shows the results of classified mapping with the KTLC method.

In the experimental process, segmentation parameter settings are as follows based on the principles in Section 2.3: segmentation scale parameter: 90; color/shape parameter: 0.5/0.5; and smoothness/compactness parameter: 0.5/0.5. **Figure 4c** and **d** shows the results of classified mapping of land use information with the EC method.

4.2. Evaluation on precision and efficiency

In general, the precision evaluation of classification results is classified into qualitative evaluation and quantitative evaluation. For qualitative evaluation, a consistence comparison between the pattern spots after classification and the actual surface feature is mainly carried out. It is strongly subjective. For quantitative evaluation, overall precision, Kappa coefficient, and the like are mainly calculated [24, 25]. Due to high spatial resolution of UAV images, verification data can be directly obtained through visual interpretation. To get more objective evaluation results, verification points are obtained with the following method in this chapter: first, draw a 20 × 20 regular grid with an area equal to the image area in the experiment; then, generate 10 random points in each grid; and finally, determine the land use type at each random verification point through visual interpretation. For experimental image 1, totally 395 valid verification points are obtained; for experimental image 2, totally 382 valid verification

http://dx.doi.org/10.5772/intechopen.74475

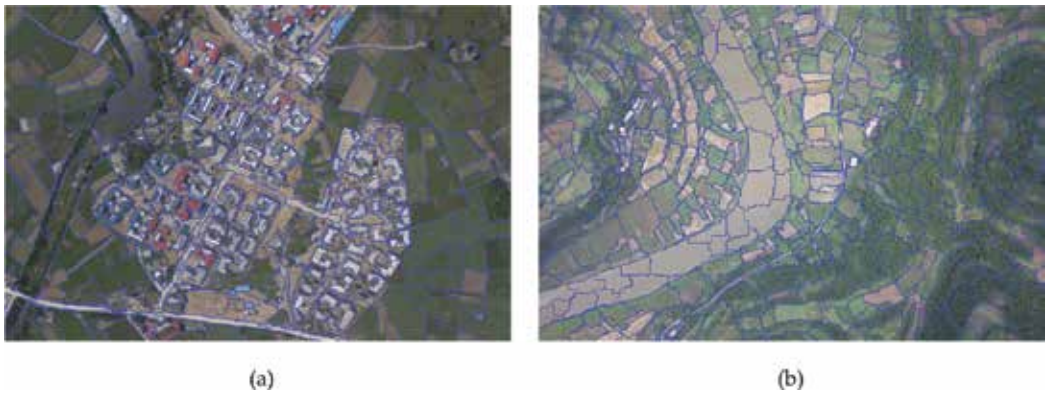

Figure 3. Segmentation results based on the improved mean shift method. (a) Segmentation result of experimental image 1. (b) Segmentation result of experimental image 2.

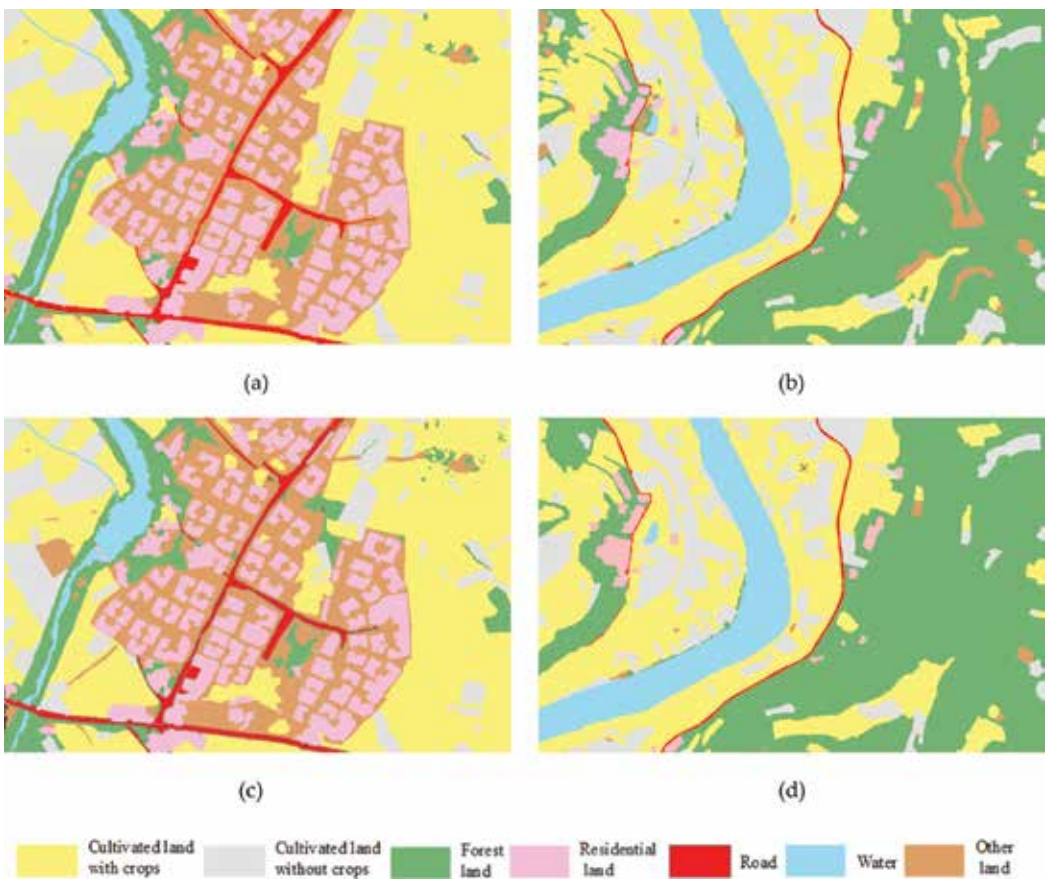

Figure 4. Results of classification mapping based on the two methods. (a) Result of experimental image 1 based on the KTLC method. (b) Result of experimental image 2 based on the KTLC method. (c) Result of experimental image 1 based on the EC method. (d) Result of experimental image 2 based on the EC method.

points are obtained. These verification points are overlapped with the classification results to judge whether the results of classified mapping are correct. Upon calculation, for experimental image 1, the overall classification precision of the KTLC method is 88.61% and the Kappa coefficient is 0.86; the overall classification precision of the EC method is 89.87% and the Kappa coefficient is 0.87. **Tables 2** and **3** show the detailed results. For experimental image 2, the overall classification precision of the KTLC method is 88.30% and the Kappa coefficient is 0.82; the overall classification precision of the EC method is 84.84% and the Kappa coefficient is 0.79. **Tables 4** and **5** show the detailed results.

Experimental image 1 is a "complex building-cultivated land" hybrid image. It can be learned from **Tables 2** and **3** that the KTLC method and the EC method have high separation precision in terms of building land and cultivated land with crops and without crops. It indicates that these three types of land are highly separable on such images with high spatial resolution. In the KTLC method, the classification precision of forest land and roads is 74.14 and 69.23%, respectively, which is lower than that of the EC method. However, its classification precision of any land types is not extremely low, and it has high classification precision in terms of cultivated land with crops, building land, and waters (98.15, 94.25 and 100%, respectively). As a result, the overall precision of the KTLC method is up to 88.61%, which is comparable with that (89.87%) of the EC method. Experimental image 2 is a "forest land—cultivated land" hybrid image. It can be learned from **Tables 4** and **5** that both the KTLC method and the EC method result in many errors in separation of forest land and cultivated land with crops due to high spectrum and texture similarity of these two types of land. The classification precision can be improved if more reliable samples are used during transfer learning. The overall precision of the KTLC method is 88.30%, which is slightly higher than that (84.84%) of the EC method, especially for forest land, cultivated land without crops, and waters (91.95, 90.77 and 100%, respectively).

	Forest land	**Cultivated land with crops**	**Cultivated land without crops**	**Road**	**Residential land**	**Other land**	**Water**
Forest land	43	12	1	0	2	0	0
Cultivated land with crops	2	106	0	0	0	0	0
Cultivated land without crop	0	4	36	0	1	2	0
Road	0	0	0	18	5	3	0
Residential land	0	0	0	2	82	3	0
Other land	2	0	5	1	0	53	0
Water	0	0	0	0	0	0	12
Producer's precision/%	91.49	86.89	85.71	85.71	91.11	86.89	100
User's precision/%	74.14	98.15	83.72	69.23	94.25	86.89	100
Overall precision = 88.61%; Kappa coefficient = 0.86							

Table 2. Confusion matrix of accuracy for experimental image 1(KTLC method).

	Forest land	Cultivated land with crops	Cultivated land without crops	Road	Residential land	Other land	Water
Forest land	46	6	0	0	0	0	0
Cultivated land with crops	3	101	0	0	0	0	0
Cultivated land without crop	0	4	30	0	0	4	0
Road	0	0	0	14	4	2	0
Residential land	1	0	1	3	90	4	0
Other land	1	0	6	0	0	63	1
Water	0	0	0	0	0	0	11
Producer's precision/%	90.20	90.99	81.08	82.35	95.74	86.30	91.67
User's precision/%	88.46	97.12	78.95	70.00	90.91	88.73	100
Overall precision = 89.87%; Kappa coefficient = 0.87							

Table 3. Confusion matrix of accuracy for experimental image 1(EC method).

Besides, after review of the error-related sample points in the results of classified mapping, it is discovered that some of the sample points are located at the boundary of two different land types (because random sample points on a 20 × 20 regular grid are adopted in the chapter), and therefore they are difficult to-be-classified. Therefore, if the errors caused by visual interpretation can be eliminated, the precision of classified mapping can be higher than that listed in **Tables 2–5**.

	Forest land	Cultivated land with crops	Cultivated land without crops	Road	Residential land	Other land	Water
Forest land	137	11	0	0	1	0	0
Cultivated land with crops	15	82	2	0	0	0	0
Cultivated land without crop	0	4	59	0	0	2	0
Road	0	0	0	11	2	0	0
Residential land	2	0	0	2	15	1	0
Other land	1	0	6	0	1	12	0
Water	0	0	0	0	0	0	16
Producer's precision/%	88.39	84.54	88.06	84.62	78.95	80.00	100
User's precision/%	91.95	82.83	90.77	84.62	75.00	60.00	100
Overall precision = 88.30%; Kappa coefficient = 0.82							

Table 4. Confusion matrix of accuracy for experimental image 2(KTLC method).

	Forest land	Cultivated land with crops	Cultivated land without crops	Road	Residential land	Other land	Water
Forest land	141	10	2	0	0	1	0
Cultivated land with crops	20	74	0	0	0	0	0
Cultivated land without crop	0	1	51	0	1	2	0
Road	0	0	0	8	4	1	0
Residential land	1	0	0	1	16	2	0
Other land	4	0	7	1	0	14	0
Water	0	0	0	0	0	0	15
Producer's precision/%	84.94	87.06	85.00	80.00	80.00	70.00	100
User's precision/%	91.56	78.72	92.73	61.54	80.00	53.85	100
Overall precision = 84.8%; Kappa coefficient = 0.79							

Table 5. Confusion matrix of accuracy for experimental image 2(EC method).

Methods	Consumption time of experimental image 1/h	Consumption time of experimental image 2/h
KTLC	0.5	0.7
EC	1.2	1.3

Table 6. Comparison of efficiency based on two methods.

For efficiency of classified mapping, with two groups of experimental data as examples, the efficiency of the KTLC method and the EC method is shown in **Table 6** under the conditions of Intel Core i7 2.4GHz,4GB memory and Windows 7 environment. It can be discovered that the KTLC method saves much time in obtaining object samples on the premise of ensuring high precision, so its efficiency is greatly improved when compared with the EC method.

5. Conclusion

In this chapter, a method for rapid classified mapping of land use information on high-resolution remote sensing images is studied in the knowledge transfer mechanism. Compared with the extensively used methods for classified mapping with the software eCognition, the KTLC method proposed in this chapter effectively combines machine learning, knowledge accumulation, and agricultural remote sensing field. In addition to providing classification results comparable with those of the EC method, the KTLC method also improves efficiency greatly, and thus improving the automation level of classified mapping of land use information. It has great application prospect to fully explore the relationship between the historical data and current data. The studies in this chapter provide new ideas for quick collection of land use information in key areas in respect of agricultural remote sensing field.

Acknowledgements

This work is supported by the National Natural Science Foundation of China (Grant no. 41701499), the Key Laboratory of Digital Mapping and Land Information Application of National Administration of Surveying, Mapping and Geoinformation of China (Grant no. DM2014SC02) and the Key Laboratory of Geo-special Information Technology, Ministry of Land and Resources of China (Grant no. KLGSIT2015-04). Finally, Lu H wants to thank, in particular, the invaluable support received from Fu X over the years.

Conflicts of interest

The authors declare no conflict of interest.

Author details

Lu Heng[1,2], Fu Xiao[3], Liu Chao[1,2], Li Longguo[1,2], Li Naiwen[1,2]* and Ma Lei[4]

*Address all correspondence to: gxqlnw@163.com

1 State Key Laboratory of Hydraulics and Mountain River Engineering, Sichuan University, Chengdu, China

2 College of Hydraulic and Hydroelectric Engineering, Sichuan University, Chengdu, China

3 Faculty of Geosciences and Environmental Engineering, Southwest Jiaotong University, Chengdu, China

4 Jiangsu Provincial Key Laboratory of Geographic Information Science and Technology, Nanjing University, Nanjing, China

References

[1] Chunjiang Z. Advances of research and application in remote sensing for agriculture. Transactions of the Chinese Society for Agricultural Machinery. 2014;**45**(12):277-293 (in Chinese)

[2] Lei M, Liang C, Wenqi H, et al. Cultivated land information extraction from high-resolution unmanned aerial vehicle imagery data. Journal of Applied Remote Sensing. 2014;**8**(1):083673

[3] Zhou S, Zongzheng L, Yuanyuan Y, et al. Status and prospect of agricultural remote sensing. Transactions of the Chinese Society for Agricultural Machinery. 2015;**46**(2):247-260 (in Chinese)

[4] Yongqi H, Weihong C, Yangjian Z, et al. Research on development of agricultural geographic information ontology. Journal of Integrative Agriculture. 2012;**11**(5):865-877

[5] Rujing W. Bottleneck of agricultural informatization development in China and the thinking of coping strategies. Bulletin of the Chinese Academy of Sciences. 2013;**28**(3):337-343 (in Chinese)

[6] Qiong H, Wenbin W, Qian S, et al. Recent progresses in research of crop patterns mapping by using remote sensing. Scientia Agricultura Sinica. 2015;**48**(10):1900-1914 (in Chinese)

[7] Qiting H, Zelin Q, Zhikang Z. Study on the crop classification and planting area estimation at land parcel scale using multi-sources satellite data. International Journal of Geographical Information Science. 2016;**18**(5):708-717 (in Chinese)

[8] Limin W, Jia L, Lingbo Y, et al. Applications of unmanned aerial vehicle images on agricultural remote sensing monitoring. Transactions of the Chinese Society of Agricultural Engineering. 2013;**29**(18):136-145 (in Chinese)

[9] Heng L, Longguo L, Yi'nan H, et al. Method of UAV image mosaic based on weighted adjustment considering terrain feature. Transactions of the Chinese Society for Agricultural Machinery. 2015;**46**(9):296-301 (in Chinese)

[10] Heng L, Xiao F, Yi'nan H, et al. Cultivated land information extraction from high resolution UAV imagery based on transfer learning. Transactions of the Chinese Society for Agricultural Machinery. 2015;**46**(12):274-279, 284 (in Chinese)

[11] Bin L, Liangpei Z. Robust autodual morphological profiles for the classification of high-resolution satellite images. IEEE Transactions on Geoscience and Remote Sensing. 2014;**52**(2):1451-1462

[12] Baatz M, Schape A. Object-oriented and multi-scale image analysis in semantic networks. In: Proceedings of the 2nd International Symposium on Operationalization of Remote Sensing; Enschede. Netherlands; 1999. pp. 16-20

[13] Hay GJ, Castilla G. An automated object-based approach for the multiscale image segmentation of forest scenes. International Journal of Applied Earth Observation and Geoinformation. 2005;**7**(4):339-359

[14] Gitas IZ, Mitri GH, Ventura G. Object-based image classification for burned area mapping of creus cape, Spain, using NOAA-AVHRR imagery. Remote Sensing of Environment. 2004;**92**(3):409-413

[15] Yunhao C, Tong F, Peijun S, et al. Classification of remote sensing image based on object oriented and class rules. Geomatics and Information Science of Wuhan University. 2006;**31**(4):316-320

[16] Benz UC, Hofmann P, Willhauck G, et al. Multi-resolution, object-oriented fuzzy analysis of remote sensing data for GIS-ready information. ISPRS Journal of Photogrammetry and Remote Sensing. 2004;**58**(3-4):239-258

[17] Renaud M, Jagannath A. Object-Based classification of Ikonos imagery for mapping large-scale vegetation communities in urban areas. Sensors. 2007;**7**(11):2860-2880

[18] Ruvimbo G, Philippe DM, Morgan DD. Object-oriented change detection for the city of Harare, Zimbabwe. Expert Systems with Applications. 2009;**36**(1):571-588

[19] Jialin P, Qiang Y. A survey on transfer learning. IEEE Transactions on Knowledge and Data Engineering. 2010;**22**(10):1345-1359

[20] Sarinnapakorn K, Kubat M. Combining subclassifiers in text categorization: A dst-based solution and a case study. IEEE Transactions on Knowledge and Data Engineering. 2007;**19**(12):1638-1651

[21] Zhizhuo W. Photogrammetric Principles. Wuhan: Wuhan University Press; 2007

[22] Yongjun Z. Geometric processing of low altitude remote sensing images captured by unmanned airship. Geomatics and Information Science of Wuhan University. 2009;**34**(3): 284-288 (in Chinese)

[23] Heng L, Chao L, Naiwen L, et al. Segmentation of high spatial resolution remote sensing images based on the improved mean shift algorithm. Journal of Mountain Science. 2015;**12**(3):671-681

[24] Shukui B, Lin D. The effect of the size of training sample on classification accuracy in object-oriented image analysis. Journal of Image and Graphics. 2010;**15**(7):1106-1111 (in Chinese)

[25] Foody GM. Status of land cover classification accuracy assessment. Remote Sensing of Environment. 2002;**80**(1):185-201

Chapter 9

Unmanned Aerial Systems for Magnetic Survey

Sergey Cherkasov and Dmitry Kapshtan

Additional information is available at the end of the chapter

http://dx.doi.org/10.5772/intechopen.73003

Abstract

Placing a magnetometer on unmanned aerial vehicle (UAV) seems to be an easy task as the sensor is rather lightweight in comparison with other geophysical sensors. But, the realization of an unmanned aeromagnetic system (UAMS) faces multiple technical complications, and, as a result, very few of many attempts to build a UAMS have succeeded. Even less projects have produced results of real magnetic survey. Different platforms (helicopters, multirotor, and fixed wing UAVs) and different kinds of magnetometers for UAMS have different pros and cons for the purpose. For the quality of magnetic survey, the most important is the issue of a platform's (UAV) magnetic noise and its influence on a magnetic sensor. Workbench experimental studies as well as results of magnetic surveys with multirotor UAMS in Leningrad region, Republic Sakha-Yakutia, and Kazakhstan demonstrate solutions facilitating state-of-the-art high-quality measurements of magnetic anomalies for geological, archeological, and other purposes.

Keywords: geophysics, magnetic survey, magnetometer, unmanned aeromagnetic system (UAMS), unmanned aerial vehicle (UAV)

1. Introduction

Magnetic survey represents one of the most effective geophysical methods for mapping the anomalies related with geological features and objects characterized by different magnetic properties. First evaluation of magnetic anomalies has been carried out in Sweden in 1640 using a compass for detecting iron ore deposits, but systematic magnetic surveys have started at the end of nineteenth—beginning of twentieth century with invention of magnetometers [1]. Both ground and aeromagnetic surveys are usually carried out in a regular pattern with fixed distances between parallel lines and points of measurements [2]. Aeromagnetic survey is usually being executed at 250–300 m height depending on aircraft characteristics and flight regulations. Unmanned aeromagnetic system (UAMS) can operate lower, starting from few meters.

This is important for geological interpretation of magnetic anomalies as the magnetic signal weakens at a distance from the source. Another advantage of UAMS is a pure economic one. A piloted aircraft is ineffective for surveys of areas, which are less than 200–300 km^2 due to high expenses on services requesting airport infrastructure and on approach from the airport to the area of survey. Unmanned aerial vehicle (UAV), especially a small one (lighter than 10 kg [3]), does not need an infrastructure and can be easily transported by car or even by operator.

The major issue of UAMS design is elimination of UAV's magnetic noise. With piloted aircraft, the problem gets resolved by one of two ways: (1) placing the magnetometer at a gondola attached to aircraft either by rope or by special bar or (2) using quite complicated systems of the aircraft's noise compensation. In traditional aeromagnetic survey, such systems contain additional magnetometers and use special algorithms facilitating results characterized by error well below 2 nT. In UAMS, such system adds sufficient weight to the load and, practically, rejects use of lightweight UAVs, which eliminates UAMS advantages over using a piloted aircraft. Thus, for UAMS, the first way is the most effective way to fight the carrier's magnetic noise. Miniaturization of equipment theoretically allows the use of compensation in UAMS using existing technologies, but it makes the system much more complex and expensive.

Each measurement in the magnetic survey, besides of the magnetic field components, should contain time and exact positioning of the magnetometer. State-of-the-art professional UAVs are usually equipped with global navigation satellite system (GNSS) and navigation system facilitating programmed flight route.

Choice of magnetometer for UAMS is also important. It should be lightweight, tolerant to the sensor's orientation, and, preferably, characterized by high frequency of measurements.

Further, we will consider solutions of these issues for fixed-wing and multirotor UAMS and will demonstrate results of magnetic surveys executed with UAMS designed on the basis of a quadcopter drone "Geoscan-401".

2. UAV as a platform for unmanned aeromagnetic system

The advisability of using UAVs to carry out aeromagnetic surveys is based on the fact that UAV-based surveys are more cost effective, and their results are comparable with those of conventional aeromagnetic surveying with the use of manned aircraft. The greater the takeoff weight of a UAV is, the more difficult and expensive its development is, and the lower its reliability and operational safety are [4]. Lightweight UAVs need no airfield; they are characterized by low energy consumption. The main problems to be solved are (1) the development of a magnetic sensor to meet a number of requirements and (2) deviation minimization [5]. The requirements for magnetic-field sensors are related to the speed of a UAV (the measurement rate should be more than 10 Hz at a speed of 60 km/h, which corresponds to a 2-m spacing between measurements) and to payload restrictions. For short-range (from 10 to 120 km) lightweight UAVs [4], the payload weight must not exceed 2 kg, which means additional requirements for aeromagnetometers.

Choice of UAV type (fixed-wing, helicopter, and multirotor) for UAMS should be made on the basis of tasks to be resolved. For magnetic survey of large areas (over 150–200 km^2) with

relatively flat surface, fixed-wing UAV would be the best option because of higher flight speed. For mountains, maneuverability of the UAV is more important, so helicopter and multirotor UAVs will be the favorites for mountain territories. Further, we will consider fixed-wing and multirotor UAVs as possible platforms for UAMS. The helicopters are excluded from consideration, as they are more expensive in operation and, at the same time, do not have clear advantages in comparison with multirotor UAVs.

2.1. Fixed-wing UAV

Typical magnetic signature of a fixed-wing lightweight UAV can be seen in **Figure 1** [5].

The magnetic noise induced by UAV "Geoscan-201" components has been measured using special non-magnetic stand 120 × 270 cm (**Figure 2**) and atomic scalar magnetometers MMPOS-1 (Russia) and Geometrics G-858 (Canada). To remove the background magnetic field, the measurements on the upper level of the stand have been initially executed without UAV by grid 10 × 10 cm. The amplitude of background magnetic anomalies of the stand is below 1 nT/m.

As far as use of gondola for distancing magnetic sensor from the UAV is rather impossible for such a lightweight aircraft as "Geoscan-201", the best option for the sensor placement is the end of wing, where magnetic influence of the aircraft ranges from −4 to +4 nT. Difference between ΔTa measured at the ends of left and right wings varies for different regimes of the engine and servo operation from 7 to 19 nT, which is much more than acceptable for the high-quality magnetic survey [5].

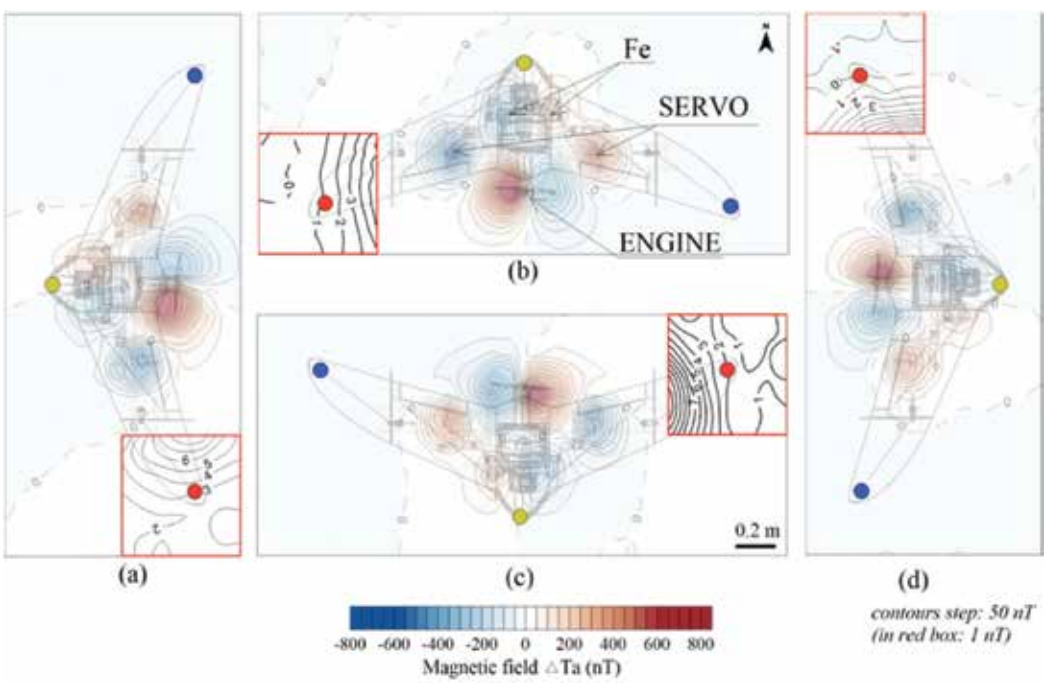

Figure 1. Magnetic signature ΔTa of "Geoscan-201" for its different orientation at the Earth's magnetic field: (a) west; (b) north; (c) south; and (d) east.

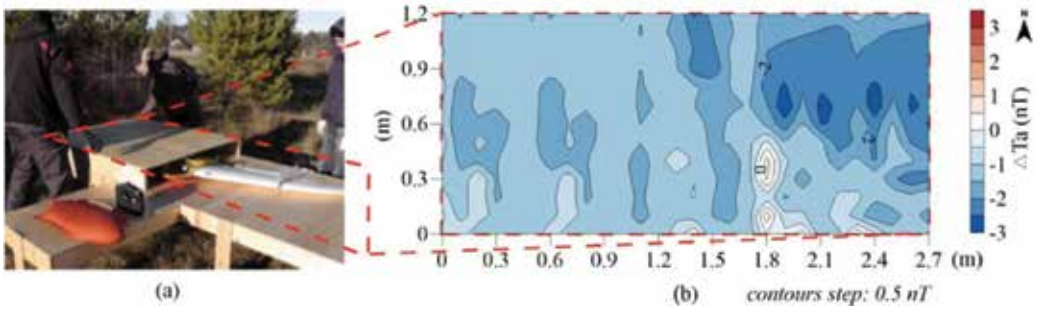

Figure 2. "Geoscan-201" magnetic noise measurement (a) and background magnetic field (b).

From **Figure 1**, it is absolutely clear that, for a lightweight UAV:

- major sources of magnetic noise are electric engine and servos producing anomalies with amplitude of 600–700 nT;
- the most appropriate location of magnetic sensors is at the ends of wings, and, in that case, the servos should be placed in the UAV's main body instead of wings.

Another obvious conclusion relates with the UAV's engine type. Replacement of an electric engine with combustion one in accordance with the results of mathematical modeling makes a horizontal gradient of the magnetic field at the end of a wing three to four times lower. However, the combustion engine fitting the task weighs about 700 g versus 284 g of electro engine. This, along with the additional weight of a magnetic sensor (up to 200 g) at the end of a wing, has made UAV "Geoscan-201" unstable in the air because of displacing center of mass.

To comply with the results of the experiment, a new UAV "Geoscan-301"has been designed (**Figure 3a**) and built (**Figure 3b**).

Aerodynamic modeling and measured magnetic effect (**Figure 4**) demonstrate compliance of the new UAV with all the requests of high-quality magnetic survey. Nevertheless, the new problem appeared during the flight tests: complicate control of the combustion engine makes flight control extremely difficult, and it requests fundamental changes in the software facilitating UAV operation.

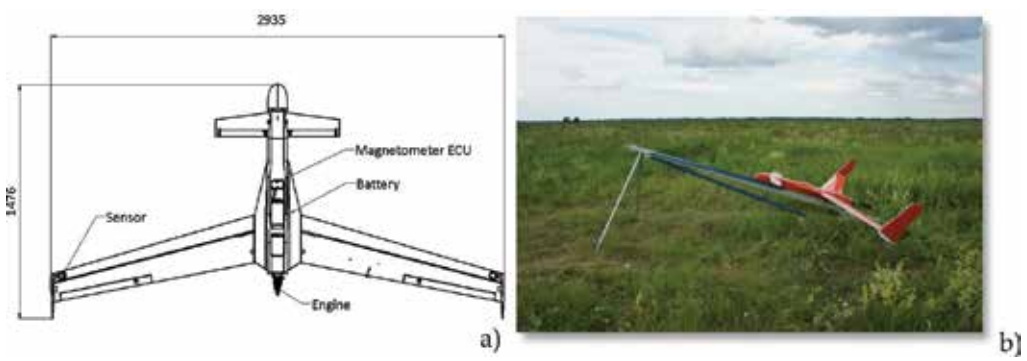

Figure 3. Design of "Geoscan-301" (a) and its launch (b).

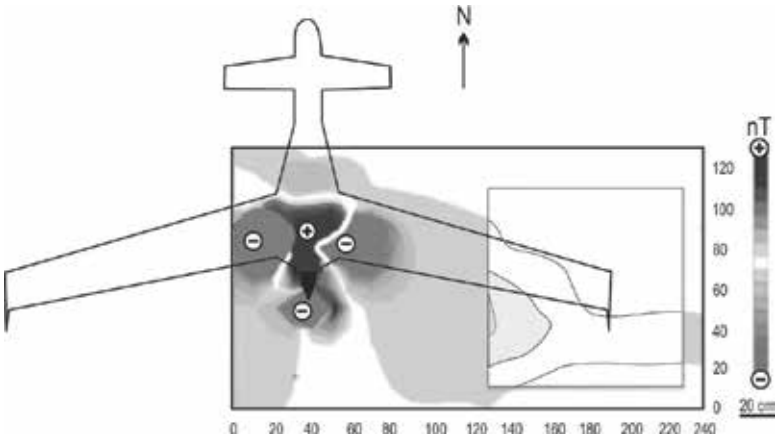

Figure 4. Measured magnetic effect of "Geoscan-301". Contour interval—25 nT; contour interval in the sidebar—1 nT.

2.2. Multirotor UAV

Multirotor UAV can be characterized as easiest-to-control type of unmanned aircrafts. At the same time, its magnetic noise is much more complicated in comparison with a fixed-wing UAV because of minimum four electric engines. And, there is no room for a magnetic sensor in the main UAV body, so we have to consider use of non-magnetic gondola attached to the UAV by rope (cable).

Magnetic noise of "Geoscan-401" quadcopter (**Figure 5**) measured at different distances from the UAV is given in **Table 1**.

It is obvious that at 3 m from the UAV, the magnetic noise is already negligible. Nevertheless, in UAMS built on the basis of "Geoscan-401", the length of the rope is 20 m, which is reasoned by aerodynamic specifics of this UAV. The lesser distance between gondola and UAV affects stability of the flight. It is necessary to note that for another UAVs, these figures can differ.

At the first tests, the gondola itself was a ring-shaped non-magnetic frame with rubidium vapor magnetometer (RVM) and additional differential GNSS receivers with external antennas [6]. Later, in order to improve UAMS aerodynamic characteristics, a crossbar-shape gondola had

Figure 5. Quadcopter "Geoscan-401".

Distance from the UAV, m	Max amplitude of magnetic noise, nT
1	≈5
2	≈1
3	≈0.1

Table 1. Measured magnetic noise of "Geoscan-401" quadcopter.

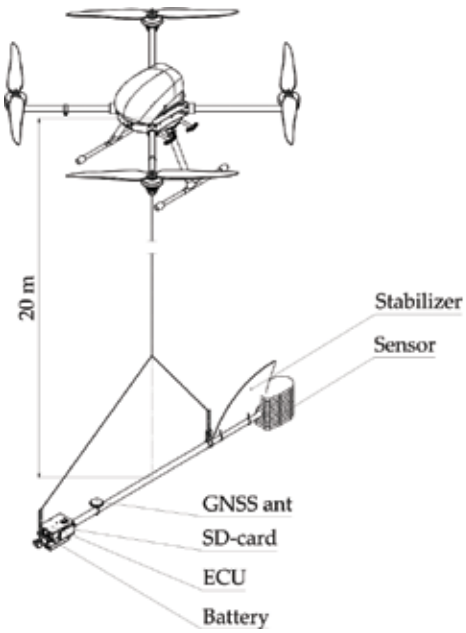

Figure 6. Unmanned aeromagnetic system (UAMS) on the basis of "Geoscan-401".

been designed (**Figure 6**). During the flight, the autopilot uses copter's GNSS for navigation, and GNSS on the outer frame registers the magnetometer's allocation using time synchronization method. The GNSS horizontal accuracy is about ±2.5 m, and vertical accuracy is about ±3 m.

Thus, both fixed-wing and multirotor UAVs can be used as a transport platform for UAMS. For the fixed-wing ones, optimal location of magnetic sensor(s) is at the ends of wings, and for the multirotor UAVs—at a gondola attached to UAV by a rope (cable) not less than 3 m in length, depending on magnetic and aerodynamic characteristics of the aircraft.

3. Magnetometer

Different models of magnetometers have been considered for UAMS. The magnetic sensor for unmanned aeromagnetic survey should be: (a) lightweight, not over 300 g; (b) quite fast, not

less than 10 measurements per second; and (c) insensitive to orientation. As far as no one from the magnetometers in the market responded to these requests without a sufficient adaptation, a new rubidium vapor magnetometer (RVM) has been designed and built for the purpose.

The specification of the rubidium vapor magnetometer (RVM; **Figure 7**) is listed in **Table 2**. The RVM includes: (i) magnetic sensor with a bulb containing vapor Rb^{87}; (ii) the Electronic Control Unit (ECU) including the optical pumping lamp; and (iii) the power source (not shown in **Figure 7**). All the parts are designed as separate modules connected by fiber-optic and electric cables, which facilitate distribution of the weight in the UAMS.

The RVM's noise has been checked at the magnetic field stabilizer, and it is about 10 pT/√Hz. The transition process (speed of reaction to a jump field) takes 30 ms.

To evaluate an absolute error of the RVM, a series of comparative tests has been conducted using the commercially available cesium vapor Geometrics G-858 and Overhauser MMPOS magnetometers. The field tests were organized in the area free of industrial noise and anomalous magnetic field gradients (Leningrad region, Russia).

Range of tests has been conducted in order to evaluate an influence of temperature on the measurements. The results demonstrate independence of measurements as well as of the measurement's error estimation of the temperature of both magnetic sensor and electronic unit of RVM [6].

Another standard test was conducted inside the calibration test station UPTM-4 in order to define the metrological characteristics of the magnetometer. The test had taken place at the

Figure 7. Rubidium vapor magnetometer (RVM).

Sensitivity	10 pT/√Hz
Field range	20,000–100,000 nT
Frequency response	200 Hz
Sampling rate	1000 Hz
The range sensor angles	±45°
Power	8–35 V, 10 W
Environment temperature	−20 … + 60°C
Weight of the sensor/ECU	120 g/300 g

Table 2. Specification of the rubidium vapor magnetometer (RVM).

B, nT	**Δ_{es}(B), nT**	**S(B), nT**
20,000	0.86	0.02
30,000	0.19	0.02
40,000	−0.19	0.02
50,000	−0.60	0.02
60,000	−1.28	0.01
70,000	−2.07	0.01
80,000	−3.05	0.03
90,000	−4.51	0.04
1000 000	−6.31	0.03

Table 3. RVM systematic errors Δ_{se}(B) and standard deviation S(B) depending on the magnetic induction (B).

facilities of FGUNPP "Geologorazvedka" in Leningrad region, Vsevolozhsk district. Results of the RVM systematic errors Δ_{se}(B) and standard deviation S(B) with a measurement range of magnetic induction module (B) are shown in **Table 3**.

All the experiments demonstrate conformity of all RVM characteristics with requests of high precision aeromagnetic survey.

4. Experiments and surveys

A number of magnetic surveys measuring total magnetic intensity (TMI) have been carried out using UAMS during the fall of 2016 and 2017 in different regions of Russia and Kazakhstan (**Table 4**). In all cases, the preprogrammed flights were executed along the parallel lines. Example of a flight layout is demonstrated in **Figure 8**.

Location	Size of area	Height of the survey (position of the sensor)	Distance between the flight lines	Type of the survey
Leningrad region, Agalatovo village	0.8 × 1 km	150 m from the highest point	50 m	Test survey
Republic Sakha-Yakutia	1 × 1 km	100 m from the highest point	100 m	Demonstration survey
Republic Kazakhstan, Eastern Kazakhstan, southwestern part of Kazakhstan Altay	7.5 × 4 km	50 m from the surface	50 m	Commercial survey
	1 × 1 km detalization	30 m from the surface	50 m	Commercial survey
		70 m from the surface	100 m	Commercial survey
Republic Kazakhstan, Central Kazakhstan	3.5 × 12 km	30 m from the surface	100 m	Commercial survey

Table 4. Magnetic surveys executed by Geoscan, Ltd. between September 2016 and November 2017 using UAMS on the basis of "Geoscan-401" quadcopter with RVM.

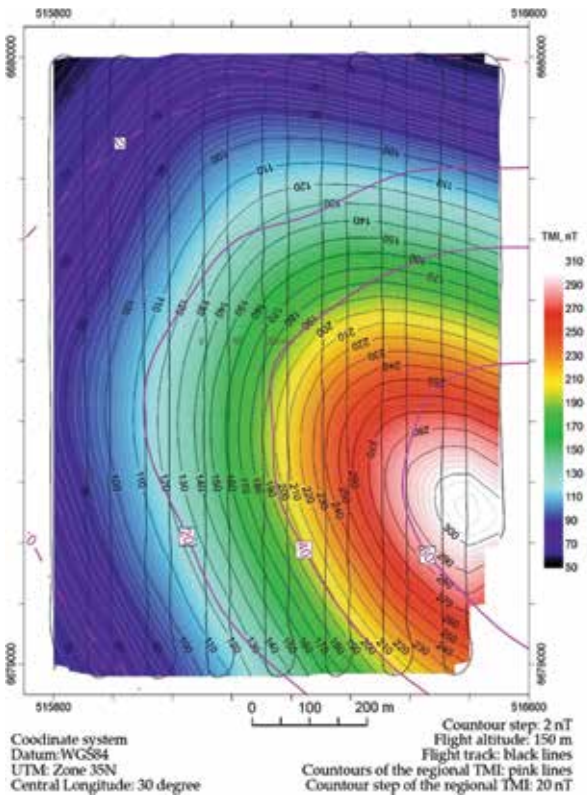

Figure 8. TMI map of the first test survey in Leningrad region.

The first survey has been carried out in Leningrad region just as a test of UAMS in the area with relatively quiet natural magnetic field with a local TMI anomaly of over 60 nT amplitude measured during regional aeromagnetic survey. The test survey has revealed an anomaly of concordant shape with higher (above 300 nT) intensity, which is due to lower height of the flight.

The results of the survey confirm workability of UAMS. Also, the comparison of task lines and real survey lines shows the difference of about 10 m for all flights of southward direction and approximately 1 m when the UAS moved northward (**Figure 8**). The latest demonstrates an influence of west wind (10 m/s) on a ring-shaped gondola. After this survey, the new gondola design (crossbar) has been implemented and used in all the subsequent surveys. The rope length has been cut from 50 to 20 m.

The second test was conducted in Republic Sakha-Yakutia in the area determined by potential UAMS buyer (**Figure 9**). The area is located at the flank of iron ore deposit and is characterized by more intensive TMI anomalies.

The survey has demonstrated stable measurements under conditions of high-gradient (up to 30 nT/m) magnetic field and, by conclusion of the buyer, good compliance with results of ground survey. Two UAMSs have been acquired, and, by now, about 100 km^2 of 1:10,000 magnetic survey has been carried out.

In 2017, 465 line km of 1:10,000 UAMS magnetic survey has been carried out in Central Kazakhstan [7]. The task of the survey is geological mapping, in particular—tracing of zones prospective for lead-zinc and iron-manganese ores of stratiform type in carbonyte rocks buried under sand and clay deposits. What is important, a comparison was made between UAMS and ground survey (**Figure 10**) as well as between UAMS and traditional aeromagnetic survey (**Figure 11**).

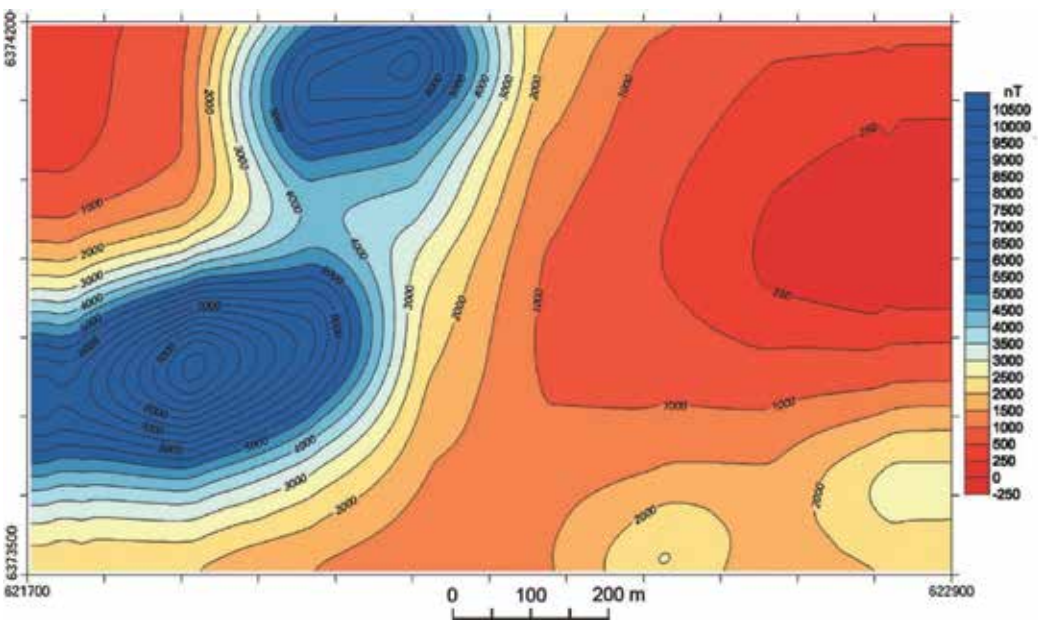

Figure 9. TMI map of the demonstration survey in Republic Sakha-Yakutia.

http://dx.doi.org/10.5772/intechopen.73003

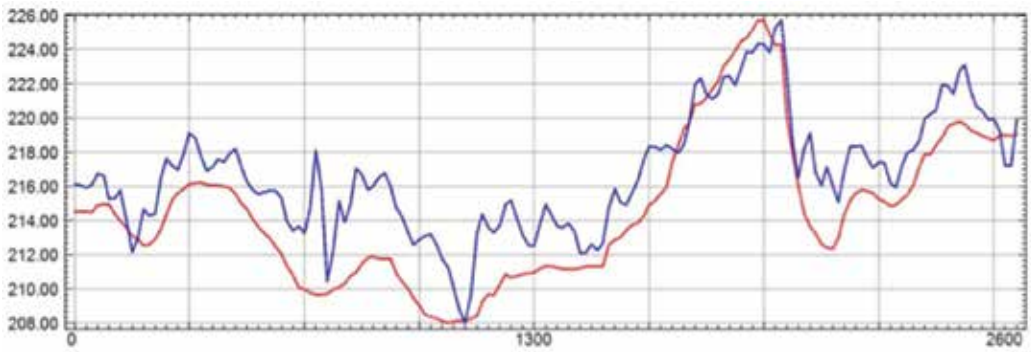

Figure 10. Comparison of ground (blue) and UAMS (red) measurements along the same line. X-axis—distance, m; Y-axis—TMI, nT.

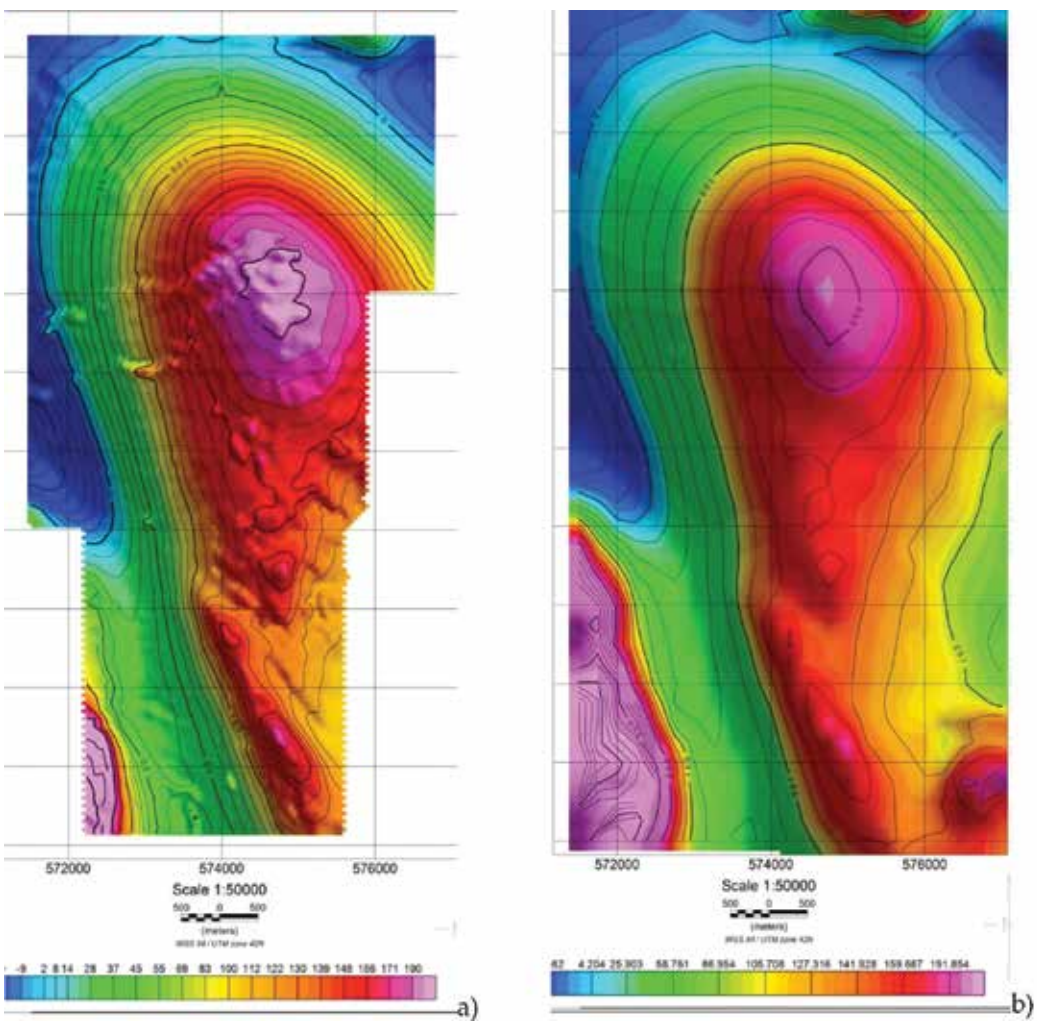

Figure 11. TMI map of the commercial survey in Central Kazakhstan: (a) UAMS 1:10,000 survey, 2017 and (b) 1:25,000 aeromagnetic survey, 1988.

The survey was carried out at as low as 30 m height (sensor position). Control measurements demonstrate TMI standard deviation at ±0.35 nT, which is a very good characteristic in comparison with both traditional aeromagnetic and ground surveys.

The more detailed (1:5000) UAMS survey was executed in the Eastern Kazakhstan over an area of 30 sq. km in the frames of gold ore deposits prospecting.

5. Conclusions

At the moment, the use of UAV in geology, including UAMS magnetic survey, experiences a fast grow. In 2016, special session named "Unmanned aerial vehicles (UAV)-based technologies for geology and Earth sciences" had been organized in the frames of 35th International Geological Congress. In 2018, similar session is supposed to take place at 15th Quadrennial Symposium of International Association for Genesis of Ore Deposits (IAGOD). These events indicate an interest of geological community to the new opportunities and, vice versa, growing readiness of the technologies for implementation.

In the frames of this study, few technical conclusions can be made, including the following:

- fixed-wing and multirotor UAVs can be used as a transport platform for UAMS;
- for UAMS based on the fixed-wing UAVs, optimal location of magnetic sensor(s) is at the ends of wings, and for the multirotor UAVs—at a gondola, it is attached to UAV by a rope or cable;
- design of UAMS includes deep adaptation of both UAV and magnetometer, targeting minimization of magnetic influence of UAV and its components on the magnetic measurements;
- UAMS based on "Geoscan-401" quadcopter is efficient for high-precision magnetic survey in the areas from first to $n \times 100$ km^2. One UAMS facilitates from 120 to 160 line km of magnetic survey per day;
- UAMS magnetic survey is more informative in comparison with traditional aerial survey at the count of lower flight and technical ability to circumvent the terrain;
- use of fixed-wing UAV can be more effective than of multirotor one, especially for large (over 100 km^2) areas, but fixed-wing UAMS still has issues to be resolved before entering the market.

One of the promising directions of the further development of UAMS magnetic survey is multilevel magnetic survey. Theoretical basis for such survey has been developed in the middle of twentieth century, but it would be extremely expensive to fly few times the same area by piloted aircraft. UAMS survey makes it effective when 3D magnetic field measurements are useful for geological purposes.

In comparison with traditional magnetic survey, advantages of UAMS are:

- the possibility of conducting a night flight;
- the simplified obtaining of resolving documentation for the flight;
- simultaneous survey by several UAMSs;
- independence from the location of the airports;
- reducing the cost of flight hours;
- the increase profitability of detailed survey compared to aeromagnetic and ground surveys.

Altogether, UAMS magnetic survey represents the future of magnetic prospecting, especially—in the ore geology, and provides geologists with new effective tool for field work.

Acknowledgements

Sufficient part of this research was funded by the Ministry of Education and Science of Russian Federation, under Agreement no. 14.607.21.0081 (ID no. RFMEFI60714X0081). The authors would like to thank FGUNPP "Geologorazvedka" and, personally, Vadim Tsirel for assistance in the testing of RVM. TOO "NPTs Geoken" and TOO "Kazzinc" have kindly allowed authors to demonstrate results of the first commercial survey executed with UAMS.

Author details

Sergey Cherkasov[1]* and Dmitry Kapshtan[2]

*Address all correspondence to: s.cherkasov@sgm.ru

1 Vernadsky State Geological Museum of Russian Academy of Sciences, Moscow, Russia

2 Geoscan, Ltd., Sankt-Petersburg, Russia

References

[1] Hanna WF. Some historical notes on early magnetic surveying in the U.S. Geological Survey. In: Hanna WF, editor. Geologic Applications of Modern Aeromagnetic Surveys. United States Geological Survey Bulletin 1924. 1990. pp. 63-73

[2] Gubbins D, Herrero-Bervera E, editors. Encyclopedia of Geomagnetism and Paleomagnetism. Berlin, Heidelberg: Springer-Verlag; 2007. 1054 pp

[3] Inozemtsev DP. Unmanned aircraft systems: Theory and practice Pt. 1. Overview of aircraft systems. ATIP. 2013;**2**(49):50-55 (in Russian)

[4] Korotkov VV, Glinskii NA, Kirsanov VN, et al. Aerial survey using unmanned aircraft systems—A new stage of development of domestic aerogeophysics. Ross.Geofiz. Zh. 2014;**53-54**:122-126

[5] Sterligov BV, Cherkasov SV. Reducing magnetic noise of an unmanned aerial vehicle for high-quality magnetic surveys. International Journal of Geophysics. 2016;**2016**:7. DOI: 10.1155/2016/4098275

[6] Sterligov BV, Cherkasov SV, Kapshtan DYa, Kurmaeva VV. An experimental aero-magnetic survey using a rubidium vapor magnetometer attached to the rotary-wings unmanned aerial vehicle. First Break. 2018 January;**36**(1):39-45. DOI: 10.3997/1365-2397.2017023

[7] Kovrizhnykh PN, Kozhamsugirov DO, Kozhevnikov SN, Makarov DV, Kapshtan DY. Innovative magnetic survey using unmanned aerial vehicle for ore deposits prospecting in Kazakhstan. Geologiya i okhrana nedr (Geology and Bowels of the Earth), Almaty. 2017;**4**(65):34-42 (in Russian)

Edited by George Dekoulis

Drone technologies have constantly been developing for over 100 years. The latest models exhibit a previously unseen set of specifications available to the end users. The collective effort of distinguished international researchers, within the field of drone technologies, has been incorporated into this textbook suitable to the broader audience. The book has been edited by Prof. George Dekoulis, Aerospace Engineering Institute (AEI), Cyprus, an expert on state-of-the-art implementations of reconfigurable space engineering systems. The book consists of four main sections, namely, ''Introduction,'' "Drone History," "Drone Design," and "Drone Applications." We hope this book will be beneficial to professionals, researchers, and academicians and, moreover, to inspire the younger generations into pursuing relevant academic studies and professional careers within the drone industry.

Published in London, UK

IntechOpen

ISBN 978-1-83881-478-6